Investigation of collectivity in the neutron-rich ^{142}Xe

Untersuchung der Kollektivität im neutronenreichen ^{142}Xe
Vom Fachbereich Physik der Technischen Universität Darmstadt zur Erlangung
des Grades eines Doktors der Naturwissenschaften (Dr. rer. nat.)
genehmigte Dissertation von M. Sc. Corinna Henrich aus Hanau
Tag der Einreichung: 06.10.2020, Tag der Prüfung: 23.11.2020

1. Gutachten: Prof. Dr. Thorsten Kröll
2. Gutachten: Prof. Dr. Wilfried Nörtershäuser

Darmstadt 2020 - D17

TECHNISCHE
UNIVERSITÄT
DARMSTADT

Fachbereich Physik
Institut für Kernphysik
AG Kröll

GEFÖRDERT VOM
Bundesministerium
für Bildung
und Forschung

ENSAR2

ISOLDE

Investigation of collectivity in the neutron-rich ^{142}Xe
Untersuchung der Kollektivität im neutronenreichen ^{142}Xe

Doctoral thesis by M. Sc. Corinna Henrich

1. Review: Prof. Dr. Thorsten Kröll
2. Review: Prof. Dr. Wilfried Nörtershäuser

Date of submission: 06.10.2020
Date of thesis defense: 23.11.2020

Darmstadt 2020 - D17

Bitte zitieren Sie dieses Dokument als:
URN: urn:nbn:de:tuda-tuprints-174736
URL: http://tuprints.ulb.tu-darmstadt.de/id/eprint/17473

Erklärung gemäß §9 Promotionsordnung

Hiermit versichere ich, dass ich die vorliegende Dissertation selbstständig angefertigt und keine anderen als die angegebenen Quellen und Hilfsmittel verwendet habe. Alle wörtlichen und paraphrasierten Zitate wurden angemessen kenntlich gemacht. Die Arbeit hat bisher noch nicht zu Prüfungszwecken gedient.

Darmstadt, 06.10.2020

M. Sc. Corinna Henrich

Abstract

The neutron-rich ^{142}Xe lies north-east of the doubly-magic ^{132}Sn, in a region that is not only describable by nuclear theory with single-particle and mean-field approaches, but also became accessible in experiments in recent times.

Since the astrophysical r process passes through the area, understanding the structure of nuclei therein may provide insight into the A = 130 peak in the solar-element abundances.

Furthermore, ^{144}Ba, a nucleus that exhibits strong octupole collectivity, lies in the immediate proximity just two protons above ^{142}Xe.

In order to gain understanding on the evolution of quadrupole and octupole collectivity in this region, a Coulomb excitation experiment was carried out using the MINIBALL and C-REX setup at the HIE-ISOLDE facility, CERN.

Several reduced transition strengths of low-lying transitions along with the spectroscopic quadrupole moments of the respective states could be determined. Additionally, new low-spin low-energy states, interpreted as part of a γ band, demonstrated for the first time in this isotope, could be identified, and the location of the 3_1^- state supported.

The results are compared to SCCM and LSSM calculations.

Zusammenfassung

Das neutronenreiche ^{142}Xe liegt nordöstlich des doppeltmagischen ^{132}Sn, in einer Region, die nicht nur durch Einteilchen- und Meanfieldansätze beschreibbar ist, sondern zudem kürzlich experimentell zugänglich wurde.

Da der astrophysikalische r-Prozess innerhalb dieser Gegend erwartet wird, könnte das Wissen um die Kernstruktur dieser Nuklide zum besseren Verständnis der $A = 130$ Erhöhung in den Elementhäufigkeiten beitragen.

Desweiteren befindet sich ^{144}Ba, ein Kern, welcher eine starke Oktupolkollektivität aufweist, mit zwei zusätzlichen Protonen in der unmittelbaren Nähe von ^{142}Xe.

Um die Datenlage in Bezug auf Quadrupol- und Oktupolkollektivität zu verbessern, wurde ein Coulombanregungsexperiment unter Verwendung von MINIBALL und C-REX an HIE-ISOLDE, CERN, durchgeführt.

Sowohl mehrere reduzierte Übergangswahrscheinlichkeiten von niedrig liegenden Übergängen, als auch spektroskopische Quadrupolmomente konnten bestimmt werden. Zusätzlich wurde zum ersten Mal Evidenz für die Existenz eines Gammabandes innerhalb dieses Kerns in Form von niedrig liegenden Zuständen gefunden. Weiterhin konnte die Lage des 3_1^- Zustandes unterstützt werden.

Die Ergebnisse werden mit SCCM und LSSM Rechnungen verglichen.

Contents

1. Introduction - physics case

To date, more than 3300 nuclides have been observed in various experimental campaigns [1] though about 7000 nuclei are predicted to exist in between the driplines [2].

The synthesis of the lighter elements up to iron is possible by thermonuclear fusion, while heavier nuclei mainly form via multiple captures of neutrons. In nuclear astrophysics the observed solar abundances above iron are explained as a result of two processes. On the one hand the slow s-process, that takes place at low neutron capture rates as compared to the beta-decay time of the respective nucleus. On the other hand the rapid r-process, which involves nuclei far away from β stability and high capture rates.

Understanding the mechanisms and the environment that rule the r-process is an active field in nuclear astrophysics. For example, there is evidence that merger of two neutron stars contribute to the production of nuclides via the r-process. These events are used to explain the observed solar abundances for nuclei within and above the $A \approx 130$ peak [3, 4].

As the r-process is expected to pass through the region north-east of the doubly-magic ^{132}Sn, knowledge on the nuclear structure of the nuclides therein may impact the theoretical description of the r-process as well.

The region possesses some interesting features, such as the irregularily low energy of the 2_1^+ state in ^{128}Cd and ^{136}Te. In Figure 1.1, the evolution of the energies of the first 2^+ states and reduced transition strengths around the $N = 82$ neutron-shell closure are shown.

Another prominent property in that region are enhanced octupole correlations, reported already for the doubly-magic ^{132}Sn [5] and peaking at ^{144}Ba [6]. Large octupole correlations are expected to occur specifically for nuclei with 56 protons and 88 neutrons [7, 8].

The neutron-rich nucleus ^{142}Xe lies two protons below ^{144}Ba, also possessing 88 neutrons. While estimated dipole moments in the other xenon isotopes appear to indicate a significant drop of octupole correlations as compared to barium, the same may not be true for ^{142}Xe [9]. This makes this isotope a perfect candidate for further investigation of the evolution of octupole collectivity in this region.

An excellent means to explore the low-lying states of this nucleus is Coulomb excitation. The method gives direct access to reduced transition strengths and spectroscopic quadrupole moments. Therefore, especially as both these quantities can be measured, Coulomb excitation is a very powerful tool to probe the collectivity of nuclear excitations and particularly nuclear shapes.

The low-lying structure of ^{142}Xe and its even-even neighboring isotopes have already been investigated within the scope of a Coulomb-excitation campaign at REX-ISOLDE [10]. With

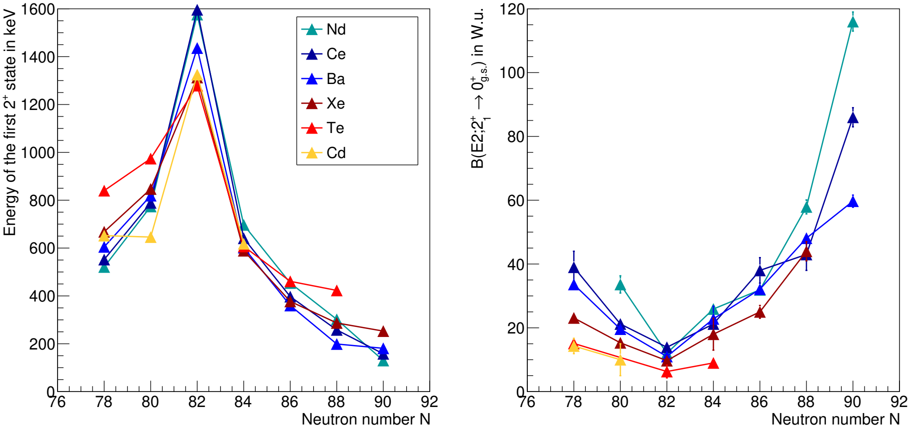

Figure 1.1.: Evolution of E(2_1^+) and B(E2; $2_1^+ \rightarrow 0^+_{\text{g.s.}}$) values in the region of ^{142}Xe. Note that the neutron shell closure is at N = 82. Literature values as found in NNDC.

the lower available beam energy of 2.7 MeV/u only the first 2^+ and first 4^+ states could be populated. The weakness of the excitation of the 4^+ state led to large uncertainties on the determined observables.

The facility's recent upgrade to HIE-ISOLDE [11] provided a higher beam energy of 4.5 MeV/u and thus a higher probability for multiple-step Coulomb excitation. Such an energy is needed for populating the 4_1^+ state with sufficient statistics within the given time frame as well as exciting higher-lying states.

Additionally, this beam energy makes single-step excitation of the 3_1^- state possible, which is necessary to gain understanding of the octupole collectivity of the nucleus.

2. Nuclear structure physics

Several years after the atomic nucleus was discovered in 1911 [12], it became apparent that nuclei consist not only of protons but also of neutrons [13] and thus exhibit an internal structure [14, 15]. Over time, the nuclear shell model formulated by Goeppert-Mayer [16] and Haxel, Jensen and Suess [17] was joined by complementary collective models proposed, e.g., by Bohr and Mottelson [18]. To this day both these model types, as well as other approaches, are being improved to reproduce and predict experimental data.

The nuclear shell model is structured in a similar manner as the atomic shell model describing the electrons in an atom. The nucleons are expected on certain discrete energy levels and to obey the Pauli exclusion principle.

The model is able to reproduce the experimentally found magic numbers, i.e., the numbers of nucleons needed to fill shells when starting from the bottom. Experimental evidence for these numbers is provided by, for example, sudden changes in the two-neutron separation energy when approaching closed shells [19] and differences in the mean-square charge radii of the nuclei [20]. The basics of the shell model are described in Section 2.1.

Going away from closed shells nuclei undergo drastic changes. While doubly-magic nuclei can be considered spherical in their ground state, mid-shell nuclei are anything but that. A number of observables reflect this onset of deformation. The energies of the first 2^+ states in even-even nuclei drop when moving away from shell closures, while, at the same time, the transition strengths connecting the ground to the first excited state increase.

These changes cannot be explained using the spherical shell model and are better described in terms of collective behavior. Expressing the aforementioned transition strengths in single-particle or Weisskopf units (see Section 3.4), provides evidence that in many nuclei multiple nucleons are participating in transitions. The collective model by Bohr and Mottelson describes the nucleus as a droplet of nuclear matter like the liquid-drop model by Bohr and Kalckar [21, 22]. As such the nucleus is allowed to vibrate and rotate if it has a non-spherical shape.

An overview on the collective model by Bohr and Mottelson is given in Section 2.2.

2.1. Shell model

The idea of the shell model is a nucleus in which a system of independent nucleons reside in a central potential. An additional residual interaction V_{res} accounts for the interaction between two particles i and j. Higher interaction orders are neglected. This section follows mostly [20, 23].

A Hamiltonian describing such an interaction can be defined as

$$\mathcal{H} = \mathcal{H}_0 + V_{\text{res}} = \mathcal{H}_0 + \sum_{i<j}^{A} V_{ij} - \sum_{i=1}^{A} U(r_i)\,, \tag{2.1}$$

thus describing a common spherical potential as opposed to a nucleon-nucleon interaction potential. The independent-particle Hamiltonian is defined as

$$\mathcal{H}_0 = \sum_{i=1}^{A} h_i = \sum_{i=1}^{A} \left(\frac{\vec{p_i}^{\,2}}{2M} + U(r_i) \right) . \tag{2.2}$$

The single-particle potential $U(r_i)$ is understood as being distinct for neutrons and protons, as due to the Coulomb force an additonal repulsive potential should be added for protons.

To account for the short-range character of the strong force a potential of the form of an infinite square well, which reads

$$U(r) = \begin{cases} -V_0 & \text{if } r < R \\ \infty & \text{if } r \geq R \end{cases} \tag{2.3}$$

or the spherical harmonic oscillator

$$U(r) = \text{const.} + \frac{1}{2} M \omega^2 r^2 \,, \tag{2.4}$$

can be used. The nuclear frequency is denoted as ω.

Both these potentials are analytically solvable, and the most commonly used potential is the spherical harmonic oscillator. A more realistic single-particle potential, which is proportional to the nuclear-density distribution, is the Woods-Saxon potential [24]

$$U(r) = -V_0 \left(1 + \exp\left\{ \frac{r-R}{a} \right\} \right)^{-1} , \tag{2.5}$$

where a describes the diffuseness of the nuclear surface, and R is a measure of the nuclear size.

All three potentials are sketched in Figure 2.1.

For a single particle in a spherical symmetric potential the spatial wave function reads

$$\psi_{nlm} = R_{nl}(r) \mathcal{Y}_{lm}(\vartheta, \varphi) \,, \tag{2.6}$$

where $R_{nl}(r)$ is the radial component and $\mathcal{Y}_{lm}(\vartheta, \varphi)$ are the spherical harmonics. The radial quantum number n takes the values $n = 1, 2, 3, \ldots$, the orbital angular momentum

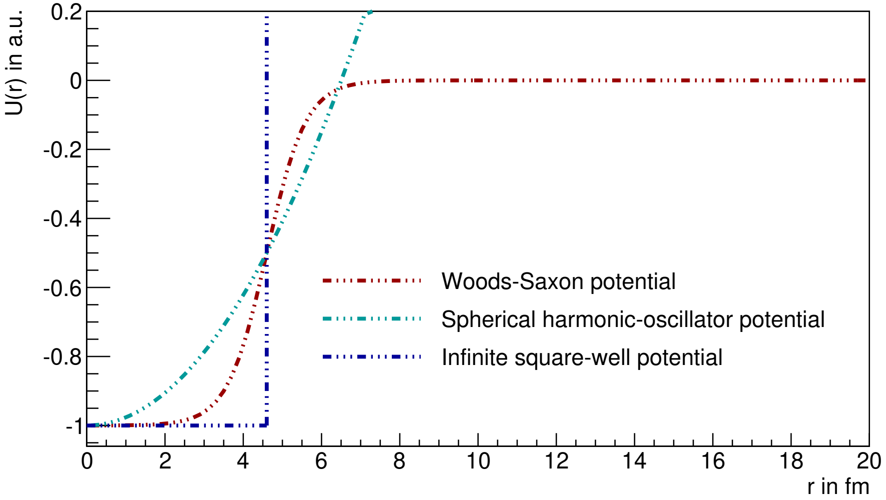

Figure 2.1.: Single-particle shell-model potentials. The infinite-well potential is sketched in blue, the spherical harmonic-oscillator potential in cyan, and the Woods-Saxon potential in red.

l the values $l = 0, 1, ..$ (s, p, d, f, g, ..) and the magnetic quantum number m the values $m = -l, .., +l$.

The energy levels for a spherical three-dimensional harmonic oscillator are

$$E_{nl} = (N + \frac{3}{2})\hbar\omega\,, \tag{2.7}$$

with the principal quantum number $N = 2(n-1) + l$. The nuclear frequency can be estimated as $\hbar\omega = 41A^{-1/3}\,\mathrm{MeV}$.

Trying to reproduce the full set of magic numbers using this approach fails except for the first few. Because of this, historically, a strong spin-orbit interaction was proposed by Goeppert-Mayer [16] and Haxel, Jensen and Suess [17], while as further correction a term proportional to the squared angular momentum was suggested by Nilsson [25].

The latter was introduced to account for the flatter potential caused by the centrifugal force as the angular momentum increases and results in lower level energies for high-l states. Together with the term proportional to the product of spin and angular momentum, the single-particle Hamiltonian then becomes

$$h_i = \frac{\vec{p_i}^{\,2}}{2M} + \frac{1}{2}M\omega^2 r^2 - D\vec{l}^{\,2} - \xi\vec{l}\cdot\vec{s}\,. \tag{2.8}$$

The parameter ξ is negative for the coupling $j = l - 1/2$ and positive for $j = l + 1/2$.

With these adjustments the magic numbers (2, 8, 20, 28, 50, 82) could be reproduced. A picture showing the produced energy-level sequence can be found in various sources, e.g., [20, 23, 26]. Furthermore, the spherical shell model can be used to predict ground-state spins and parities.

Problems arise when going away from closed shells to nuclei exhibiting a deformation. To account for these, the Nilsson model [25] was formulated. Here, the spherical potential is replaced by one with spheroidal shape, i.e., allowing either a prolate or oblate deformation of the nucleus.

The axially-symmetric single-particle Hamiltonian reads

$$h_i = \frac{\vec{p_i}^{\,2}}{2M} + \frac{1}{2}M\left(\omega_\perp^2(x^2+y^2) + \omega_z^2 z^2\right) - D\vec{l}^{\,2} - \xi\vec{l}\cdot\vec{s}\,, \tag{2.9}$$

where the x, y, and z coordinates are to be understood as relative to the intrinsic axes of the rotor. The frequencies are given by

$$\omega_\perp = \omega_0(\epsilon)(1 + \frac{1}{3}\epsilon) \tag{2.10}$$

$$\omega_z = \omega_0(\epsilon)(1 - \frac{2}{3}\epsilon)\,, \tag{2.11}$$

where ϵ denotes the deformation parameter. This parameter can also be found in the collective model by Bohr and Mottelson as it is connected to their deformation parameter β by

$$\epsilon \approx \frac{3}{2}\sqrt{\frac{5}{4\pi}}\beta + \frac{3}{8}\frac{5}{4\pi}\beta^2 + O(\beta^3)\,. \tag{2.12}$$

For the Nilsson diagram depicting the energy-level sequence dependent on the deformation parameter ϵ the reader is again referred to [20, 23].

Many ground-state spins in deformed nuclei can be explained utilizing the Nilsson model, though a certain ambiguity in its prediction capabilities remains. Excited states in deformed nuclei cannot be explained well as collective effects take place.

2.2. Bohr collective model

The collective model by Bohr and Mottelson [18] describes the nucleus as nuclear-matter droplet in which the nucleons act in a highly correlated manner. The nucleus may exhibit a shape and is allowed to vibrate and rotate depending on its deformation. This part follows [20, 23].

The surface of a nucleus can be denoted as

$$R(\vartheta,\varphi) = R_0\left(1 + \sum_{\lambda,\mu} a_{\lambda\mu}\mathcal{Y}_{\lambda\mu}(\vartheta,\varphi)\right)\,, \tag{2.13}$$

with the spherical harmonics $\mathcal{Y}_{\lambda\mu}(\vartheta,\varphi)$, a set of parameters $a_{\lambda\mu}$ reflecting the deformation, the multipole order λ, and the magnetic quantum number μ.

A vibrational mode with a particular non-zero λ is called a 2^λ-pole mode. A monopole or breathing mode is not expected at low excitation energies as nuclear matter is considered incompressible, and a dipole mode would describe a translation motion. Therefore, the first mode of interest is the $\lambda = 2$ mode, the quadrupole. Furthermore, octupole, hexadecapole, and 2^5-pole vibrations are observed in some nuclei.

The vibrational model assumes that oscillator quanta, *phonons* (spin two and spin μ along the laboratory fixed z-axis), are created and annihilated using the respective operators.

In this model the ground state has a total angular momentum of $I = 0$ if no intrinsic spin is present. For the first excited state the angular momentum is equal to two. Going to higher states the assignment becomes more difficult as a range of magnetic substates is available. For the second excited state two photons need to be considered, which leads to $I = 0, 2, 4$.

The Hamiltonian for quantized harmonic quadrupole vibrations reads

$$\mathcal{H}_{HV} = \sum_{\mu} \hbar\omega \left(O^{+}_{2\mu} O^{2\mu} + \frac{1}{2} \right) , \ \mu = 0, \pm 1, \pm 2 , \tag{2.14}$$

with the creation $O^{+}_{2\mu}$ and annihilation operator $O^{2\mu}$, and the nuclear frequency of the vibrations ω.

The corresponding energy eigenvalues are given by

$$E_n = (n + \frac{5}{2})\hbar\omega , \ n = 0, 1, 2, \ldots \tag{2.15}$$

The zero-point vibrational energy is therefore given as $\frac{5}{2}\hbar\omega$.

To identify a typical vibrator the ratio

$$R_{42} = \frac{E(4^{+}_{1})}{E(2^{+}_{1})} , \tag{2.16}$$

relating the level energy of the first 4^{+} to that of the first 2^{+} state can be used. That ratio should be equal to 2 for a vibrator.

For quadrupole deformation of symmetric nuclei the parameters $a_{\lambda\mu}$ given in Equation 2.13 can be expressed by the introduction of a radial coordinate β and an angle coordinate γ, in the following way:

$$a_{20} = \beta \cos(\gamma) , \tag{2.17}$$

and

$$a_{2+2} = a_{2-2} = \frac{1}{\sqrt{2}} \beta \cos(\gamma) . \tag{2.18}$$

The β parameter denotes the magnitude of deformation of the nucleus, while the triaxiality parameter γ describes the rotational symmetry. Two conventions exist, but the one used in this work is the following: β is only allowed to take positive values, i.e., the nucleus is spherical for $\beta = 0$. γ is allowed to range between 0, indicating an axially symmetric prolate shape, and 60 °, reflecting an axially symmetric oblate shape. For $0 < \gamma < 60$ °, the nucleus assumes an ellipsoidal shape, having three unequal axes.

Quantum mechanically only a deformed nucleus is expected to rotate. This implies that only open-shell nuclei exhibit rotational modes. The Hamiltonian for a quantum-mechanical rotor reads

$$\mathcal{H}_{rot} = \frac{\hbar^2}{2\mathcal{I}} I^2 . \tag{2.19}$$

Generally the rotor Hamiltonian is not analytically solvable, but the axially symmetric case, defined as

$$\mathcal{I}_1 = \mathcal{I}_2 = \mathcal{I} \neq \mathcal{I}_3 = 0\,, \tag{2.20}$$

is.

The corresponding Hamiltonian becomes

$$\mathcal{H}_{rot} = \frac{\hbar^2}{2\mathcal{I}}(I^2 - I_3^2)\,, \tag{2.21}$$

with the energy eigenvalues

$$E_{KI} = \frac{\hbar^2}{2\mathcal{I}}(I(I+1) - K^2)\,. \tag{2.22}$$

For a typical rotor the R_{42} ratio defined in Equation 2.16 should be $R_{42} = 3.33$.

Up to this point the nucleus was described as either rotating or vibrating. Of course, a nucleus can do both. Considering an axially symmetric rotor, the Hamiltonian can be approximately separated in three uncoupled terms and reads

$$\mathcal{H} \approx \mathcal{H}_{\text{rotor}} + \mathcal{H}_\beta + \mathcal{H}_\gamma\,. \tag{2.23}$$

The corresponding energy levels are given by

$$E_{n_\beta n_\gamma KL} = \frac{\hbar^2}{2\mathcal{I}}(I(I+1) - K^2) + (n_\beta + \frac{1}{2})\hbar\omega_\beta + (n_\gamma + 1)\hbar\omega_\gamma\,. \tag{2.24}$$

Hence, alongside the rotational main band, a sequence of β and γ vibrational bands is expected to be generated, as well as their combinations. Here, β vibration is understood as the nucleus compressing and stretching while it maintains its axial symmetry. For γ vibration, the nucleus vibrates towards a triaxial shape.

3. Coulomb excitation

Coulomb excitation (abbr.: Coulex) is the excitation of a nucleus via the long-range electromagnetic interaction with the changing field of a passing charged particle. For the limit of so-called “Safe” Coulex (Section 3.3), only the well-known electric Coulomb force causes the excitation, while more complicated nuclear interactions and magnetic excitations are negligible. Details on Coulex at intermediate and relativistic energies can be found in [27] and [28], respectively.

Coulex as a method provides access to the cross sections of the participating states. These cross sections are probed via the indirect measurement of the level population, which, in turn, can be determined by measuring the internal conversion electrons [29], the kinetic energies of the collision partners [30], or the emitted γ-rays (Section 3.6), as is done here.

Coulex is a perfect tool to probe the collective properties of nuclei. Vibrational and rotational low-lying states in particular are readily excited using this method. The reduced transition strengths (Section 3.4) provide a way to estimate the collectivity of a transition, while the spectroscopic quadrupole moments (Section 3.5) reflect the shape of the nucleus.

In the following, the electromagnetic transitions caused by Coulomb excitation are described quantum mechanically (Section 3.2 and 3.5), while the particle trajectories are treated classically (Section 3.1). The latter means that the nuclei follow classical Kepler trajectories during the entire process.

The numerical methods used for this analysis are discussed in Section 3.7.

This chapter aims to provide an overview on the method and is based mostly on Reference [31, 32]. For other detailed discussions see for example [33, 34].

3.1. Classical particle trajectories

For the characterization of the movement of a nucleus (charge Z_1, mass number A_1, velocity v, energy E_1 in MeV) in the Coulomb field of their reaction partner with charge number Z_2, it is practical to use the Sommerfeld parameter

$$\eta = \frac{Z_1 Z_2 e^2}{\hbar v} \approx \frac{Z_1 Z_2 A_1^{1/2}}{6.32\,\mathrm{E}_1^{1/2}}\,. \tag{3.1}$$

This dimensionless quantity is a measure for the effective strength of the interaction. I.e., $\eta \ll 1$ reflects a small distortion of the incident wave by the Coulomb field, so that the Born approximation can be used for the description [31]. For the case of $\eta \gg 1$, the particle can be considered as a wave packet moving along a classical trajectory. The latter is true here, as in our case $\eta = 330$.

Therefore, the Rutherford cross section can be used to describe the elastic scattering process, which reads

$$\left(\frac{d\sigma}{d\Omega}\right)_{\text{Ruth.}} = \frac{1}{16}\frac{d_{\text{min}}^2}{\sin^4(\vartheta_{\text{CM}}/2)} , \tag{3.2}$$

where d_{min} stands for the distance of closest approach, given by

$$d_{\text{min}} = 2\frac{Z_1 Z_2 e^2}{m_0 v^2} . \tag{3.3}$$

Allowing inelastic scattering as well, the related dimensionless quantity ξ is defined by

$$\xi = \frac{Z_1 Z_2 e^2}{\hbar v_\infty} \cdot \frac{\Delta E}{2E} , \tag{3.4}$$

with $E = \frac{1}{2} m_0 v_\infty^2$. Hence, this quantity describes how much energy can be transferred. Together with the eccentricity

$$\epsilon = \frac{1}{\sin(\vartheta/2)} , \tag{3.5}$$

which is dependent on the deflection angle ϑ, the ratio between collision time τ and nuclear period T can be described as the product $\xi\epsilon$, which reflects the adiabaticity of the reaction. I.e., for $\xi\epsilon \gg 1$, an adiabatic cut-off takes place, such that the internal motion of the nucleus can adapt to any change [31]. The nuclear period T is reversely proportional to the nuclear frequency ω:

$$\frac{1}{T} \propto \omega = \frac{\Delta E}{\hbar} = \frac{E_f - E_i}{\hbar} , \tag{3.6}$$

with the excitation energy ΔE, i.e., the energetic difference between the two energy levels.

Note, that $\xi(\vartheta = 180\,^\circ)$ is often defined as adiabaticity parameter [34].

Generally, the cross section for the excitation of a certain state via Coulex is given by

$$\left(\frac{d\sigma}{d\Omega}\right)_{\text{CLX}} = P_{if}\left(\frac{d\sigma}{d\Omega}\right)_{\text{Ruth.}} , \tag{3.7}$$

that is in addition to the Rutherford cross section, as defined in Equation 3.2, the probability P_{if} to find the nucleus in a given state has to be taken into consideration.

The probability P_{if} is linked to the amplitudes b_{if} for the transition from one state i with spin I_i to another state f by

$$P_{if} = \frac{1}{2I_i + 1} \sum_{M_i M_f} |b_{if}|^2 \, . \tag{3.8}$$

Here, M_i and M_f denote the magnetic quantum number of the initial and final state, respectively. The value $|b_{if}|^2$ is also known as Fermi's Golden Rule.

3.2. Coulex as first-order perturbation theory

In order to calculate the excitation probabilty the time-dependent Schrödinger equation is used, which reads

$$i\hbar \frac{d\psi(t)}{dt} = (\mathcal{H}_0 + \mathcal{H}(t))\psi(t)\,, \tag{3.9}$$

with the wave function $\psi(t)$, the Hamiltonian of the undisturbed system $\mathcal{H}_0$ and the time-dependent electromagnetic interaction $\mathcal{H}(t)$. The latter Hamiltonian can be split up into three parts: The monopole-monopole term describing the classical Rutherford interaction, the monopole-multipole term characterizing the excitation of only one nucleus and a multipole-multipole term representing the simultaneous excitation of both nuclei. As the excitation probabilities are very small, the last part can be considered negligible.

In first order, only direct excitations of states are allowed, i.e., excitation paths via intermediate states, described as products of transition amplitudes, are excluded. Second-order effects are discussed at a later point in Section 3.5.

Following this approach, the transition amplitudes b_{if} are denoted as the integral over the time-dependent Hamiltonian $\mathcal{H}(t)$ and an exponential comprising the nuclear frequency ω:

$$b_{if} = \frac{1}{i\hbar} \int_{-\infty}^{\infty} \langle f | \, \mathcal{H}(t) \, | i \rangle \, e^{i\omega t} dt \, . \tag{3.10}$$

For most cases, the transition amplitudes are very small, i.e., $b_{if} \ll 1$.

The electric interaction is described classically as

$$\mathcal{H}_e(t) = \int \rho_n(\vec{r}) \varphi(\vec{r}, t) d\tau \, , \tag{3.11}$$

with the nuclear charge-density operator $\rho_n(\vec{r})$ and $\varphi(\vec{r}, t)$ defined as

$$\varphi(\vec{r}, t) = \frac{Z_1 e}{|\vec{r} - \vec{r}_p(t)|} - \frac{Z_1 e}{\vec{r}_p(t)} \, . \tag{3.12}$$

To be able to calculate the matrix element in Equation 3.10, the matrix element is expanded using the description of the monopole-multipole interaction via multipole moments. The result of this reads

$$\mathcal{H}_e(t) = 4\pi Z_1 e \sum_{\lambda=1}^{\infty} \sum_{\mu=-\lambda}^{\lambda} r_p(t)^{-\lambda-1} \mathcal{Y}_{\lambda\mu}(\vartheta(t), \varphi(t)) \rho_n(\vec{r}(t)) d\tau \,, \tag{3.13}$$

where the electric multipole moments

$$\mathcal{M}(E\lambda, \mu) = \int \vec{r} \mathcal{Y}_{\lambda\mu}(\vartheta, \varphi) \rho_n(\vec{r}) d\tau \tag{3.14}$$

are related to the normalized spherical harmonics $\mathcal{Y}_{\lambda\mu}(\vartheta, \varphi)$.

Using this, the transition amplitude becomes

$$b_{if} = \frac{4\pi Z_1 e}{i\hbar} \sum_{\lambda,\mu} \frac{1}{2\lambda+1} \left\langle I_i M_i \right| \mathcal{M}(E\lambda, \mu) \left| I_f M_f \right\rangle S(E\lambda, \mu) \,, \tag{3.15}$$

for electric excitations. The quantity $S(E\lambda, \mu)$ is defined as

$$S(E\lambda, \mu) = \int_{-\infty}^{\infty} e^{i\omega t} \mathcal{Y}_{\lambda\mu}(\vartheta(t), \varphi(t)) \left[\vec{r}_p(t)\right]^{-\lambda-1} dt \,. \tag{3.16}$$

Putting this information into Equation 3.7, the differential Coulomb-excitation cross section for electric processes reads

$$\left(\frac{d\sigma}{d\Omega}\right)_{CLX,E\lambda} = \frac{\pi Z_1^2 e^2}{\hbar^2} \frac{d_{\text{min}}^2}{\sin^4(\vartheta/2)} \frac{B(E\lambda)}{(2\lambda+1)^3} \sum_{\mu} \left|S(E\lambda, \mu)\right|^2 \,. \tag{3.17}$$

Here, the nuclear-structure information is fully given by the reduced transition strength $B(E\lambda)$.

This can be further rewritten by introducing a dimensionless function $f_{E\lambda}(\vartheta, \xi)$ containing all information on the classical trajectory of the scattered particle. Thus the electric component of the differential cross section for Coulomb excitation reads

$$\left(\frac{d\sigma}{d\Omega}\right)_{CLX,E\lambda} = \left(\frac{Z_1 e}{\hbar v}\right)^2 \left(\frac{d_{\text{min}}}{2}\right)^{-2\lambda+2} B(E\lambda) f_{E\lambda}(\vartheta, \xi) \,. \tag{3.18}$$

In a similar fashion the magnetic component can be defined[1] as

$$\left(\frac{d\sigma}{d\Omega}\right)_{CLX,M\lambda} = \left(\frac{Z_1 e}{\hbar c}\right)^2 \left(\frac{d_{\text{min}}}{2}\right)^{-2\lambda+2} B(M\lambda) f_{M\lambda}(\vartheta, \xi) \,. \tag{3.21}$$

---

[1] For magnetic excitation the starting point is in analogy to the electric case of Equation 3.11:

$$\mathcal{H}_m(t) = -\frac{1}{c} \int \vec{j}_n(\vec{r}) \cdot \vec{A}(\vec{r}, t) d\tau \tag{3.19}$$

3.3. Safe Coulex

The Coulomb excitation process is considered “safe” if only the electromagnetic interaction governs the process. That is, no nuclear interference effects take place and change the excitation probabilities. This condition can be met by either restricting the beam energy or the scattering parameters, i.e., the scattering angles under which the nuclei are detected. Due to the diffuseness of the nuclear matter distribution it can be rather difficult to define an exact value, and multiple parameterizations exist.

Equation 3.3 for the distance of closest approach in the scattering process can be rewritten as

$$d_{\text{min}} = \frac{e}{4\pi\epsilon_0} \frac{Z_1 Z_2}{E_{\text{CM}}} \,, \tag{3.22}$$

with the energy in the center-of-mass frame E_{CM}. The relation to the laboratory beam energy E_{lab} reads

$$E_{\text{CM}} = \frac{A_2}{A_1 + A_2} \cdot E_{\text{lab}} \,, \tag{3.23}$$

where the particle denoted with index 1 is understood as the projectile and index 2 indicates the target.

Therefore the beam energy in MeV can be calculated as

$$E_{\text{lab}} = 0.72 \cdot \frac{Z_1 Z_2}{d} \cdot \frac{A_1 + A_2}{A_2} \left(1 + \frac{1}{\sin\left(\frac{\vartheta_{\text{CM}}}{2}\right)} \right) \,, \tag{3.24}$$

where the distance d stands for the distance between the centers of the two scattering nuclei.

For the limit of “Safe” Coulex this distance has to exceed a certain safe distance d_{min}, so that

$$d > d_{\text{min}} \tag{3.25}$$

holds true, to ensure an exclusive electromagnetic interaction. Generally, this distance is understood as sum of the two radii R_i in addition to a safety separation s, i.e.,

$$d_{\text{min}} = R_1 + R_2 + s \,. \tag{3.26}$$

---

with the nuclear current density $\vec{j}_n(\vec{r})$ and the vector potential

$$\vec{A}(\vec{r}, t) = \frac{Z_1 e}{c} \frac{\vec{v}_p(t)}{|\vec{r} - \vec{r}_p(t)|} \,. \tag{3.20}$$

The relative velocity of the reaction partners is denoted as $\vec{v}_p(t)$. The full derivation can be found in [31].

This additional safety separation accounts for the diffuseness of the matter distribution of nuclei. Various values are given in literature, ranging between 3 fm [35] and 6 fm [36], though the exact value is dependent on the mass of the nucleus in question and on the parameterization of its radius.

The radius R of the nucleus can, for example, be parameterized as

$$R_i = 1.25 \cdot A_i^{1/3}\,\mathrm{fm}\,. \tag{3.27}$$

This definition together with an offset of 5 fm is often called Cline's criterium for "safe" Coulex [37]. For heavy nuclei, it is also possible to utilize the approach [38] of radii of half density of the Fermi mass distribution

$$R_i = r_i(1 - \frac{1}{r_i^2})\,\mathrm{fm} \tag{3.28}$$

with the nuclear radii as defined via the liquid drop model given as

$$r_i = 1.12 \cdot A_i^{1/3} - 0.94 \cdot A_i^{-1/3}\,. \tag{3.29}$$

For our experiment the beam energy was chosen such that it does not exceed the limit as defined in [38].

3.4. Reduced transition strength

The reduced transition strengths introduced above in Equation 3.18 and Equation 3.21, for the electric and the magnetic case, respectively, are defined as the average of the matrix elements over the magnetic substates of the decaying state. They read

$$B(\pi\lambda; I_i \rightarrow I_f) = \frac{1}{2I_i+1} \sum_{\mu M_f} \left|\langle I_i M_i | \mathcal{M}(\pi\lambda,\mu) | I_f M_f \rangle\right|^2 \tag{3.30}$$

$$= \frac{1}{2I_i+1} \left|\langle I_i | \, |\mathcal{M}(\pi\lambda)| \, | I_f \rangle\right|^2 \ , \tag{3.31}$$

where the Wigner-Eckart Theorem is used.

This theorem relates matrix elements to the product of Clebsch-Gordan Coefficients $\begin{pmatrix} I_i & \lambda & I_f \\ -M_i & \mu & M_f \end{pmatrix}$ and reduced matrix elements via

$$\langle I_i M_i | \mathcal{M}(\pi\lambda,\mu) | I_f M_f \rangle = \tag{3.32}$$

$$(-1)^{I_i - M_i} \begin{pmatrix} I_i & \lambda & I_f \\ -M_i & \mu & M_f \end{pmatrix} \langle I_i | \, |\mathcal{M}(\pi\lambda)| \, | I_f \rangle\ . \tag{3.33}$$

The reduced transition strengths are a main result from any Coulex analysis and are related to the lifetime τ of the decaying state by

$$\frac{1}{\tau} = P_{if} = 8\pi\frac{\lambda+1}{\lambda((2\lambda+1)!!)^2} \cdot \left(\frac{E_\gamma}{\hbar c}\right)^{2\lambda+1} \cdot B(\pi\lambda; I_i \rightarrow I_f) \tag{3.34}$$

$$= \mathcal{C}_{\pi\lambda} \cdot (E_\gamma)^{2\lambda+1} \cdot B(\pi\lambda; I_i \rightarrow I_f)\,, \tag{3.35}$$

with the constants $\mathcal{C}_{\pi\lambda}$ that are relevant for this work given as

$$\begin{aligned}
\mathcal{C}_{E1} &= 1.59 \cdot 10^{15}\\
\mathcal{C}_{E2} &= 1.22 \cdot 10^{9}\\
\mathcal{C}_{E3} &= 5.67 \cdot 10^{2}\\
\mathcal{C}_{E4} &= 1.69 \cdot 10^{-4}\\
\mathcal{C}_{M1} &= 1.76 \cdot 10^{13}\ ,
\end{aligned}$$

with the γ-ray energy given in MeV, and the reduced transition strengths in $e^2 fm^{2\lambda}$ and $\mu_N^2 fm^{2\lambda-2}$, for the electric and the magnetic case, respectively.

As the reduced transition strengths are dependent on the wave functions of the connected states, they also encode the number of nucleons participating in the excitation process. The Weisskopf unit (W.u.) [39] reflects the number of nucleons, and is defined as

$$1\,\mathrm{W.u.} = \frac{1}{4\pi}\left(\frac{3}{\lambda+3}\right)^2 (1.2A^{\frac{1}{3}})^{2\lambda}\mathrm{e}^2\mathrm{fm}^{2\lambda} \tag{3.36}$$

for the electric case and therefore B(Eλ) values. The magnetic B(Mλ) values become

$$1\,\mathrm{W.u.} = \frac{10}{\pi}\left(\frac{3}{\lambda+3}\right)^2 (1.2A^{\frac{1}{3}})^{2\lambda-2}\mu_\mathrm{N}^2\mathrm{fm}^{2\lambda-2}\,. \tag{3.37}$$

The following equations give an overview of all transitions relevant in the scope of this work. It is notable that they are dependent on the number of nucleons in the nucleus only.

$$\begin{aligned}
1\,\mathrm{W.u.(E1)} &= 6.446 \cdot 10^{-4} A^{2/3}\,\mathrm{e}^2\mathrm{b}\\
1\,\mathrm{W.u.(E2)} &= 5.940 \cdot 10^{-6} A^{4/3}\,\mathrm{e}^2\mathrm{b}^2\\
1\,\mathrm{W.u.(E3)} &= 5.940 \cdot 10^{-8} A^{2}\,\mathrm{e}^2\mathrm{b}^3\\
1\,\mathrm{W.u.(E4)} &= 6.285 \cdot 10^{-10} A^{8/3}\,\mathrm{e}^2\mathrm{b}^4\\
1\,\mathrm{W.u.(M1)} &= 1.790\,\mu_\mathrm{N}^2\,.
\end{aligned}$$

Therefore, when we find a reduced transition strength of several tens of W.u. we consider it a collective transition with multiple nucleons participating. On the other hand, measuring a reduced transition strength of 1 W.u. reflects a transition with single-particle character. The exception to this classification are B(E1) values. Here, a value of 0.01 W.u. constitutes the approximate maximum that has been seen in octupole-collective nuclei [40, 8].

3.5. Second order processes

So far only direct excitations of a final state f have been considered. Though also second order effects, i.e., intermediate states n are allowed such that the final state is reached only after the excitation of the intermediate one. This is called multiple-step Coulex.

In second order, the transition amplitudes $b_{if}^{(1)}$, defined in Equation 3.10, need to be modified by a term that accounts for possible intermediate states, thus the second-order transition amplitudes become

$$b_{if}^{(2)} = b_{if}^{(1)} + \sum_n b_{inf} \, , \tag{3.38}$$

where

$$b_{inf} = \frac{1}{(i\hbar)^2} \int_{-\infty}^{\infty} \langle f | \, \mathcal{H}(t) \, | n \rangle \, e^{\frac{i}{\hbar}(E_f - E_n)t} dt \tag{3.39}$$

$$\cdot \int_{-\infty}^{t} \langle n | \, \mathcal{H}(t') \, | i \rangle \, e^{\frac{i}{\hbar}(E_n - E_i)t'} dt' \, . \tag{3.40}$$

The transition probability can again be calculated like in Equation 3.8, that is, taking the absolute square of the transition amplitude $b_{if}^{(2)}$. Here, unlike when only first order effects are considered, the relative signs of the single excitation amplitudes become important. This is due to the occurance of interference terms and not just quadratic terms. For details see [35].

Figure 3.1 shows the possible cases for multiple-step Coulex along with the first-order situation. In Figure 3.1a only one state is directly populated as discussed in Section 3.2, in Figure 3.1b the excitation of the final state f from the ground state i takes place via an intermediate state n. In the last case in Figure 3.1c, the intermediate state is a magnetic substate, which will be discussed in detail in Section 3.5.1.

3.5.1. Reorientation and spectroscopic quadrupole moments

The reorientation effect denotes the transition between two magnetic substates in an excited final state. Here, the spectroscopic quadrupole moment, i.e., the quadrupole moment in

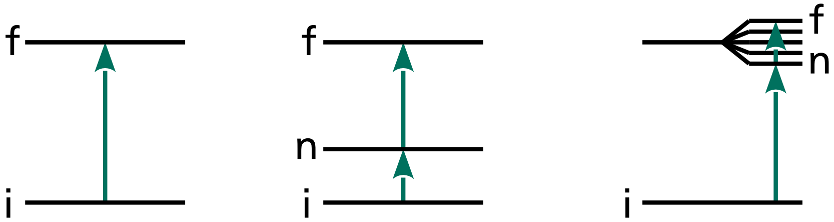

(a) Single-step Coulex. (b) Multiple-step Coulex. (c) Reorientation.

Figure 3.1.: Different types of Coulomb excitation. Single-step, two step via different state and two step via magnetic substate. For more information see text.

the laboratory frame, interacts with the time-dependent electric-field gradient during the excitation process.

The impact is strongest at close distances. The positive spectroscopic quadrupole moment enhances the Coulex cross section, while a negative sign leads to a reduction. The spectroscopic quadrupole moments Q_s are encoded in the diagonal matrix elements via the relation

$$eQ_s = \sqrt{\frac{16\pi}{5 \cdot (2I+1)}} \cdot \begin{pmatrix} I_i & \lambda & I_f \\ -M_i & \mu & M_f \end{pmatrix} \cdot \langle I| \, |\mathcal{M}(E2)| \, |I\rangle \ , \tag{3.41}$$

where $\begin{pmatrix} I_i & \lambda & I_f \\ -M_i & \mu & M_f \end{pmatrix}$ are again the Clebsch-Gordan Coefficients.

With the exception of laser spectroscopy for long-lived states, there are no other methods that grant direct access to spectroscopic quadrupole moments other than Coulex, which makes this technique a unique means of establishing the shape of the nucleus. A positive spectroscopic quadrupole moment signals an oblate shape, while a negative sign describes a prolate deformation.

For a detailed discussion see [35].

3.6. γ-ray emission as de-excitation path

The excitation process and the de-excitation happen on completely different time scales and can be considered separate and sequential. This is intuitive considering that the excitation process takes about $3 \cdot 10^{-21}$ s [41], while the de-excitation time depends on the lifetime of the respective states. These are typically in the order of 10^{-10} - 10^{-13} s. In other words, the interaction range for which the two nuclei are close enough to undergo Coulex, lies within the order of tens of fm, and the distance after which the nuclei deexcite in the order of µm or more.

The de-excitation is governed by the same multipole operators as the excitation, i.e., the same matrix elements can be used to describe the entire process. This also means that the detailed balance equation [42] is valid, which reads

$$B(\pi\lambda; I_f \to I_i) = \frac{2I_i + 1}{2I_f + 1} \cdot B(\pi\lambda; I_i \to I_f)\,. \tag{3.42}$$

The typical selection rules fulfilling angular and parity conservation apply for both excitation and de-excitation:

$$|I_i - I_f| \leq \lambda \leq I_i + I_f, \text{ but } 0^+ \nrightarrow 0^+ \tag{3.43}$$

$$\pi_i \cdot \pi_f = \begin{cases} (-1)^{\lambda} \text{ for } E\lambda\,, \\ (-1)^{\lambda+1} \text{ for } M\lambda\,, \end{cases} \tag{3.44}$$

where I_i and I_f are the total angular momenta of the initial and final state with the parities π_i and π_f, respectively. λ denotes the angular momentum carried by the emitted radiation. E stands for electric and M for magnetic character.

As mentioned before, reduced transition strengths are connected directly to the decay probability, which is inversely proportional to the lifetime of the respective states. This was already given in Equation 3.35.

3.7. Numerical methods

The first version of computer code extracting information from multiple-step Coulomb-excitation experiments was the one by Winther and de Boer [33] based on their semiclassical theory [31]. The later GOSIA code [43] was designed in 1980 to employ a fitting routine to extract the relevant matrix elements describing the interaction. It is based on a semiclassical coupled-channel Coulomb excitation least-squares search. GOSIA can be used for analysis, i.e., multidimensional fit of matrix elements to the data, and simulation.

The excitation cross sections of multiple Coulomb excitations are extracted from data utilizing a set of electric and magnetic matrix elements, with multipolarity E1 to E6 and M1 to M2, respectively. The kinematics-dependent intensities of the γ-ray transitions respresent a main input[2]. Together with spatial information on the used detector system, stopping powers, electronic conversion coefficients and other information, limits on the

---

[2] In the GOSIA manual the observed counts in γ-ray transitions are often referred to as yields, the same is true for this work.

matrix elements can be established in order to find the true set of matrix elements including their uncertainties.

GOSIA uses the least-squares static S for the minimization process [41], which is similar to a standard χ^2 function, with the difference of not normalizing towards the number of degrees of freedom, but rather towards the number of data points given. The S function consists of three parts and reads

$$S = \frac{1}{N}\left(S_\gamma + S_1 + \sum_i w_i S_i\right) , \tag{3.45}$$

where N is the number of total data points, including all yields and spectroscopic data such as branching ratios and lifetimes, but excluding upper limits. In the following each of the three parts is explained.

The first part consists of the contributions stemming from the difference between calculated γ-ray yield Y_k^c and the observed γ-ray yields Y_k^e as defined in each of the experiments I_e and the respective detectors I_d

$$S_\gamma = \sum_{I_e I_d} w_{I_e I_d} \sum_{k(I_e, I_d)} \frac{1}{\sigma_k^2}(C_{I_e I_d} Y_k^c - Y_k^e)^2 . \tag{3.46}$$

Here, $C_{I_e I_d}$ are normalization factors, $w_{I_e I_d}$ the weight of each data set as chosen by the user, and σ_k are the respective experimental uncertainties.

The second term is related to the observation limits, which are given by the user. In case that a transition is not observed, an upper limit can be used to restrict associated matrix elements such that physically unreasonable solutions are excluded. GOSIA expects this information as a ratio between the yield in the unobserved transition and a normalizing transition. Should the calculated yield ratio exceed that upper limit, then its contribution is accounted for via

$$S_1 = \sum_j \left(\frac{Y_j^c(I_e, I_d)}{Y_n^c(I_e, I_d)} - u(I_e, I_d)\right)^2 \cdot \frac{1}{u^2(I_e, I_d)} , \tag{3.47}$$

where $u(I_e, I)$ are the upper limits, $Y_j^c(I_e, I_d)$ is the calculated yield of the considered transition, and $Y_n^c(I_e, I_d)$ the yield of the normalizing transition.

The last contribution stems from the spectroscopic data $d_{n_i}^e$ and their uncertainties σ_{n_i} given, originating not from the current data set, i.e., literature values like branching ratios and lifetimes. Again, the calculated values $d_{n_i}^c$ are compared to the data:

$$S_i = \sum_{n_i} (d_{n_i}^c - d_{n_i}^e)^2 \cdot \frac{1}{\sigma_{n_i}^2} . \tag{3.48}$$

The least-squares static S is print out every minimization step as CHISQ, and is one of the main tools in finding the global minimum and thus the correct matrix elements describing the experiment.

For further details on the GOSIA analysis as performed in this work see Chapter 7 and, of course, the GOSIA manual [41]. An overview article on using GOSIA for the analysis of safe Coulex experiments can be found in [44].

4. Experiment

The experimental campaign was carried out at HIE-ISOLDE, CERN, in late 2016. The recent upgrade to HIE-ISOLDE, allowed for the first time in its history to accelerate radioactive beams up to 5.5 MeV/u.

This was a crucial increase that allowed to probe the structure of ^{142}Xe beyond the 4_1^+ state and populate higher spin states. This chapter starts with a detailed overview on the ISOLDE facility in Section 4.1, which will focus especially on the accelerator part of HIE-ISOLDE.

After that, the specifics of the used detector systems are discussed, namely C-REX in Section 4.2.1, a particle detector based on several silicon detectors, and the high-purity germanium-array MINIBALL in Section 4.2.2 serving as γ-ray detector.

4.1. HIE-ISOLDE

The ISOLDE facility [11] is located at the proton synchrotron booster of CERN, Geneva. Using the protons of the PS booster a large variety of nuclei is produced employing the ISOL technique (Section 4.1.1). These isotopes are thereafter bunched and charge bred (Section 4.1.2), accelerated and refocussed by several cavities and magnets, respectively, (Section 4.1.3), and eventually delivered to the MINIBALL experimental site.

4.1.1. Production target and mass separator

The ISOLDE facility is built around the concept of the eponymous ISOL method. The latter stands for Isotope-Separation OnLine, a method that provides the means to produce and select short lived isotopes for subsequent experiments. For the creation of the isotopes 1.4 GeV protons, provided by the PS booster, hit in our case a thick uranium-carbide target at one of the two primary-target areas of ISOLDE. Here, fragmentation, spallation and fission take place, producing a multitude of isotopes. The process with the highest ^{142}Xe yield is fission, i.e., the hit uranium nucleus absorbs the proton, thus becoming an excited compound nucleus. This nucleus then splits into two fragments of comparable mass [26].

The primary target is heated to 2000 °C to decrease the diffusion time of the isotopes through the thick target and the transfer line.

The following plasma-discharge ion-source [45] ionizes the nuclei employing 130 V electrons in between transfer line and electrode. These electrons interact with the gas mixture coming from the target and produce a plasma. For the case of the noble gas xenon, less volatile elements can be suppressed using a cold plasma source [46]. Namely, the transfer line is cooled with water, and an effective elimination of contaminants is accomplished. Besides the aforementioned plasma ion source, other ion sources, e.g., the resonant laser ion source [47], are available. Which ion source is used depends on the chemical properties of the isotope in question. The extracted 30 keV ions are afterwards moved to the magnetic separators.

Two targets are operated at the ISOLDE facility with their own mass separators, the General Purpose Separator (GPS) and the High Resolution Separator (HRS). The idea is that both target stations can be used in pulse-sharing mode [48]. For this work the HRS with the mass resolution $\frac{M}{\Delta M} \geq 7000$ was used [49].

After selecting the desired isotopes according to their mass, the 30 keV singly-charged ions are transported to the high-energy side of ISOLDE.

4.1.2. REXTRAP and REXEBIS

A crucial step in obtaining high-energy nuclei at the experimental site is increasing the charge state of the ions. This is readily apparent as high voltage is limited, and the maximum achievable energy of a linac is linearly dependent on the factor q/A with q being the charge state and A the mass of the ion. Therefore, the combination of REXTRAP and REXEBIS is installed to ensure further ionization of the incoming singly-charged ions.

REXTRAP [50] is a Penning trap that accumulates and bunches the beam so that it can be inserted efficiently into the subsequent charge breeder REXEBIS. This is necessary as the beam coming from ISOLDE's primary target is semi-continuous and the charge breeding process takes a certain time. This time is dependent on the required charge state.

Before entering the trap through the potential barrier, the ions are decelerated electrostatically. Collisions with a buffer gas cool the ions further so that they eventually accumulate in the potential minimum of the trap.

The following REXEBIS, which stands for Electron-Beam Ion-Source, produces highly charged ions by employing focused mono-energetic electrons [51]. The bunched and cooled ions provided by REXTRAP are detained by a potential caused by cylindrical electrodes in longitudinal and by the electron beam in radial direction. The electrons coming from an electron gun induce stepwise ionization. A variable potential can be applied for the extraction to meet the velocity acceptance of the subsequent radio-frequency quadrupole (RFQ).

In this experiment, the ^{142}Xe ions leave REXEBIS with a charge state of 33^+ after a breeding time of 192 ms. This means that the beam is pulsed at 5 Hz with a pulse length of 500 µs as opposed to being semi-continuous as before entering REXTRAP.

For additional information on both, REXTRAP and REXEBIS, see, for example, [52].

4.1.3. REX linac

Once the ions leave REXEBIS, they enter the mass separator leading to the REX linac, HIE-ISOLDE's post-accelerator [53]. Here, they are mass separated according to their A/q [54], with A being the ion's mass and q its respective charge state. In the case of ^{142}Xe, the ratio was equal to 4.30. The importance of the mass separator is reflected by that fact that the amount of residual gas ions stemming from REXTRAP and REXEBIS is greater than the desired charge-bred ions. The lack of suppression would lead to a huge contamination at the experimental site.

As first step of the actual acceleration process, the four-rod, $\lambda/2$-type RFQ enhances the ion's energy from 5 keV/u to 0.3 MeV/u. The following split-ring buncher ensures that the longitudinal beam parameters fit the subsequent 20-gap interdigital H-type structure (IH). The IH structure is a drift-tube linac-element that increases the energy further to 1.2 MeV/u. The next 3 structures are all 7-gap split-ring resonators, which provide the sequential acceleration up to a variable energy of 1.55-2.2 MeV/u. The last piece of the accelerator operating at room temperature is the 9-gap IH structure. Here, the ions achieve an energy of 3 MeV/u.

The following structures are superconducting and are part of the HIE-ISOLDE project [55]. During phase one of HIE-ISOLDE two out of eventually four niobium-on-copper sputtered superconducting RF cavities [56, 57] were installed allowing for a maximum energy of 5.5 MeV/u. The new high-energy beam-transfer line, equipped with modular units of doublet cells, achromatic 90 ° bends and final focusing triplets [53] delivered the ^{142}Xe beam to the MINIBALL experimental site with an energy of 4.5 MeV/u.

4.1.4. Beam characteristics

The beam at HIE-ISOLDE is pulsed, here at 5 Hz, due to the breeding time of REXEBIS, as mentioned before.

During operation, the ISOLDE operators can use several ways to check the targeting of the beam and its intensity. Usually, the beam tuning is done using a stable pilot beam as such a beam has a higher intensity and is more easily tracked. The beam's intensity can be checked moving in Faraday cups at several locations, or utilizing the MINIBALL-specific option to check the scattered beam distribution on the four quadrants of the forward DSSSD in real time.

The beam transmission rate for this specific experiment was 45 % for the low-energy part of ISOLDE, 7 % for REXTRAP/EBIS and 60 % for HIE-ISOLDE [58]. This means that we have comparetively big losses in the low-energy part and to some extent in REXTRAP/EBIS, where the slow extraction was applied but not optimized, compared to other runs in that year.

While we requested a beam intensity of 10^6 pps, the actual beam intensity was lower. This was not determined via the Faraday cups, which do not work at the low-intensity radioactive beam which was provided. Instead, the beam intensity can be estimated and cross checked using two approaches during the offline analysis. Firstly, the detected counts in the main transition of the target can be used. All required information on that nucleus and of the setup is available, so using either CLX/DCY [59] or GOSIA [43] the corresponding beam intensity can be determined. Secondly, the Rutherford cross section can be calculated and compared to the measured elastically scattered particles in the forward-facing DSSSD using either of the two programs. Both approaches result in the same average estimate of $1.2\ (2) \cdot 10^5$ pps.

The lower beam intensity had to be compensated by the use of a thicker secondary target.

The production target broke after its expected lifetime, though earlier during the measurements than the approved 240 h, resulting in an effective beam time of 90.5 h with the ^{206}Pb Coulex target. In addition to that roughly 30 h were spent on beam tuning by the ISOLDE team, adjusting electronics in the MINIBALL setup and measurements with the thinner ^{196}Pt Coulex target.

The lower beam intensity together with the shorter campaign time means that we could only accumulate roughly 10 % of the desired statistics.

4.2. Detector setup

This Coulomb excitation experiment is rather demanding, with a low-intensity radioactive beam, low cross sections for several of the interesting states, and a high beam energy. The MINIBALL setup is optimized for this case and has been operational at ISOLDE since 2001 [60].

The high-purity germanium-array MINIBALL allows the detection of γ-ray energies with a good resolution and high efficiency of 8 % at 1332 keV utilizing a smaller scattering chamber than the one used for C-REX [61]. For details on the γ-ray detector see Section 4.2.2.

The Doppler effect introduced due to the high beam energy, i.e., approximately 10 % of the speed of light, demands the usage of a particle detector to correct for Doppler broadening and Doppler shift affecting the emitted γ rays.

For the campaign in 2016 the C-REX particle detector was used as it is a detector array providing a much larger angular coverage. The details on the silicon detector are provided in Section 4.2.1. The downside to this setup as opposed to the standard Coulex setup employing merely a forward DSSSD, is a more voluminous target chamber. This creates a drop in MINIBALL efficiency down to 5 % at 1332 keV [62] due to the increased distance of the germanium crystals from the target. In addition to the particle detector, the target itself is housed in that chamber. Several targets were mounted on the target ladder, ensuring a choice of targets was selectable during the experiment, see Section 4.2.3.

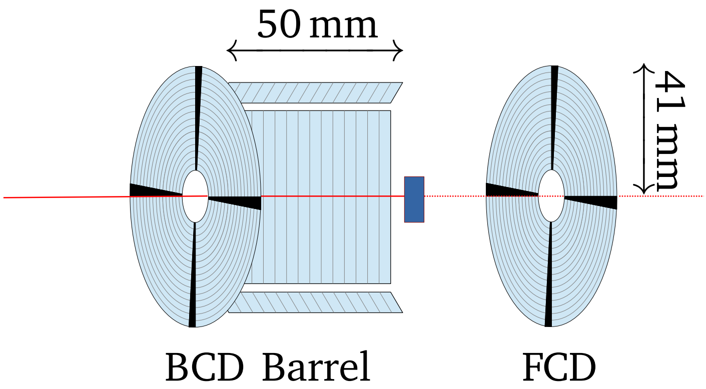

Figure 4.1.: Schematic representation of the particle-detector C-REX. Both DSSSDs mounted in forward and backward direction are shown together with three out of four barrel detectors, beam direction is from left to right. Target is marked in blue. Not to scale.

4.2.1. C-REX

The particle detector of this setup is called C-REX, which stands for Coulex-Radioactive Beam Experiment [63]. It is an adaptation of T-REX [62] that meets the requirements of Coulex experiments. It consists of a barrel part mounted upstream of the target and a set of two Double-Sided Silicon-Strip Detector (DSSSD) arrays that are found under extreme forward and backward angles. The two DSSSD detectors are also referred to as FCD and BCD, for the forwards and backwards facing DSSSD, respectively. Figure 4.1 shows a schematic drawing of C-REX, while Figure 4.2 shows C-REX mounted on target location, without attached cables.

A feature of the C-REX setup is that the DSSSD in forward direction is movable such that the distance between this particle detector and the target can be adjusted. The optimal distance can be selected with the requirement of the best angular coverage and the maximum tolerable count rates in mind. Elastically scattered particles are the predominant source of high rates and are expected under extreme forward angles, so moving the detector closer to the target avoids these. The choice for the distance lies in between approximately 2 cm and 6.4 cm. In the scope of this work the frame that controls this distance was recreated and decreases the distance in comparison to the setup used in [63] further. Too high count rates stemming from elastically-scattered beam particles posed a problem in earlier experiments

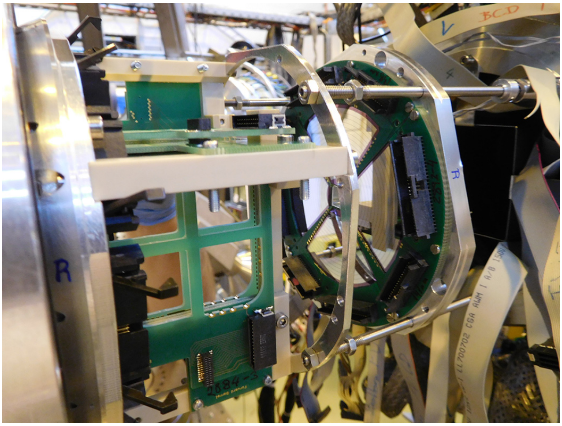

Figure 4.2.: Photograph of particle-detector C-REX mounted on target position. Beam direction is from left to right. Cables not attached. Back DSSSD is not visible, barrel backside and forward DSSSD are shown.

[10], but are circumvented by putting the forward DSSSD as close as possible to the target. The closest distance is dictated by the cables, which still need to be attached to the DSSSD.

The exact distance during our experiment was determined in the offline analysis, which is discussed in Section 5.10.1.

Barrel detectors

The barrel part of C-REX consists of four silicon-strip detectors. Figure 4.3 shows an unmounted barrel detector. The thickness of the detectors is 141(2) μm, with an active area of 50 x 50 mm. Each detector is segmented into 16 resistive strips, providing a front-side signal stemming from a single strip and an unsegmented rear-side signal. The silicon detectors cover the angular range of 102-153 ° in the laboratory system. As the backwards C-REX part is fixed, their position cannot be altered unless the frame is exchanged. The detector is mounted such that the strips are orientated perpendicular to the beam direction.

The signals from the resistive strips of the barrel detector are first preamplified in a charge-sensitive MPR-64 preamplifier [64], then shaped with a STM-16 unit [65] and eventually digitized in MADC-32 modules [66].

The rear-side signals are shaped and preamplified employing a MSI-8 unit [67]. The out-going energy signal is processed by an MADC-32 module. Fast timing signals are also obtained from the MSI-8, which are sent to a constant-fraction discriminator to obtain the

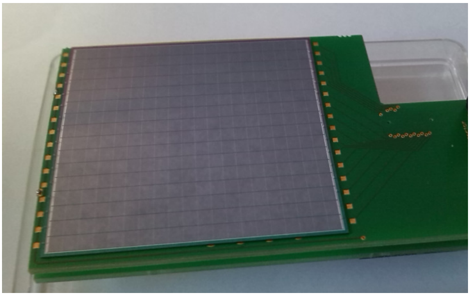

Figure 4.3.: Photograph of a silicon barrel detector, which is part of the particle-detector array C-REX.

trigger signal.

CDs

The two CD detectors consist of Double-Sided Silicon-Strip Detectors. They are of type QQQ2 by Micron Semiconductor Ltd. [68]. Each DSSSD is built from four quadrants with an active area of radius 9 mm to 41 mm and 81.6 ° in φ. The thickness of the detectors is 140(2) µm for the forward-facing ones and 486(6) µm for the backwards-facing detectors. The maximum range of ^{142}Xe in silicon at the given beam energy is 60 µm, hence the nuclei are fully stopped in both the detectors. The backwards-facing DSSSD covers an angular range of 153-172 ° in the laboratory frame.

The quadrants are made up from 16 independently readable annular strips looking upstream and 24 strips downstream. Within the scope of this work, the frontside annular strips will be called rings, while the rear-side strips will be called strips, although they are often referred to as segments in other works. The rings have a pitch of 2 mm, but an active width of 1.9 mm. The strips have an opening angle of 3.4 °. The center 16 strips on the rear side are electronically coupled to eight strips. Figure 4.4 shows the entire forward-facing DSSSD particle detector.

Multiplexing

Compared to the standard Coulex setup, consisting of only one DSSSD mounted in forward direction, C-REX provides significantly more channels. This fact requires a set of electronics that can handle the additional data input.

In order to get the increased number of channels into the data acquisition, 32-channel fast multiplexers (abbr. MUX) [69] by Mesytec were used for the read out of the DSSSDs.

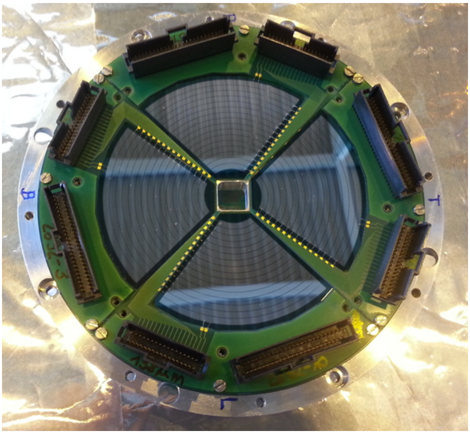

Figure 4.4.: Photograph of the forward facing double-sided silicon-strip particle detector mounted on its frame.

Each of the MUX-32 modules consists of a set of two MUX-16 submodules.

These MUX-16 modules, in turn, allow for up to 16 input channels to be multiplexed. They can cope with a maximum of two coincident signals above a set threshold within a 30 ns time frame. Otherwise a reject signal is produced and the event data discarded.

The output of a good event, i.e., a maximum of two input signals, is encoded in a total of 5 output signals: The trigger signal containing the timing information of the event is the only shared piece of information. For both input signals, the ID of the input channel and the amplified and shaped energy signal are returned. A distinction needs to be made between the two signals only in the sense that the first signal is always the one with the lower input ID.

Since the two submodules of the MUX-32 are connected by the same bus, the ID signals are generated such that the two groups possess a distinct offset. This guarantees that the association between detector and ID signal is never lost.

For our setup it is mandatory that ring and strip signals do not go onto the same bus, as one physical event should always produce at least one ring and one strip signal and with this the maximum signal input is already reached. In fact, for interstrip events one physical hit produces two signals on neighboring rings or strips.

Therefore, e.g., the ring signals from the top FCD quadrant and the top BCD quadrant are put together into one module, as a hit on both these detectors can kinematically not stem from a single physical Coulex event. The strip signals are handled in the same manner.

For an in-depth discussion of the multiplexers used for this experiment type see, for

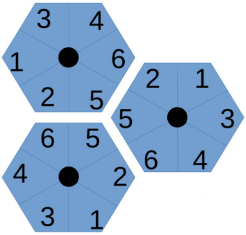

Figure 4.5.: Scheme of a MINIBALL triple cluster, providing a core-energy signal per crystal along with six segment signals.

example, [63].

4.2.2. MINIBALL

MINIBALL is a germanium array that has served as γ-ray detector at ISOLDE and other facilities for many years. It is designed for low-multiplicity γ-ray detection following reactions with radioactive ion beams.

The array consists of 24 high-purity germanium crystals, which are encapsulated in aluminum cans. Three of those are then housed together in one cryostat, making it eight triple clusters. Picture 4.5 shows a scheme of such a cluster including the numbering of the segments. The clusters are mounted on a flexible frame, that allows for a dedicated positioning following the requirements of each experiment. In this experiment, the clusters were mounted in such a way that they were as close as mechanically possible to the target chamber, without touching each other or any surrounding electronics.

The germanium crystals are cooled with liquid nitrogen and are six-fold segmented, providing a core-energy signal and six segment signals per crystal. This segmentation improves the spatial resolution and therefore the Doppler correction considerably.

Figure 4.6 shows a photograph of two MINIBALL triple clusters mounted at the MINIBALL experimental site at CERN.

The read out of the MINIBALL signals is handled by Digital Gamma Finder (DGF XIA) modules in triggerless mode. These modules provide the needed timestamps for the detected γ rays. During the 800 µs long RF window, referred to as “beam-on” window, the beam nuclei hit the Coulex target. During this time frame, the data acquisition registers all information by the full detector setup. A second “beam-off” window is used to allow for a reliable background subtraction.

For a dedicated overview on MINIBALL see [61].

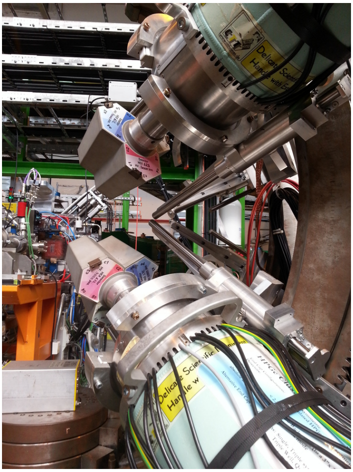

Figure 4.6.: Photograph of two MINIBALL triple clusters mounted on their frame at the MINIBALL experimental site. Looking upstream, with perpendicular offset to the beam line.

4.2.3. Secondary target

Generally, a Coulex target for beam excitation needs to fulfill several requirements. It must be preparable in an isotopically pure fashion and be solid at room temperature. For this experimental setup it has to be possible to create a thin foil that can be mounted on the target ladder. The isotope has to be stable to prevent daughters from interacting with the incoming beam, warping results.

Furthermore, the kinematics for the scattering process at the given beam energy must be such that beam and target are separable using the particle detector, as discussed in Section 5.8.2.

Additionally, the relevant known transition energies for beam and target isotope are to lie sufficiently apart to be separable. This makes it mandatory that adequate literature of the nuclear structure of the target nucleus is available.

Two well fitting reaction partners for ^{142}Xe are ^{196}Pt and ^{206}Pb.

Figure 4.7 shows a photograph of the choice of targets mounted on the target frame during the experiment.

In order to help with the beam-tuning process, initially the empty target frame was used on target location. As no scattered events were detected by the forward-facing particle detector, subsequently the ^{206}Pb target was chosen. At 4 $\frac{\mathrm{mg}}{\mathrm{cm}^2}$, this rather thick target is perfect

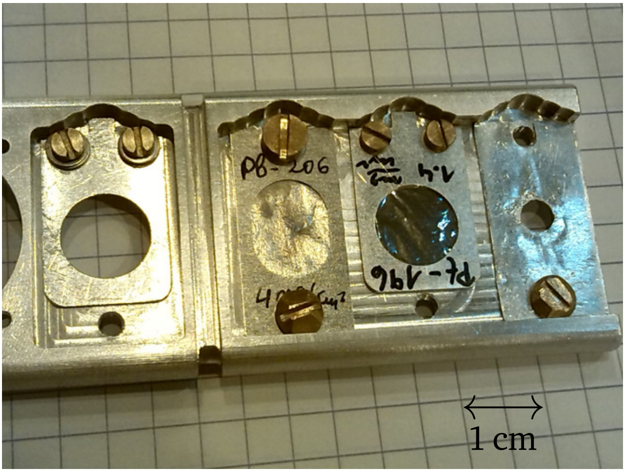

Figure 4.7.: Photograph of choice of targets mounted on the target ladder during the experiment. From left to right: Empty target frame, ^{206}Pb target with 4 $\frac{\text{mg}}{\text{cm}^2}$ thickness, ^{196}Pt target with 1.4 $\frac{\text{mg}}{\text{cm}^2}$ thickness, which turned out to not be isotopically pure, and a frame with a hole of 4 mm diameter.

for starting measurements, as the higher thickness results in more scattered beam nuclei, which are detected by the four quadrants of the forward DSSSD. A uniform distribution across those quadrants indicates that the beam is fairly centered.

At the very start of the actual data collection the 1.4 $\frac{\mathrm{mg}}{\mathrm{cm}^2}$ thick platinum target was used. The properties of this target are discussed in Appendix B.

Eventually, in order to compensate for the low beam intensity and to acquire sufficient statistics within the given time frame, the thicker ^{206}Pb target was selected to serve as Coulex target. The downside to this decision was increased straggling of the beam in the target perpendicular to the beam direction, leading to an increased smearing of the kinematics.

5. Data preparation

This chapter covers the conversion from so-called MED files to Doppler-corrected spectra. The latter, combined with the spatial information of the detectors, is used to determine reduced transition strengths and spectroscopic quadrupole moments using GOSIA (Chapter 7).

5.1. Data format and program structure

The data for this experiment was taken using the MARABOU data acquisition system [70]. Data readout and data transport were based on the Multi Branch System (MBS) [71], while the data storage was managed within CERN's ROOT framework [72].

The data was then analyzed using a program package based on C++ and the ROOT framework.

The code was built upon the works [73, 74, 75, 63], who have written and modified the original program. Within the scope of this work, parts of the program package were heavily modified or newly written to meet the needs of this specific experiment.

There are distinct levels in the data flow, which are handled in consecutive steps. Furthermore, additional programs were available or created helping to determine, for example, fitting parameters and the spatial information of the detectors.

As a first step the **event building** process transforms binary MED [70] to ROOT files. This is necessary as the data acquisition is triggerless, so events need to be sorted during the analysis using a set 1 µs correlation window.

After that, the **calibration** of the detector system is performed. This includes, for example, the calibration of the particle detectors (Section 5.3.3 and 5.4) and the energy and efficiency calibration of the γ-ray detector MINIBALL (Section 5.2).

On the **reconstruction** level follows the creation of physical objects, i.e., γ rays and particles. Here, for example the trigger-point dependence on the energy (Section 5.7.2) is handled and the addback routine (Section 5.2.3) of the MINIBALL detector is implemented, as well as the beam shift (Section 5.10.2) performed. The eponymous reconstruction of undetected particles using the equations given in Appendix A also takes place in this step.

Lastly, the **high-level analysis** is completed, combining particle and γ-ray information. Event types are specified (Section 5.8.1) and the background subtraction performed based on timing information.

5.2. Calibration of the MINIBALL detectors

The γ-ray array MINIBALL needs to be energy- and efficiency-calibrated. The energy calibration is necessary as the output, which goes into the data stream, is given in channels instead of actual energy. The efficiency of the array is expected to follow a typical energy-dependent behavior, which needs to be taken into consideration when evaluating the number of counts in each peak.

5.2.1. Energy calibration

For the energy calibration a standard ^{152}Eu source is used. Its most prominent γ-ray decay radiation ranges from 122 keV to 1408 keV [76], the energy range in which the γ rays stemming from the excited energy levels in ^{142}Xe are expected to lie. Using the known ^{152}Eu energies, the energy calibration function

$$E(C) = m \cdot (C + b) \tag{5.1}$$

was used to connect the channels C, which were read directly from the data, to the expected energy E. The parameters m and b were fitted for each core.

A good tool to check the energy stability of MINIBALL during the experiment are the peaks stemming from the β-decay of ^{142}Xe and its daughters. When comparing a run during the early phase of the experiment with one at a later stage some deviations are, unfortunately, visible. While the energy shift is smaller than 0.5 keV in most crystals, there are some which show an offset of smaller than 1 keV and one for which the deviation is bigger than 1 keV. Moreover, a systematic change is observed in 5 crystals, though it is smaller than 1 keV.

In order to correct for this, the γ rays from the beta decay are used. The advantage of this over using the Doppler-corrected spectra manifests in a better resolution and independence from effects caused by the in-flight emission of the γ rays. It is also a crucial correction as otherwise the determination of the angles of the MINIBALL crystals as described in Section 5.10.3 will yield warped results. This is especially true as the mean of the peak is attributed an additional factor putting a bigger weight on it.

Figure 5.1 shows a fit to the six peaks used in a single crystal with their respective origin. This range was chosen such that these energies lie in the appropriate range to provide a good energy calibration for the excitation energies seen in ^{142}Xe.

By considering each experimental run separately, the time dependence could be determined and taken into account. In order to have sufficient statistics for an automatic fit in each run i, the immediately neighboring runs $i-1$ and $i+1$ were added up as well. This allowed for an improved run-dependent energy calibration for each individual crystal.

This calibration resulted in nicely-corrected MINIBALL crystals as displayed in Figure 5.2, where the Doppler-corrected γ-ray energies are shown in relation to their crystal ID.

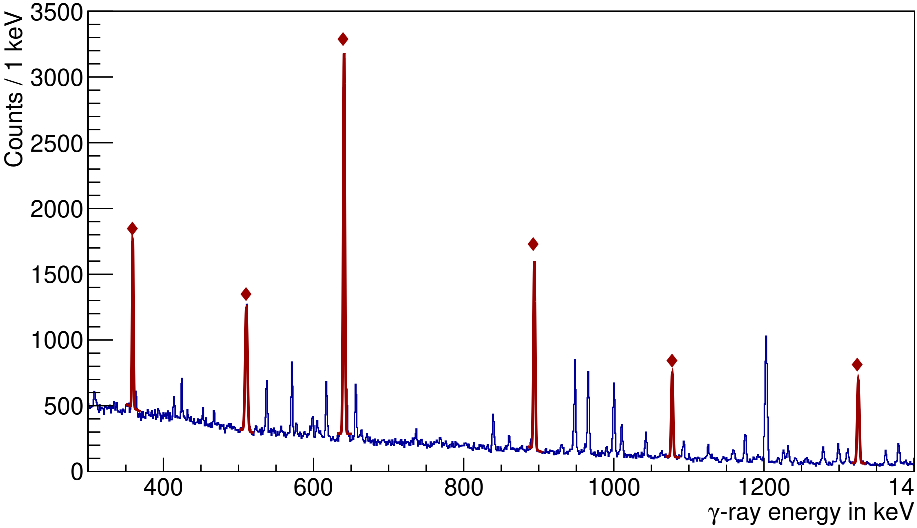

Figure 5.1.: Beta-decay γ-ray energies as detected by MINIBALL crystal 18 in one subrun as described in text. The marked peaks were used for the run-dependent energy calibration.

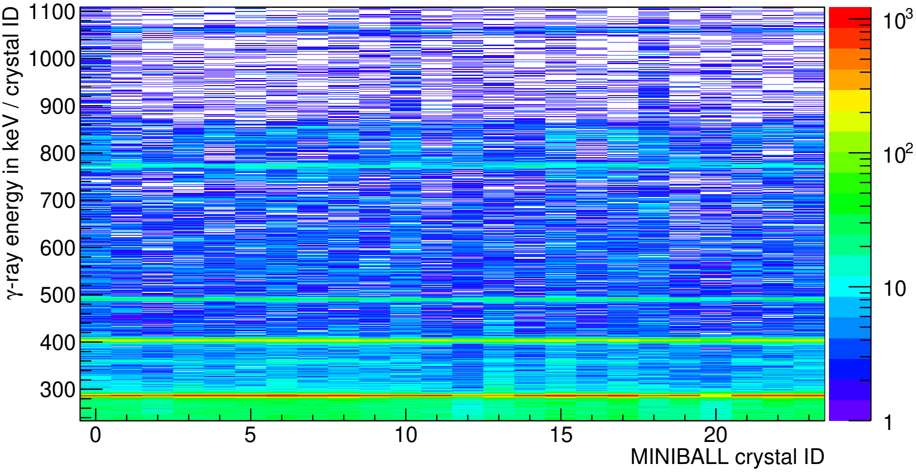

Figure 5.2.: Doppler-corrected γ-ray energies per MINIBALL crystal.

5.2.2. Efficiency calibration

The relative energy-dependent efficiency is determined using the same ^{152}Eu source mounted in target position.

As a phenomenological function reproducing the observed energy-dependent efficiency $\epsilon(E_\gamma)$, the function

$$\epsilon(E_\gamma) = e^{a_1 + a_2 \cdot \ln(E_\gamma) + a_3 \cdot \ln(E_\gamma)^2 + a_4 \cdot \ln(E_\gamma)^3} \tag{5.2}$$

is used. The parameters a_i were fitted for the full MINIBALL array using their respective core-energy signals. The relative efficiency for each data point is defined to be

$$\epsilon_{\text{rel}} = \frac{C_E}{I_E} \cdot \frac{I_{245\,\text{keV}}}{C_{245\,\text{keV}}} , \tag{5.3}$$

with the counts in each peak C_E, their literature intensity I_E [76], and the normalizing peak with an energy of 245 keV.

The associated uncertainty for the efficiency function is in the order of 5-6 %, and is energy dependent. The uncertainty stems from both fit and intensity uncertainties found in literature.

Thus, the overall uncertainty of the γ-ray counts in the peaks are governed by the efficiency uncertainties for high statistics transitions, and by the statistical uncertainty and underlying structures for low-count transitions.

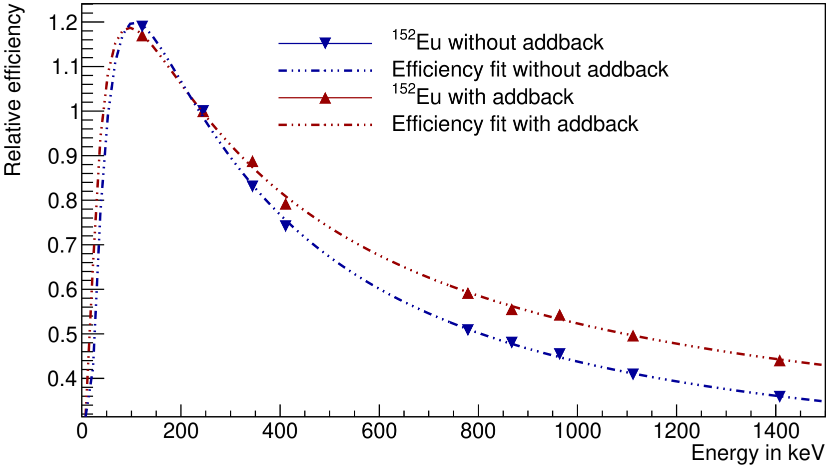

Figure 5.3.: Efficiency function as determined using an ^{152}Eu calibration source, shown in blue without any addback and in red with advanced addback applied as discussed in Section 5.2.3.

A distinction can be made between the respective efficiencies of MINIBALL without any addback and including addback. Figure 5.3 shows the increased detection efficiency of higher γ-ray energies using the addback routine described in Section 5.2.3.

It is important to note that the efficiency correction needs to be done using the detected γ-ray energy and not the Doppler-corrected energy determined using Equation 5.5. Due to this, the efficiency-correction factor defined as

$$f_\epsilon = \frac{1}{\epsilon(E_\gamma)} , \tag{5.4}$$

is applied when creating the final γ-ray energy-spectrum as opposed to afterwards.

5.2.3. Addback procedure

So far, the MINIBALL array does not have an anti-Compton shield, though a prototype for a dedicated escape-suppression shield has recently been developed and tested [77].

Due to this lack of Compton suppression, it is not only possible for a Compton-scattered γ-ray to be detected in more than one segment of the same crystal or in two neighboring MINIBALL crystals of one cluster, but also in two neighboring clusters. These cases must be addressed during the addback routine. For this purpose, it is practical to set the addback timing window to ± 100 ns [1].

For the first case, i.e., the detection in at least two segments of the same cluster, a distinction can be made: For the first subcase, more than one segment signal has the same time stamp as one single core. Here, the core-energy signal is used as energy information and the spatial information of the segment with the highest energy deposit is stored. In the other instance, where one segment has the same time stamp as their respective core, yet a distinct one from the other core-segment pair, the core-energy signal of both events is added up and assigned as energy, while again the segment with the highest energy signal determines the position.

In the other case, that is, two distinct clusters being hit, an additional restriction is applied: Not only must the timing condition be met, but the angle of the segments with the maximum energy is to lie within 36 ° as well. The exact cut-off angle was determined by looking at high-coincidence events of neighboring clusters for which outer segments show a significant enhancement.

Figure 5.4 shows the respective differences it makes for a spectrum if no addback, within-cluster addback, and advanced addback is used. In the low energy region shown in Figure 5.4 (a) the peak-to-background ratio goes up drastically once within-cluster addback is applied. The ratio improves further when advanced addback is used, yet less significantly. In the high-energy region shown in Figure 5.4 (b), the same is true. The only difference is that the background in both cases remains widely untouched. Note, that when comparing the advanced-addback routine to the within-cluster addback routine, additional counts appear within the peak region and not in the background area.

Looking at the counts in the convoluted peak at 895 keV stemming from the β-decay of both ^{142}Ba and ^{142}La, the background-subtracted integral-ratio $\frac{\text{Counts}}{\text{Counts}_{\text{adv. addback}}}$ is (85.5 ± 0.2) % for the spectrum created without addback enabled and (99.0 ± 0.2) % for within-cluster addback. This validates the slight edge the advanced addback routine has over the within-cluster addback procedure.

Figure 5.5 shows the particle-γ-γ coincidence matrix for no addback, within-cluster addback and advanced addback. The advantage of using an addback algorithm is obvious and highlighted by the weakened Compton-scattered events originating from the two strongest transitions.

Applying an addback algorithm to the data also affects the energy-dependent efficiency, a fact that is discussed in detail in Section 5.2.2. The desired consequence of applying addback is, of course, the increase of the peak-to-total ratio of all, but especially energetically higher-lying, detected transitions. Figure 5.6 shows a section of the Doppler-corrected

---

[1] The timing resolution of the MINIBALL time stamps is 25 ns [61]. Fixing the addback timing condition to be between 100 ns and 125 ns reveals still an enhancement of sensible coincidences in neighboring segments in some of the clusters. Nevertheless, there is no systematic improvement of the peak-to-background ratio at higher γ-ray energies. Therefore, the addback timing condition was set to ± 100 ns.

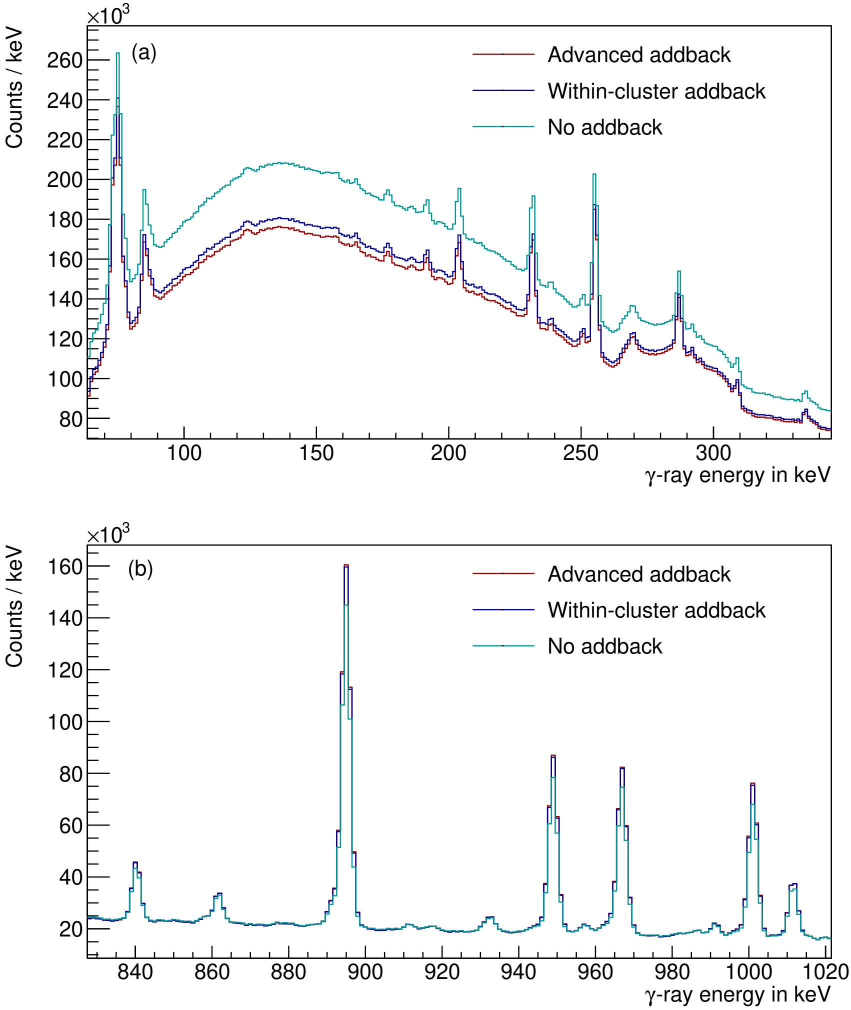

Figure 5.4.: Beta-decay spectra. No Doppler correction applied. Differences caused by different addback algorithms are shown. An exemplary low-energy range (a) and an exemplary higher-energy range (b) are depicted.

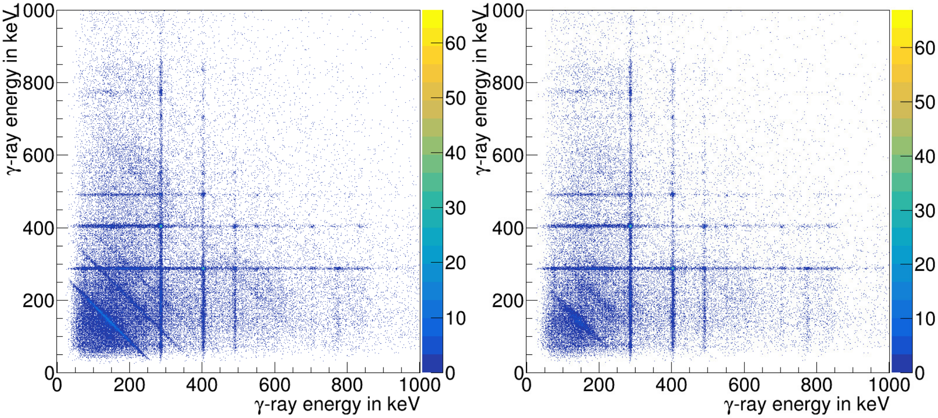

(a) Without addback.

(b) Within-cluster addback.

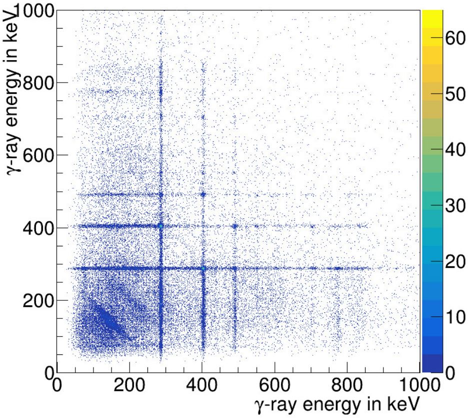

(c) Advanced addback.

Figure 5.5.: Particle-γ-γ matrix without addback (a), with within-cluster addback (b) and with advanced addback (c) applied. “Beam-on” events only, full statistics.

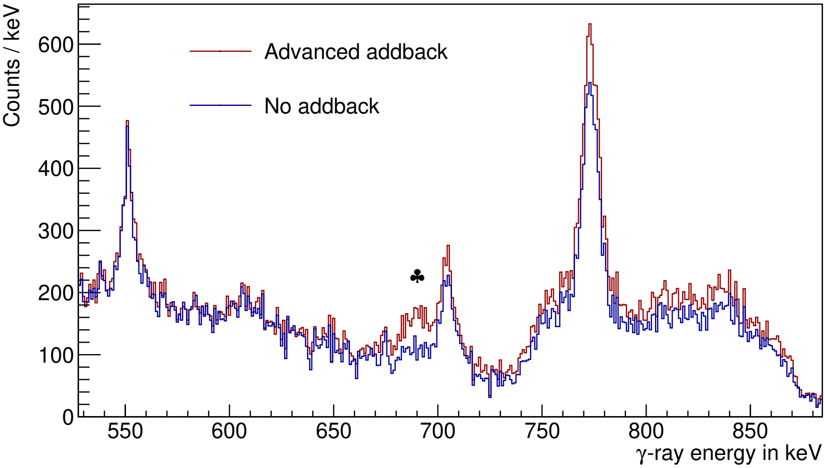

Figure 5.6.: Doppler-corrected γ-ray energy-spectrum with applied advanced addback in red and without addback in blue. The sum peak at 287 keV + 404 keV = 691 keV is highlighted.

γ-ray energy-spectrum. The aforementioned positive impact on the detected counts in the peaks is clearly visible. A negative side effect is the appearance of sum peaks, especially at 287 keV + 404 keV = 691 keV, which is in the vicinity of the 703 keV line, complicating the determinabilty of the exact number of counts in that transition.

5.3. Calibration of the CDs

Two CDs are part of the particle detector array and require consideration during the calibration process. Firstly, as their signals are multiplexed using a MUX module, the process needs to be disentangled before actually being able to use their output in the further analysis. The demultiplexing procedure is described in Section 5.3.1.

Secondly, the stability of the CD properties over time is investigated in Section 5.3.2.

Lastly, the energy signals are analyzed in detail. However, due to the pulse height defect [78], a real energy calibration is not performed. Throughout the process, multiple corrections are necessary to account for various detection effects. These are discussed in Section 5.3.3.

5.3.1. Demultiplexing

The signals of both CDs, which go into the data stream in a multiplexed form as described in Section 4.2.1, need to be demultiplexed during the offline analysis. As mentioned before, the 16 rings of the front side of a FCD quadrant are multiplexed together with the same quadrant of the BCD. The same is true for the 16 strips of the back side. In this section the necessary steps to extract the ID signals are discussed.

The MUX-16 units provide two ID signals, which reflect the ID of the rings and strips, respectively. This allows for the assignment of the correct ID of each ring (strip). Figure 5.7 shows typical multiplexed spectra of the strips of one quadrant. For single hits, 16 peaks are visible, as is expected. The center eight peaks contain approximately twice as many counts as the outer eight. This is easily understandable as the center strips comprise two separate physical strips each, which are read out together electronically.

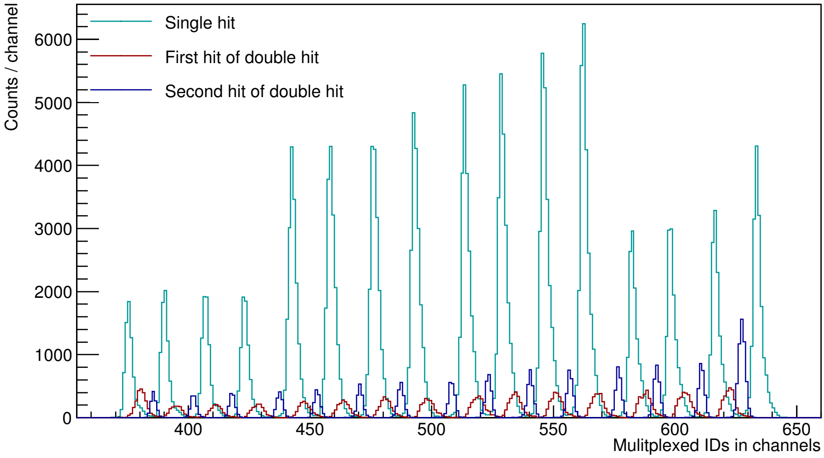

Figure 5.7.: Multiplexed strip-ID signals of quadrant 2 for one run only. Single hits as well as first and second hits of a double hit are each shown separately.

The signals of the double hits, i.e., the multiplexed information of the first and second hit, encode 15 instead of 16 separate IDs. This is due to the fact that the MUXes always assign the lower ID of a double hit to the first channel. Also, the double-hit signals are shifted with respect to the single hits, which merely means that the demultiplexing process must be performed separately for events with one hit only and the case of double hits.

For the ID assignment, the location of the minimum between two IDs is used as the ID signals are not symmetric, and therefore the use of the center as determined by a Gaussian fit turned out to be problematic.

The multiplexed strip-spectra for the other quadrants are quite similar to the one shown here, but exhibit a smaller shift between single-hit and double-hit events. This means that for all quadrants the minima in between the strips must be identified individually. The same is true for the spectra for the rings, which are comparable to the strip spectra and therefore handled the same way.

Figure 5.8 shows an exemplary plot of second-hit IDs over first-hit IDs of the strips of one quadrant for one run only. The diagonal line reflects typical double-hit events caused by one detected particle in the interstrip region, i.e., the detector response to one nucleus hitting an area that causes a signal in two adjacent strips instead of only in one strip: The signal encoding the first-hit ID is lower than the second hit ID with a maximum at neighboring strips. Other events, i.e., double hits on non-adjacent strips, are also possible as two unrelated particles can be detected simultaneously in the same quadrant. They can only appear on the upper left side of the diagonal as the first hit is assigned as the event with the lower ID in a double hit.

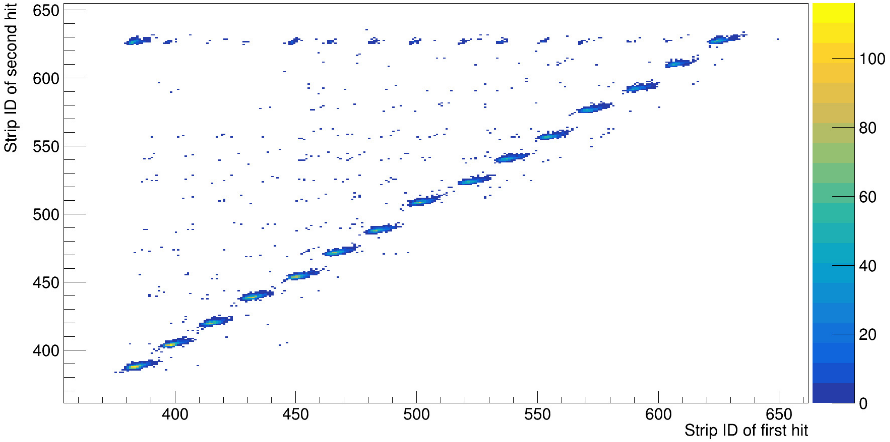

Figure 5.8.: Second-hit ID over first-hit ID of strips of one quadrant for one run. Only double hits on strips are plotted.

A feature visible in all strip spectra is the increase in statistics of strip 15. This increase is not physical in the sense that it does not stem from any special scattering event. Additionally, as such a feature was not visible using the standard electronics setup, this has to be a property of the MUX module. These double hits led to several challenges during the analysis, some of which are discussed in Section 5.3.3.

Plotting the rings in the same way as was done for the strips in Figure 5.8 exhibits the same behavior as for the strips except for the strip 15 feature.

5.3.2. Stability over time

The positions of the minima of the multiplexed signals discussed in the last section do not depend on the run number and are therefore not time dependent. This is not true for the energy signals. The energy-signal output of the rings and strips of the silicon detector changes slightly over time. This can happen when an actual change of the detector's physical properties occurs, for example caused by radiation damage due to the high beam intensity. An indication for damages to the detector are increasing reverse currents which were observed during the experimental campaign. Moreover, a possible time-dependent beam-shift has similar consequences.

Irrespective of what creates the time dependence, this must be corrected: The subsequent calibration steps require sufficient statistics, so it is quite important to be able to add the statistics of multiple runs together into sets, which can thereafter be treated as one. The key sum-up condition is whether the difference in kinematics introduced by the beam shift, i.e., how big the related offset is, is small compared to the smearing effect caused by both the width of the detector strips as well as the finite size of the beam spot. Based on this requirement two distinct sets were created as discussed in Section 5.10.2.

As a first step, the ring and strip energies are normalized to their respective counterparts in the reference run. To facilitate this, an automatic fit to each single-hit energy is performed. Double hits are not considered here, as they show additional characteristics that require detailed correction with sufficient statistics. Further special features discussed in the subsequent section are also excluded.

5.3.3. Energy signals

When considering the interaction of the scattered nuclei with the silicon detector, it is instructive to keep in mind that the maximum penetration depth for the impinging high-energy ^{142}Xe is about 0.06 mm, equivalent to a little less than half the nominal detector thickness of 0.14 mm. Therefore the xenon nuclei are fully stopped within this detector. The same is true for the ^{206}Pb nuclei.

In an optimal world, we expect the double-sided silicon-strip detector to detect the same energy on the front and back side of the detector. In fact, a detector of this type works based on the principle of charge-carrier separation. I.e., a particle hits the detector and creates a cloud of positively charged holes and negatively charged electrons that drift towards strips and rings, respectively. The number of positive and negative charge carriers should be equal, resulting in the same number being measured on both sides.

Taking this into account, the hit pattern, when plotting the strip energy over the ring energy, should show a straight line starting at the origin with a slope of one. Figure 5.9 shows the raw distribution of strip over ring energy considering only quadrant 1 without any demultiplexing done. The other quadrants show qualitatively the identical result. Note that double hits are not added up here. This distribution is significantly more complicated than the expected straight line and is discussed in this section. Furthermore, the applied corrections are explained.

In Figure 5.9, the two areas marked with (1) are rather low-lying in energy and actually disappear once multiplexing is done. They belong to a noise peak below approximately channel 350 in the ID spectra. (This may be the reject signal as discussed in Section 4.2.1, or actual noise.) This peak is not shown in Figure 5.8 as it is too low lying and easily interpreted as not physical and excluded.

The area with the expected straight line with a slope of one, denoted as (2) in Figure 5.9, shows a superposition of several straight lines stemming from different ring-strip combinations. Focussing on one specific ring-strip combination, as is done in Figure 5.10a, shows that one straight line remains in this case. The events shown in this plot are exclusively single hits on both rings and strips. The strip is one of the outer strips, and not one of the electronically coupled ones in the center of a quadrant.

Area (3) in Figure 5.9 comprises double hits on rings. This is easily determined by requesting only double hits on rings with a single hit on a strip. The result is the marked area. Remember that in this figure the energy shown is the energy as detected by a single ring or strip no matter if there was a second hit on another. Part of the energy deposited in the detector is detected by the other hit ring, therefore the ring energy appears to be lower. A detection of energy on two rings rather than one only takes place if the particle hits in the interstrip region or close to it [79, 80]. Note that the interstrip region and its effects are not necessarily equal to the geometric interstrip region but reach beyond [81]. Here, a number of different effects can take place such as charge sharing and inverted-polarity signals [79, 81].

It is instructive to add up the energies resulting from both rings and plot that energy together with the strip energy as is done in Figure 5.10b. Comparing the maximum energy with the events where only a single ring and strip were hit reveals a persistent decrease for both ring and strip energy. A possible explanation is charge-carrier loss in the interstrip area of the rings. Typically, a SiO_2 passivation layer is placed in between the strips to prevent any current on the surface between the two readouts of the rings. This leads to an effective positive surface charge close to this layer, which results in significant bending of the electric field lines [79]. The created electrons can thus be trapped in the region, either recombining or remaining trapped longer than the pulse shaping times. The slight curvature can also be understood by considering that particles, which hit the center of the inter-ring region interact with more of the SiO_2 layer, therefore losing more charge carriers, while particles hitting the sides are less affected.

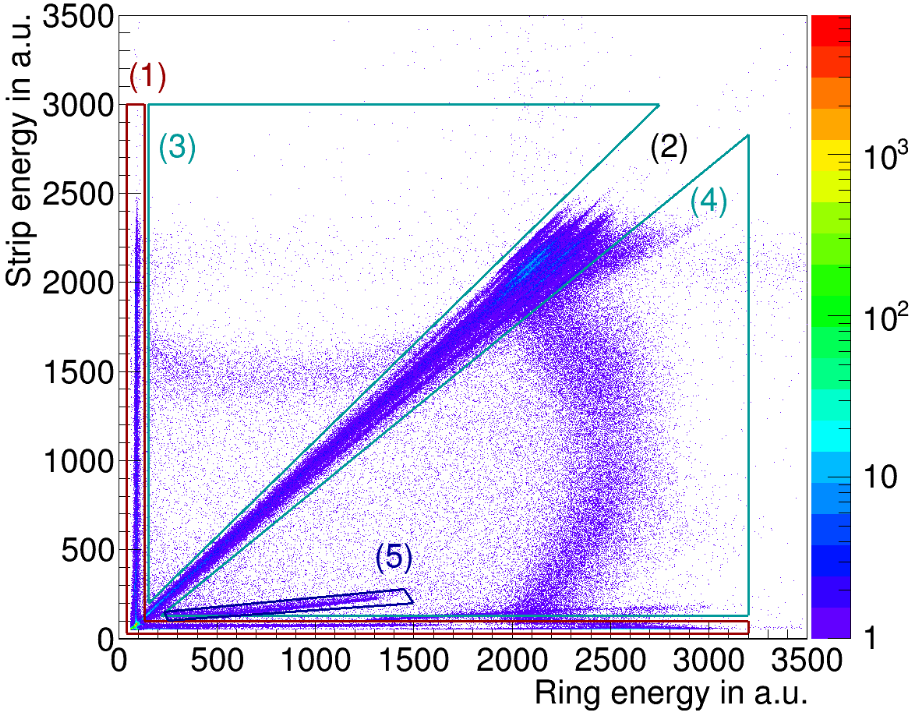

Figure 5.9.: The strip vs. ring energy of one quadrant prior to any calibration and correction is shown. Neither ring nor strip energies are summed for events where neighboring rings or strips were hit. The region marked with (1) stems from the MUX modules and is discarded. Region (2) consists of single hits on both ring and strip, while region (3) is comprised of double hits on rings, and region (4) shows double hits on strips. Region (5) originates from the malfunctioning MUX strip channel 15. For a detailed discussion see text. Summed energies are given in Figures 5.10 and 5.11.

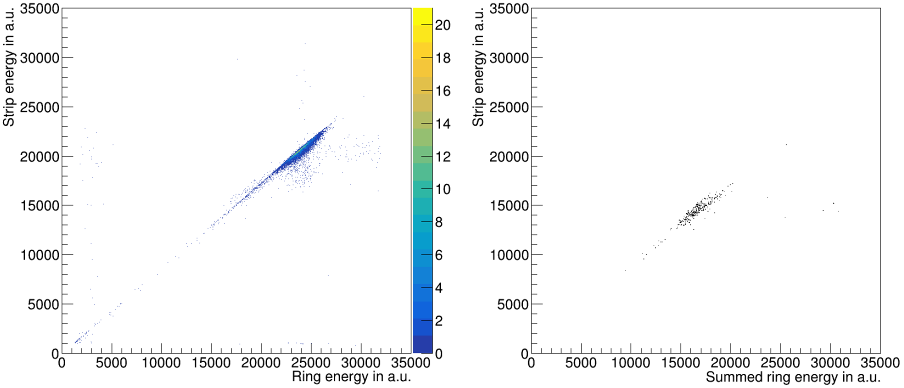

(a) Single hit on ring and outer strip.

(b) Double hit on ring, single hit on strip.

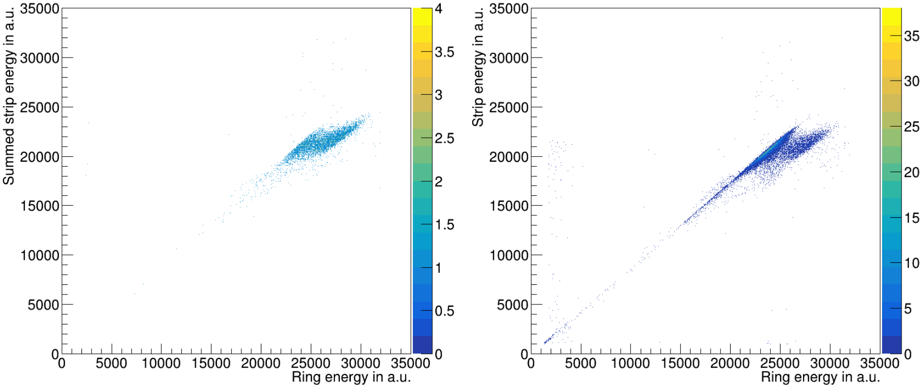

(c) Single hit on ring, double hit on strip.

(d) Single hit on ring and inner strip.

Figure 5.10.: Energy signals on DSSSD caused by single and double hits. Ring energies are summed for events where two rings fired. The same is true for double hits on strips. For more details see text, or Figure 5.9 for not summed energies. Double hits on both rings and strips are shown in Figure 5.11.

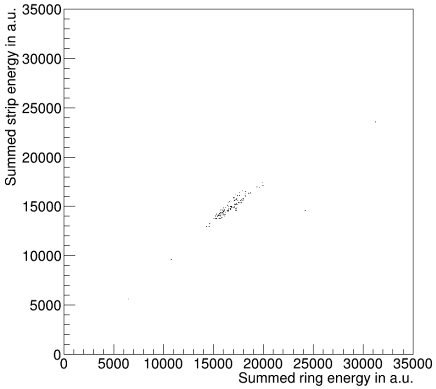

Figure 5.11.: Summed DSSSD energies for rings and strips, respectively. Double hits were detected for both rings and strips. Compare Figures 5.9 and 5.10.

Area (4) of Figure 5.9 shows the opposite effect: Charge sharing for hits which are detected by two strips and one ring. Figure 5.10c shows the same for the sum of both strip energies. The combined strip energy lies close to the respective single-ring single-strip hit event, which does make sense. The fact that the ring energy appears amplified is particularly notable. This is not straightforward to explain, and only possible explanations can be offered hereinafter.

The aforementioned pulse height defect [78], or rather its suppression may cause the observed behavior. Generally, a cloud of electron-hole pairs is created in the silicon detector upon impact of particles. For high-energy heavy ions this plasma starts to shield the trapped electrons and holes from the applied outer field of the detector. This results in a higher chance for recombination of the innerlying pairs. This effect happens systematically for heavy ions when they enter such a detector. Therefore, the only way to reliably calibrate this detector type would be to measure ions at various energies, in order to account for the strength of the defect. This was done, for example, for [63].

Imagine this effect taking place in the interstrip region of the backside of the detector. Here, the effect would also take place, but the electrons have a higher chance not to recombine, but to reach either of the two strips as the plasma is split. The holes would be pulled to the front rings, while the electrons interact with the p-stop area in the middle of the two strips and are thus reduced. This way the detectable gain of electrons on the back-side strips is counteracted by them being lost as the p-stop acts as sink for the electric field lines. The latter effect is evaluated in [80], though no explanation for the enhanced front-side energy is offered, as it is not seen there.

The strength of the pulse-height defect would be strongest for hits closest to the center of the inter-strip region, causing the clear curvature of the double-strip single-ring hit events, with the biggest gain in hole charge collection at about evenly split energies.

Another possible explanation is a baseline shift. This could be induced by the current of a neighboring strip, which would lead to an unphysical amplification of the detected voltage amplitute. Effects like this are seen in germanium detectors [82]. Such an effect depends on the energy splitting and may also cause the observed curvature. Lastly, the effect of mirror charges can also change the detection behavior of the double-sided silicon-strip detector [83].

As described in Section 4.2.1 the center 16 strips on the backside of each quadrant are electronically coupled into pairs. A consequence of this is that, for inner-lying strips, the effect of double hits on strips is already encoded in the read-out signal, as this signal is in fact the sum of two strip energies. In Figure 5.10d such a case is shown. The visible pennant originates from the same mechanism as the features of the distinguishable double hits on strips.

Another region not marked in Figure 5.9, but plotted in Figure 5.11, is the case of two neighboring strips and two neighboring rings being hit. Here, the summed energy is systematically lower than for the single-ring single-strip hits. This is intuitive as this is a superposition of the effects that were explained above.

Area (5) in Figure 5.9 shows the region that stems from an unresolved behavior of the MUX strip channel 15. This is visible for all quadrants, though the exact energy is a little different for each of them. The area was excluded from the final analysis.

On the innermost rings, the relative distribution of the four main event types is roughly 78 (3) % single-ring single-strip events, 1 (1) % double-ring single-strip events, 20 (3) % single-ring two-strip events and less than 0.2 % double-ring double-strip events. The likelihood of charge sharing between two rings or strips goes down with decreasing particle energy, i.e., most double-hit events occur in events in which the innermost rings fired. The comparatively low chance for holes to be detected on two rings simultaneously stems from their low velocity and the high field gradient in the interstrip region. The latter forces the holes predominately onto one ring instead of a split between two [79].

Note that the explained effects, with the exception of the MUX stip 15 behavior, are also seen in experiments utilizing the standard Coulex setup at ISOLDE, i.e., the forward facing DSSSD without MUX readout. Therefore, it is safe to assume that these features are not introduced by MUX behavior or the specific related read-out electronics but rather a property of the particle detector working with high-energy heavy nuclei.

After the correction of the time-dependent effects as discussed in the previous section, the four types of hits are considered separately. As mentioned above, single hits on ring and strip (type 0), good double hits on rings (i.e., hits where neighboring rings fired) with a single hit on strips (type 1), good double hits on strips with a single hit on a ring (type

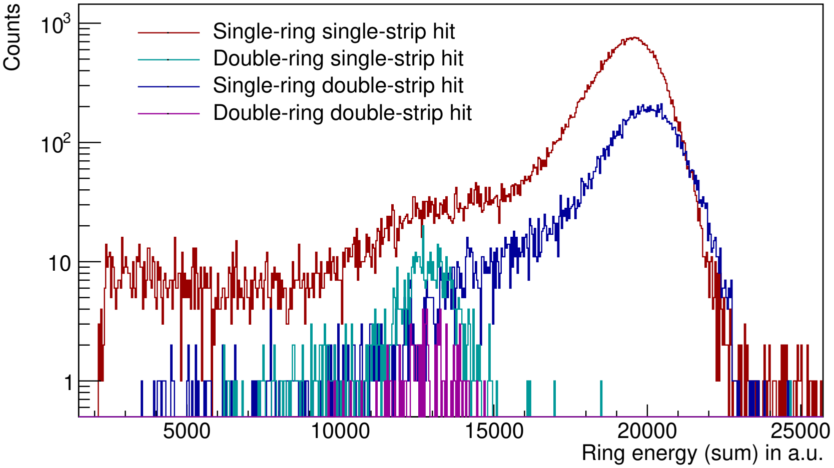

Figure 5.12.: Type-dependent uncorrected ring energies are shown for quadrant 1 and the innermost ring. Double hits on rings are summed up results. Note the offset dependent on type.

2), and good double hits on rings and strips (type 3) show different properties, which need to be addressed individually.

The idea of how to do this is sketched in the following: For each quadrant-ring-strip combination events of type 0 (single hits) are plotted as in Figure 5.10a, the slope of the shown diagonal is determined and subsequently altered to one by applying a factor to the ring energy. This factor is used for each ring energy regardless of the event type. Afterwards, dependent on their type, events far off the diagonal are handled, i.e., either corrected or discarded, so that in the end all good events lie exactly on the diagonal and show the same amplification. The last part is crucial for setting graphical cuts to distinguish beam and target particles later on. Figure 5.12 demonstrates the necessity of adjusting the amplification depending on type. Beam particles would be identified as target particles in the type 1 and 3 case, and vice versa for type 2 events.

All events have in common that the respective factors are determined using the sum of good double hits rather than considering each deposited energy individually. This is due to the fact that only the sum reflects an actual physical event.

For type 0 events, which are comprised of hits on the 8 outer strips, a shift perpendicular to the line onto the diagonal is performed, ring and strip energy are altered such that the

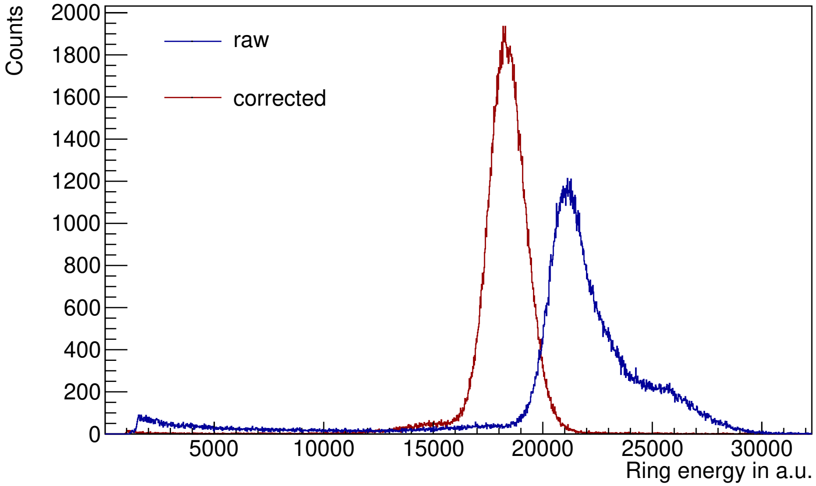

Figure 5.13.: Particle energy as detected by the innermost ring of the forward facing DSSSD particle detector quadrant 2. Raw data is depicted in blue. The low-energy counts stem from the malfunctioning mux channel 15 and are discarded in the correction. In red, the corrected particle energy is shown. Note that the exact location of the corrected peak is arbitrary.

amplification is correct. For events with hits on the 8 inner strips a shift parallel to the x axis is applied, which fixes the ring energy to the strip energy. For type 2 events the ring energy is also changed by a shift parallel to the x axis. Additionally a factor is applied, so that their energy is comparable to type 0 events. For type 1 and 3 events a perpendicular shift and an amplification factor are applied. All this is done by projecting the spectra onto the x and y axis depending on their hit type and an automatic fit to the data. Subsequently, the required parameters are stored in a settings file, which is later applied using a dedicated class.

The hits within the area resulting from the malfunctioning MUX channel 15 are excluded from the further analysis.

Figure 5.13 a shows the resulting projection of the innermost ring for quadrant 2 along with the uncorrected set. Note the absense of the energetically higher lying double peak structure for the corrected set.

To sum up, for the further analysis the exact origin of the energetic behavior of the

DSSSDs is not important as long as the effects are corrected. The corrected energies are used for the set kinematics cuts, i.e., the identification of whether a nucleus is a beam or target particle. This assignment is crucial for the Doppler correction of the observed γ rays.

The needed energy of the nuclei is calculated from the angular information. For double hits the mean of the two rings (or strips) is assigned as spatial information.

5.4. Calibration of the barrel silicon detectors

The main component of the calibration of the barrel detectors is the spatial calibration along the length of the strip. Note that two energy signals are provided by the detector. One from the 16-fold segmented front and one from the unsegmented backside.

The read-out happens on one side of the strip, and the detected hits feature larger energy signals when the hit occurs close to the readout side and smaller ones for hits further away. By comparing their frontside signal to the unsegmented backside, the interaction point along the strip can be determined.

As a first step, the noise peak caused by delta electrons on the low-energy side of the spectrum had to be identified and removed. This was done by automatically fitting a Gaussian to the data, and hereby determining a cut value. Subsequently, the spatial calibration had to be done by calculating the ratio between front and backside signal. This yields events in an interval of (0,x), where x is the maximum detected ratio as is visible by looking at the data for each strip individually. By applying a factor, this ratio was brought to the interval (0,1). The latter yields the position along the strip.

No α source was used in the calibration process, unlike in work [63], due to the fact that changes to the electronics settings had to be performed. In-beam data was used instead. This has the consequence, that the exact value of x had to be determined by hand, as an automatic fit to the low-statistics data was not possible.

The actual particle energy is calculated from the kinematics as done for the DSSSD detector using the formulae given in Appendix A.

The γ-ray energy spectrum that is obtained employing this calibration is shown in Figure 6.2b in Chapter 6.

5.5. Eventbuilding and background subtraction

In the scope of the eventbuilding process it is important to correlate γ ray and emitting particle using their respective time stamps. The time window is set to 1 µs for this step. This section deals with the principal idea and the background subtraction, while a detailed discussion of the timing properties and related corrections can be found in Section 5.7.

For the correlation of particles with their related γ rays the histogram shown in Figure 5.14 is needed. Two regions are marked. The prompt region (p) is set on the clear peak with a

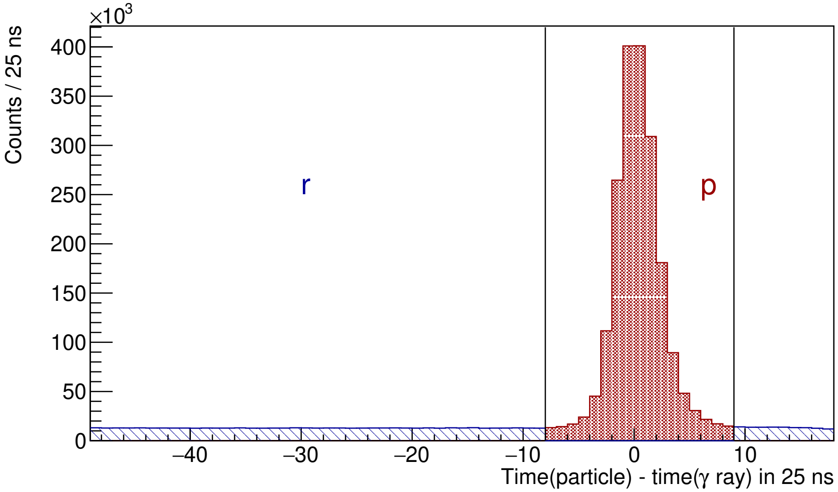

Figure 5.14.: Timing relation between particle and γ-ray hits. The prompt region is marked in red, while the random region used for the background subtraction is marked in blue.

time window of -200 ns to 225 ns, which encompasses all real particle γ-ray coincidences, i.e., events stemming from a Coulomb excitation and deexcitation process, on a continuous background. For a proper background subtraction the random region (r) with two time windows of -1225 ns to -200 ns and 225 ns to 450 ns, respectively, are used.

The events are sorted in such a way that every γ ray is assigned one or multiple particles of either the prompt or the random region: For example, there are events which are characterized by a γ ray correlated with a single prompt particle, denoted as (γ,p) events. Also higher multiplicities are possible, such as (γ,pr) events, that is, one γ ray with a particle hit in the prompt and one in the random timing window.

For the final γ-ray energy-spectra the events (γ,p), (γ,pp), (γ,pr), (γ,ppr) and (γ,prr) are considered as prompt, while (γ,r), (γ,rr) and (γ,rrr) type events are used for background subtraction. Of course, a factor accounting for the two distinct widths of the windows is applied during the actual subtraction. The use of mixed events, i.e., (γ,pr), (γ,ppr) and (γ,prr), as prompt events rather than omitting them, is based on their sensible looking Doppler-corrected γ-ray spectra, i.e., the dominant transitions are clearly visible, without any distinct additional background. Higher multiplicities and (γ,ppp) events are excluded from the further analysis. The thus omitted events amount to 0.5 % of the overall events.

Figure 5.15 shows the number of assigned particles per γ ray on a semi-logarithmic scale. By far the most γ rays are detected without any coincident particle, i.e., without a random or prompt particles, amounting to 89 % of the overall statistics. This means that 11 % of all recorded γ rays can be traced to the deexcitation of an identifiable nucleus which took part in the Coulomb excitation process. Only this portion is directly helpful in the determination of the structural properties of the nucleus being studied. This highlights the necessity of timestamps correlating hits stemming from the particle detector to those of the γ-ray detector.

Looking only at events which do have a particle assigned, that is all events except for the first column in Figure 5.15, most events are those either having only one related prompt or random particle followed by two related prompt or random particles. In fact, 50 % of the events are those with one assigned prompt particle, followed by 28 % with two related prompt particles (γ,pp). The ratio of (γ,p) to (γ,pp) events is governed by the kinematics of the reaction and the angular coverage of the particle detector. Only particles that are not stopped in the target can be detected by C-REX.

It is also instructive to consider the ratio of (γ,ppp) to (γ,p) events, which is 0.7 %, under the aspect of beam intensity. Naturally, a higher beam intensity is desirable as it yields higher statistics within a given time frame. With the mentioned ratio it is clear that from an analysis perspective no issues are expected if the intensity is increased.

5.6. Doppler correction

As the emission of γ rays happens in flight the energy of these γ rays appear at a shifted energy E_{detected} when they are detected. This so-called Doppler effect depends on the relative angle $\alpha_{\text{rel.}}$ between detector and direction of the emitting particle as well as on the velocity of the incoming beam v, denoted here as the ratio $\beta = \frac{v}{c}$, with c being the speed of light in vacuum. The energy of the emitted particle E_γ in its center-of-mass frame is then given by

$$E_\gamma = \frac{1}{\sqrt{1-\beta^2}} \cdot E_{\text{detected}} \cdot (1 - \beta \cos \alpha_{\text{rel.}}) \ . \tag{5.5}$$

While most spectra shown in this work are Doppler-corrected γ-ray energy spectra with respect to the projectile, ^{142}Xe, there is also a spectrum with respect to the ^{196}Pt target, that was used first during the campaign, depicted in Appendix B.

5.7. Timing characteristics

The energy and time information provided by each detector is routed through cables of distinct lengths and processed by several different modules depending on what detector type is considered, before being combined in the ADC channels. These particular paths

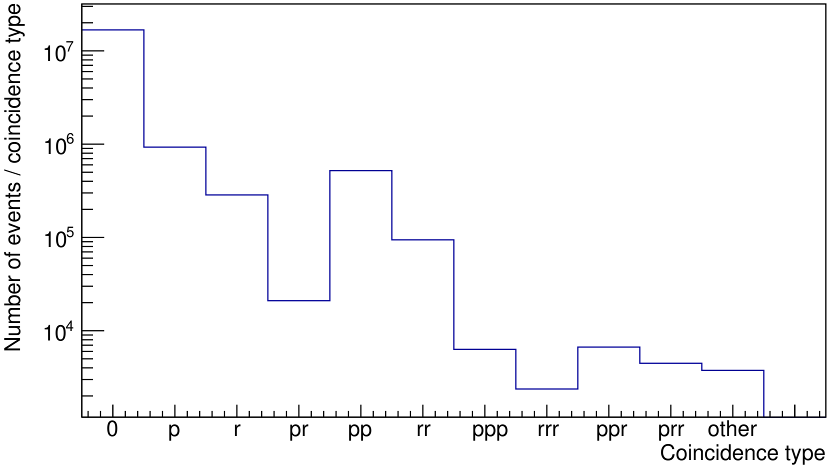

Figure 5.15.: Number of prompt (p) and random (r) hits accompanying γ rays in the "beam-on" window.

can cause specific delays for each of those groups, which need to be corrected and put in relation during the analysis. This is indispensable for the eventbuilding process described in Section 5.5.

This section covers the timing relation between MINIBALL and the particle detectors in Section 5.7.1 as well as the dependency of the MINIBALL timing signals on the energy of the detected γ-rays in Section 5.7.2.

5.7.1. Timing relation between MINIBALL and particle detectors

In order to determine the timing relation between the signals coming from MINIBALL and those from the particle detectors, the relevant information can be plotted as shown in Figure 5.16 in blue. The figure shows the time difference between a particle hit on one DSSSD quadrant and a γ-ray hit in MINIBALL with the constraint that the γ-ray energy exceeds 500 keV. The cause for this restriction will be discussed in Section 5.7.2. The peak reflects prompt events whereas the background is caused by random hits.

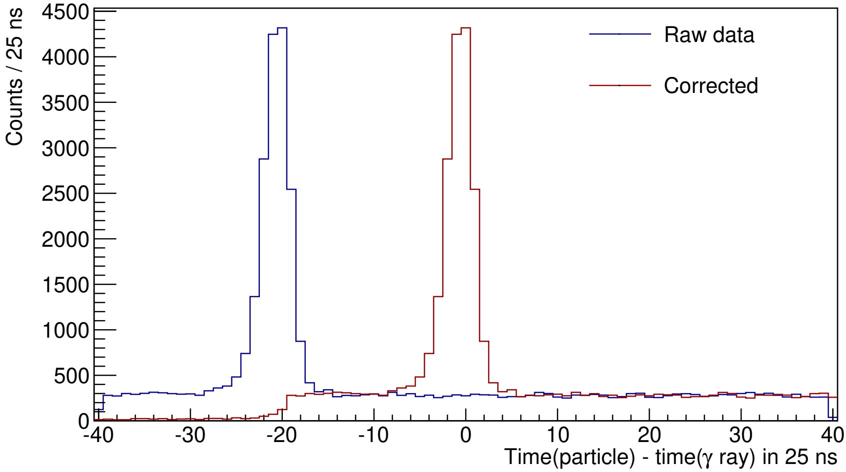

Figure 5.16.: Time difference between particle hit on quadrant 0 and a γ-ray hit in MINIBALL. Raw data is shown in blue while corrected data is shown in red.

This peak was then fitted with a Gaussian for each quadrant and detector type, i.e., barrel detector and the multiplexed DSSSD quadrants separately. Afterwards, a shift towards a difference of 0 was performed, which simplifies the analysis as the barrel and the CD detectors possess a distinct shift. The red line in Figure 5.16 shows the thus obtained corrected timing information exemplarily. Table 5.1 lists the obtained mean for each quadrant and detector before the correction was applied.

Note the differences between barrel and DSSSD signals. The offset mandates that the background window as described in Section 5.5 be set for each particle detector rather than for all detectors together.

Table 5.1.: Timing differences between MINIBALL and respective particle detector.

	Quadrant 0	Quadrant 1	Quadrant 2	Quadrant 3
CD detector	-517 ns	-514 ns	-492 ns	-515 ns
Barrel detector	-382 ns	-389 ns	28 ns	-383 ns

The origin of the extreme offset of the timing signal of one particular barrel detector with respect to the timing signals of the other detectors is not understood, but did not change the response of the detector. The statistics obtained from all detectors are comparable.

5.7.2. MINIBALL timing correction for low-energy γ-rays

On closer inspection, the timing pattern between MINIBALL and particle-detector array exhibits a γ-ray energy-dependent behavior. The left plot in Figure 5.17 depicts this curvature and the broadening of the distribution in the low γ-ray energy range. This is caused by the usage of a discriminator as part of the MINIBALL-readout electronics. This walk effect can be corrected by fitting a phenomenological exponential to the data

$$\mathcal{C} = p_0 + p_1 \cdot \exp\left(\frac{p_2}{\sqrt{E_\gamma}^3}\right), \tag{5.6}$$

where p_i are the fit parameters and E_γ the detected γ-ray energy and afterwards utilizing the correction factor $\mathcal{C}$ to remove the energy dependence for the further analysis. Figure 5.18 shows the fit function with the centroid of the timing data. To provide sufficient statistics for an automatic fit the γ-ray energies were summed for 40 keV bins.

The right plot in Figure 5.17 shows the corrected timing pattern.

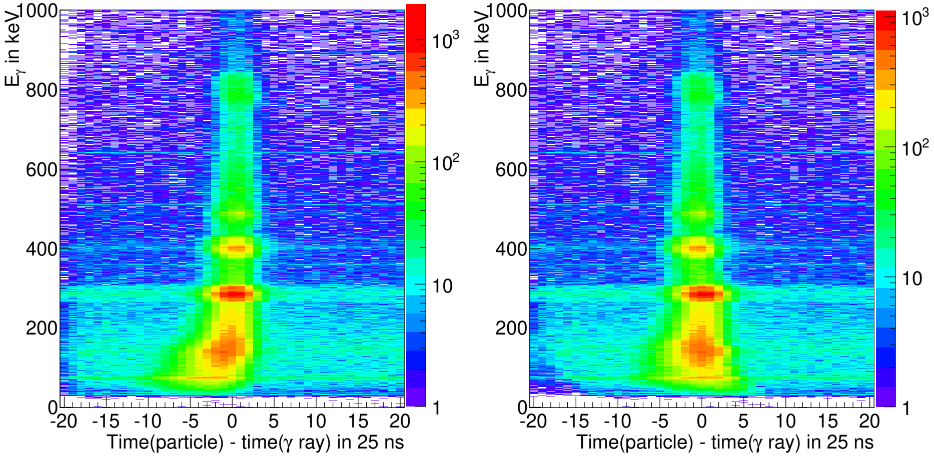

Figure 5.17.: Plot of the γ-ray energy dependence of the timing between MINIBALL and particle detector without correction on the left and corrected on the right.

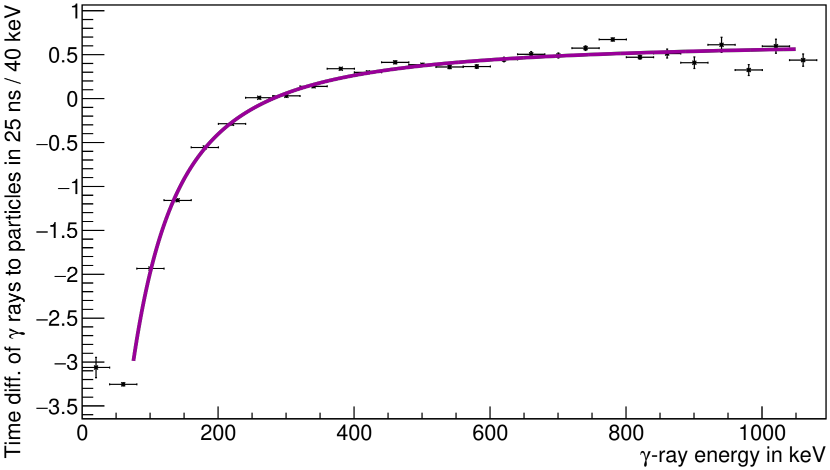

Figure 5.18.: Fit of Function 5.6 to the γ-ray energy-dependent timing offset between particle and γ-ray hit.

5.8. Identification of particles

In order to perform a valid Doppler correction of the detected γ-ray energies according to Equation 5.5, the spatial information on the emitting particle is needed. Particles and γ rays stemming from the same event can be determined using relative time stamps between γ ray and particles as discussed in Section 5.7.1.

During the event-building process, which is described in detail in Section 5.5, several prompt-region event types can be defined (Section 5.8.1), which need to be assigned and handled differently. In particular, a distinction needs to be made between beam and target nuclei as, ultimately, only the γ-ray energy spectrum which is Doppler corrected with respect to ^{142}Xe is used.

For this process, the silicon detector array and its so-called kinematics plot provides valuable information. Utilizing this plot, areas can be assigned wherein beam and target nuclei are expected to lie, as described in Section 5.8.2.

One special event type is the case in which exactly two particles are detected. This allows for a more selective procedure to determine good events and therefore yields a cleaner γ-ray energy-spectrum. See Section 5.8.3 for details. The fact that the full kinematical information is available in this case makes this event type a perfect tool for the determination of the distance between target and forward particle detector, see Section 5.10.1, as well as the beam shift, see Section 5.10.2.

5.8.1. Prompt-region event types

A detected particle in this experiment is expected to be either a target or a beam nucleus, which by definition scattered on their reaction partner, which is of the opposite type. While the target is ^{206}Pb, the beam particle is either ^{142}Xe or one of its daughters. The scattering kinematics is sufficiently similar for the possible reaction partners that in this section of this work, no distinction is made between xenon and its daughters.

In the following, only particles that are detected within the prompt time window, i.e., those that are referred to as prompt (p) particles in Section 5.5, are taken into account. Each single one of the detected particles can only be assigned to one of three types: Target, beam or unidentifiable. The exact determination process using the particle detector information is covered in the following section, and is not yet relevant.

While the particles are of a certain type, for the purposes of this section, an event is defined as the number of detected particles in the prompt region including their type. A maximum of two prompt particles can be part of such an event, as events with higher multiplicities are discarded as mentioned in Section 5.5. Therefore, three cases are possible for a single detected prompt particle: An unidentified particle, type 0, a beam nucleus, type 1, and a target nucleus, type 2. For two prompt nuclei six cases are possible: Two unidentified particles (00), an identified particle and one unidentified one, (01) or (02), two beam (11) or two target nuclei (22), or the optimal case of an identified target and an identified beam nucleus (12). Note that, for the purpose at hand, we do not need to differentiate depending on the order of the two nuclei, as it makes no difference in the analysis.

For unidentified particles, the event including their associated γ ray has to be discarded as there is no way to determine the correct Doppler-correction parameters. This is true no matter if a second particle is recorded within the prompt time window: The emitted γ ray may stem from either detected nucleus, and there is again no way to tell which one is the actual corresponding one.

In fact, the same is true for any event that comprises two kinematically non-matching nuclei. Therefore, only events containing either one identified nucleus or two matching nuclei are valuable for the further analysis.

5.8.2. Kinematics plot and cuts

The kinematics plot of the entire experiment is shown in Figure 5.19. This plot enables the determination of the nucleus type. The y axis showing the deposited energy of the particle is uncalibrated as beam-energy broadening in the target and the pulse-height defect for heavy nuclei [78] causes uncertainties that make an exact energy calibration pointless[2]. The x axis shows ϑ in the laboratory system under which the nucleus was scattered. The energy of the scattered particles can be extracted using the formulae given in Appendix A.

As can be seen in Figures 5.19 and 5.20, the beam and target regions overlap slightly, which is a consequence of using a target which at $4\,\frac{\mathrm{mg}}{\mathrm{cm}^2}$ is rather thick. As discussed in Section 4.1.4, the choice fell on this target due to the fact that the beam intensity was lower than anticipated. This causes a decrease of the selectivity of the particle type, i.e., whether a specific particle is a beam or a target nucleus.

Figure 5.20 shows the energy deposit in an inner ring of a single quadrant. There are two distinguishable regions, both fit with a Gaussian, which display an overlap, and an additional exponential background. For the target region the cut can be set such that only target nuclei lie within, while the same is not possible for beam particles. This does, of course, not increase the resolution of the peaks in the Doppler-corrected γ-ray energy spectrum as sometimes the correction may happen with respect to the wrongly identified particle.

In order to determine reliable cuts, i.e., defining the optimal area for both target and beam, each quadrant was handled individually. This is necessary as the kinematics is different for each of the quadrants due to the not-centered beam, see Section 5.10.2. The

---

[2] An extrapolation from the calibration of for example standard α-source energies would not be very precise, thus an energy calibration using beams at various higher energies is needed. This was done, for example, within the scope of the work [63].

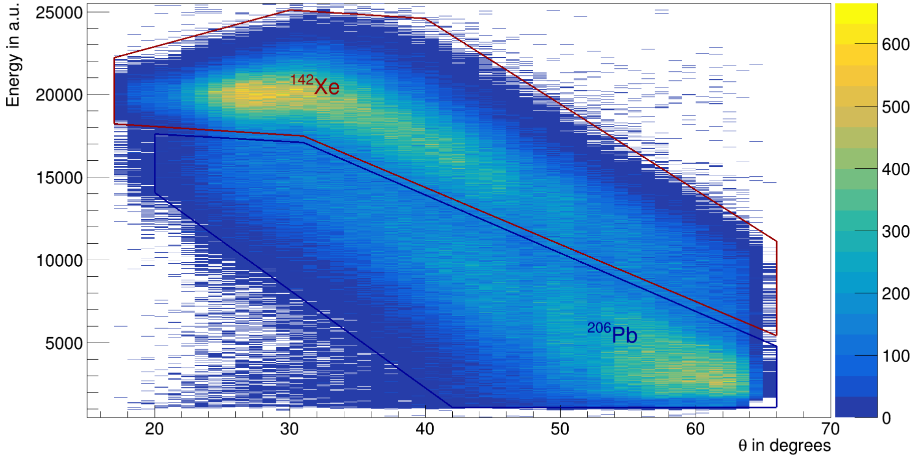

Figure 5.19.: Beam-shift corrected kinematics plot of the forward DSSSD. Beam region marked in red and target region marked in blue.

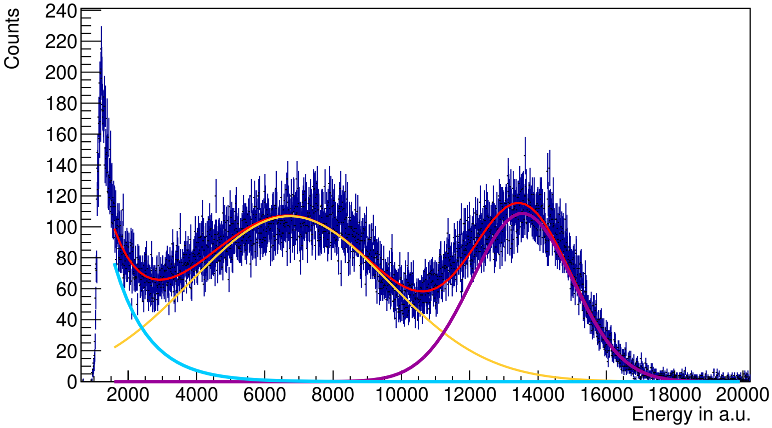

Figure 5.20.: Fit to an inner ring in a single quadrant, along with the respective fit functions comprised of two Gaussians and an exponential. Note that target and beam region overlap.

statistics of the two kinematically distinct sets as defined in Section 5.10.2 were treated separately, while within each set the statistics were summed.

The quadrants were subdivided using the separate rings and subsequently the aforementioned phenomenological function consisting of two Gaussians and an exponential background was fit to all of them.

5.8.3. pp event handling procedure

When only a single reaction partner is identified, the interpretation suffers from the ambiguity introduced by the overlap of beam and target region. This is not an issue if the full kinematical information is available, i.e., both beam and target nucleus are detected. The procedure to determine good pp events, that is two detected particles within the prompt window with respect to the considered γ-ray, is described in this section.

As part of the event-building process, the reaction partner of each detected particle is calculated and stored based on the equations found in Appendix A. This instance, based on the detected nucleus, is made up of various properties including the spatial information of the detected particle and its β, along with possible corrections (such as the beam shift discussed in Section 5.10.2) and the information of the recalculated reaction partner.

This comes in handy when determining whether two simultaneously detected particles stem from the same reaction: Consider a particle $P0$, which, identified via the cuts discussed in the previous Section 5.8.2, is a beam nucleus. The recalculated reaction partner must then be a target nucleus. Now, the angular information ($\vartheta_{\mathrm{P1,det.}}$,$\varphi_{\mathrm{P1,det.}}$) of the second particle $P1$ can be compared to the reconstructed set ($\vartheta_{\mathrm{P0,rec.}}$,$\varphi_{\mathrm{P0,rec.}}$). Figure 5.21 shows the angular differences between such partner sets. Figure 5.21a focusses on the accepted-difference cut in ϑ, while in Figure 5.21b the same situation for φ is highlighted. The accepted-difference cuts are 7.5 ° and 30 °, for ϑ and φ, respectively.

Thus, if two particles are identified as reaction partners, they are included as a good event in the analysis. Otherwise, the inverse situation is tested. That is, particle $P0$ was in fact a target particle and $P1$ a beam particle. This may mean that further calculations are necessary as now the information on the reconstructed partner can not be used. Should this too fail to yield a good result, the event is discarded as it is unusable.

Figure 5.22 shows the identified pp-event types using only the angular cuts discussed in Section 5.8.2 in blue and the hits after applying the procedure described here in red. The result was also tested by checking the corresponding Doppler-corrected γ-ray energy-spectra. Using this procedure the number of usable pp events was increased by 10 %.

5.9. Determination of the velocity of emitting particles

In order to Doppler correct the γ-ray energy correctly, it is essential to have a good estimate of the velocity of the emitting particle.

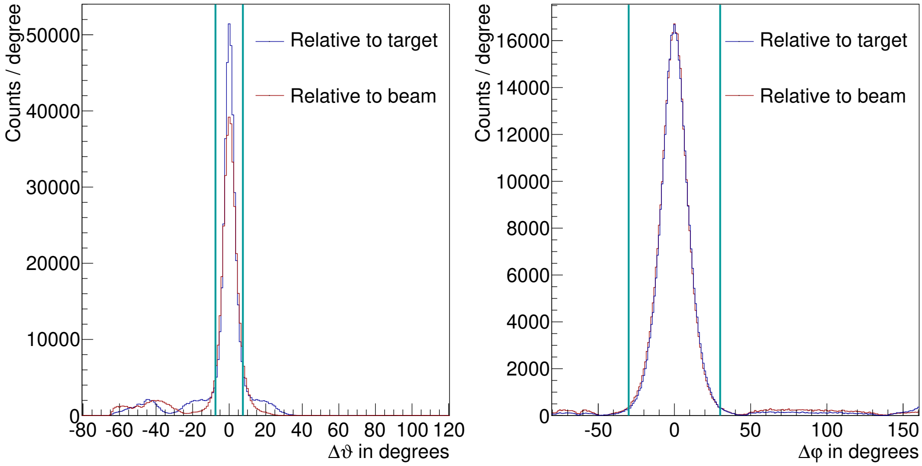

(a) Differences for ϑ.

(b) Differences for φ.

Figure 5.21.: Angular differences for pp events including the set cuts. Reconstructed and detected angles are subtracted for detected beam and target, respectively.

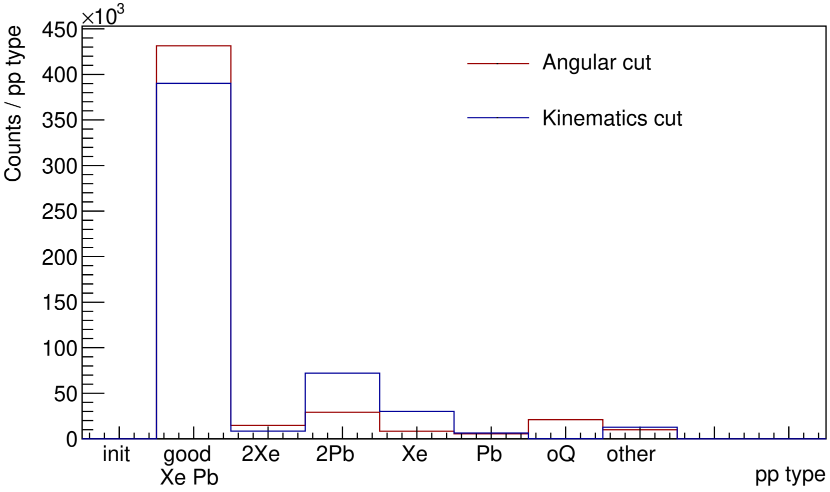

Figure 5.22.: Identified pp event types, using only kinematics cuts in blue and using angular cuts as described in text in red. Only events with precisely two nuclei detected within the prompt timing window as shown in Figure 5.14 are plotted here. The number of counts per bin stand for (from left to right): A good pp event with kinematically matching xenon and lead nucleus detected, two xenon nuclei detected, two lead nuclei detected, one xenon nucleus and one unidentified particle, one lead nucleus and an unidentified particle, two unidentified particles on opposite quadrants, and the last one shows all other events.

Several factors influence the velocity of a nucleus: Firstly, of course, the energy of the incoming beam together with the kinematics of the Coulomb excitation process, which are covered in Chapter 3. Secondly, the energy loss of the nucleus passing through the target, see Section 5.9.1, which may be angle dependent.

Figure 5.23 shows the calculated velocity $\beta = \frac{v}{c}$ of the particles after the Coulomb excitation process per angular bin in colors. Here, each bin is understood as a range with a $20\,^\circ$ width in $\vartheta_{\mathrm{lab.}}$. The black part shows the loss in velocity after the excitation process due to the interaction with the target material. Note that dependent on the scattering angle the particle moves through a distinct target width.

The formulae used for the calculation are given in Appendix A.

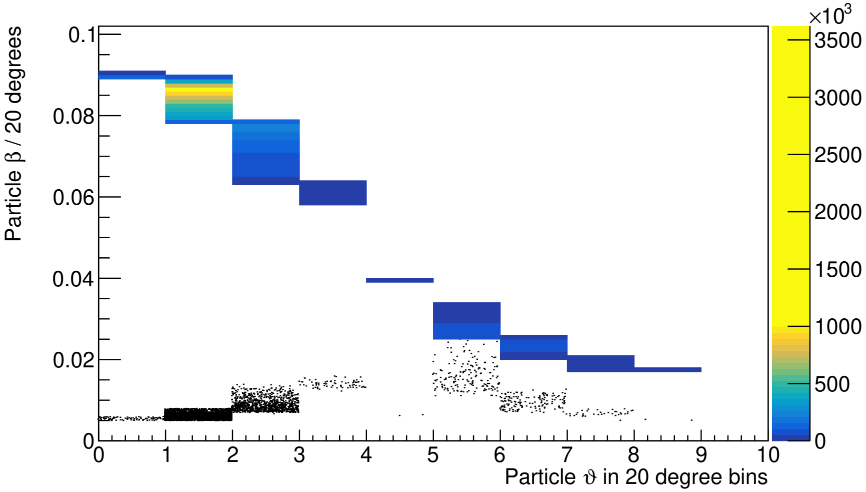

Figure 5.23.: The colored part shows the velocity β of the particles after the Coulomb excitation process in units of the speed of light. The x axis is to be understood as angular bins that are to be multiplied by $20\,^\circ$. The black part of the graphics shows the loss in velocity while traveling through the target after the excitation process.

5.9.1. Stopping powers

The reduction in velocity due to interaction with the medium can be calculated using stopping powers. Two different kinds of interactions play a role [84]: Stopping due to

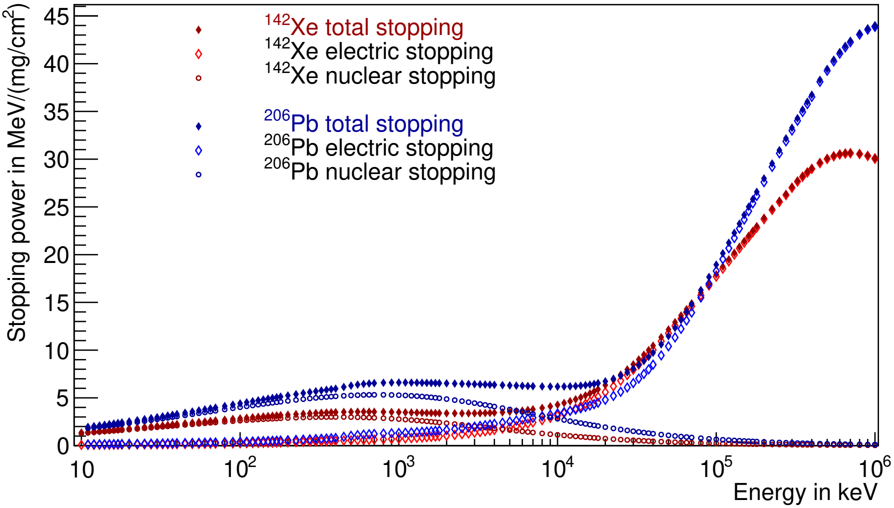

Figure 5.24.: Total stopping power of ^{142}Xe in ^{206}Pb dependent on the particle energy shown in red. The total stopping power of ^{206}Pb in ^{206}Pb is shown in blue. Respective nuclear and electronic stopping are shown for both cases as well. Calculated with SRIM [85].

nuclear interaction, i.e., stopping as a result of interacting with the positive nucleus, which is most important in the region below 10 MeV. Above that, electronic stopping, i.e., the interaction with the electrons around the nucleus, becomes most important. The two interactions are shown separately in Figure 5.24.

For our experiment, the reduction of kinetic energy before the Coulex interaction point, which is set to be in the middle of the target, is particularily important. Additionally, the angle-dependent energy-loss after the interaction point is needed. The latter is dependent on the particle in consideration, i.e., either ^{142}Xe or ^{206}Pb. Figure 5.24 shows the applied stopping powers, calculated with SRIM [85].

The data shown is fitted for both relevant nuclei employing the function

$$\frac{dE}{dx} = \left(\frac{dE}{dx}\right)_{\text{el.}} + \left(\frac{dE}{dx}\right)_{\text{nucl.}} \tag{5.7}$$

$$= \exp\left(p_0 + p_1 \cdot \log(E) + p_2 \cdot \log(E)^2\right) \tag{5.8}$$

$$+ \exp\left(p_3 + p_4 \cdot \log(E) + p_5 \cdot \log(E)^2\right), \tag{5.9}$$

where p_i are the fit parameters and E the corresponding energy. The resulting function is used for the energy-loss calculation, and therefore the Doppler correction of the γ-ray energies. The stopping powers are also needed as input for GOSIA.

5.10. Determination of the position of the detectors

Precise knowledge of the positions of both, particle and γ-ray detector, is as vital for the Doppler correction itself, see Equation 5.5, as it is for the subsequent analysis using GOSIA, see Chapter 7. Therefore, this section gives an overview on the determination of the position of both detector systems.

A feature of C-REX is the changeability of the distance between FCD and target. This requires that this piece of information is determined using the experimental data, which is discussed in Section 5.10.1. Furthermore, a possible beam shift, i.e., an offset of the beam center to the center of the C-REX, needs to be accounted for and is examined in Section 5.10.2. Lastly, an in-depth discussion of the determination of the MINIBALL-crystal position can be found in Section 5.10.3.

5.10.1. Determination of the distance between forward DSSSD and target

The forward DSSSD is movable along the beam direction. In our case, it was practical to put this particle detector as close to the target as mechanically achievable, to gain the highest angular coverage possible, knowing that the most forward angles have a lower information value for multiple-step Coulomb excitation. Additionally, this avoids a high rate of elastically scattered particles, which are scattered predominantely in extreme forward angles (Rutherford), therefore reducing radiation damage to the silicon detector.

If the distance is not well known, the missing information warps the angular data extracted from the silicon detector, having consequences for both Doppler correction and GOSIA analysis.

To correct this, a set of events was used for which the full kinematical information is available: Events for which both, recoiling target t and scattered beam particle b, are detected, see Section 5.8.3. In the center-of-mass frame

$$\vartheta_{\mathrm{b,cm}} + \vartheta_{\mathrm{t,cm}} = 180^{\circ} \ , \tag{5.10}$$

with $\vartheta_{\mathrm{b,cm}}$ and $\vartheta_{\mathrm{t,cm}}$ being the respective polar angles belonging to the detected particles, holds.

With this knowledge the assumed distance can be varied and the impact on the thus calculated kinematics can be studied.

Figure 5.25 shows the effect that varying the separation length has on the summed center-of-mass ϑ angle. Deviating from the 20 mm distance used, a clear offset of the expected 180° occurs.

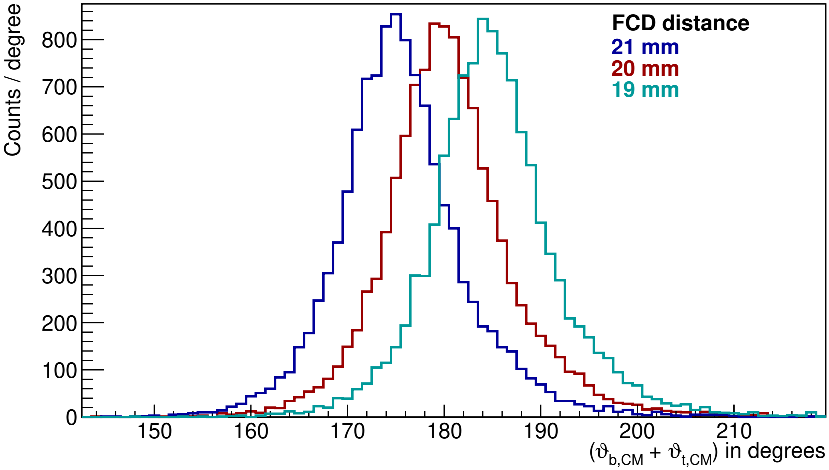

Figure 5.25.: Sum of ϑ in the center-of-mass frame for three distinct distances.

5.10.2. Correction of beam shift

Unlike the other two spatial corrections discussed in the current section, the exact beam position is not only dependent on the experimental set-up, but also on the changes and instabilities of HIE-ISOLDE's post accelerator. In fact, in order to improve the intensity of the beam, several changes to the accelerator settings were made over the course of the experimental campaign. These are reflected in a time-dependent shift of the beam position.

Such a beam shift not only affects the Doppler correction by moving the detected angles of γ rays and particles, but also causes some of the energy effects discussed in Section 5.3.3. For the correction, again, the set of events for which the full kinematical information is available was used.

The idea is to exploit a similar fact as in Section 5.10.1, namely,

$$\varphi_{\mathrm{b,lab}} + \varphi_{\mathrm{t,lab}} = \varphi_{\mathrm{b,cm}} + \varphi_{\mathrm{t,cm}} = 180^\circ \ . \tag{5.11}$$

Here, φ are the respective azimuthal angles of the detected beam-like (b) or target-like particles (t) in the laboratory frame (lab) and center-of-mass frame (cm).

Figure 5.26 shows the connecting line between two simultaneously detected particles. Using the 180° argument, the supposed real beam center can be varied and the distance d connecting the closest point on the aforementioned line to the assumed beam center is calculated. Each event with two coincident particles serves as one data point for the analysis.

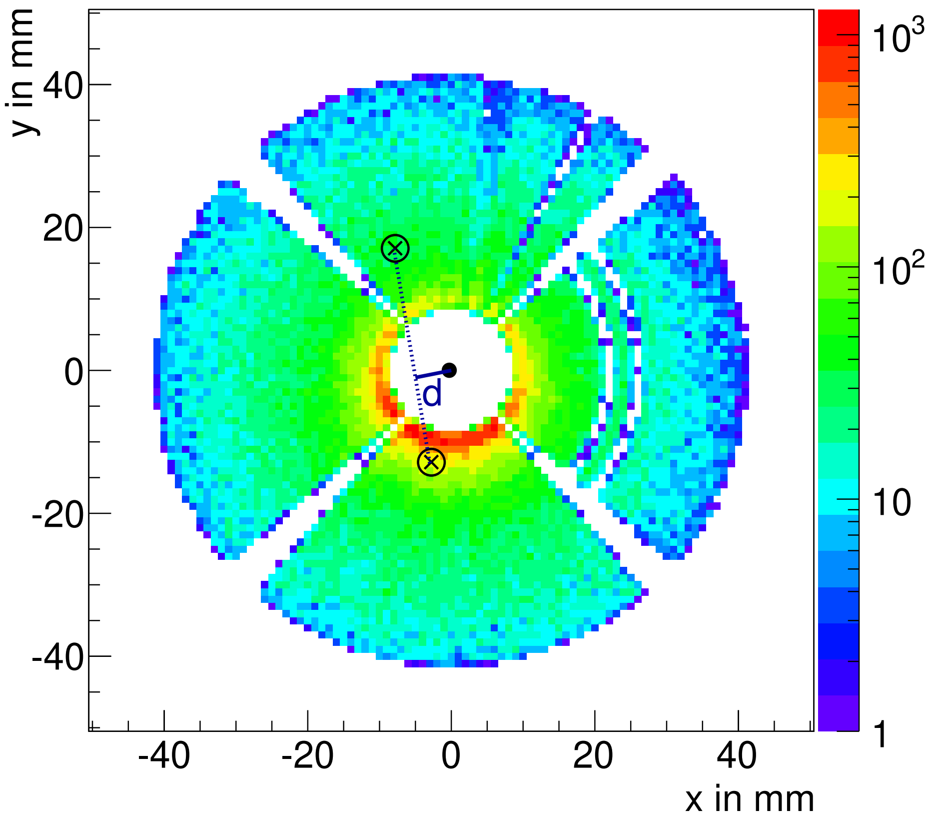

Figure 5.26.: Hit pattern on forward-facing DSSSD particle detector of a single run, without any beam-shift correction applied. Malfunctioning rings and strips are clearly visible. An event with two particles is sketched. The connecting line is marked along with the distance d as used in Equation 5.12. For more information see text.

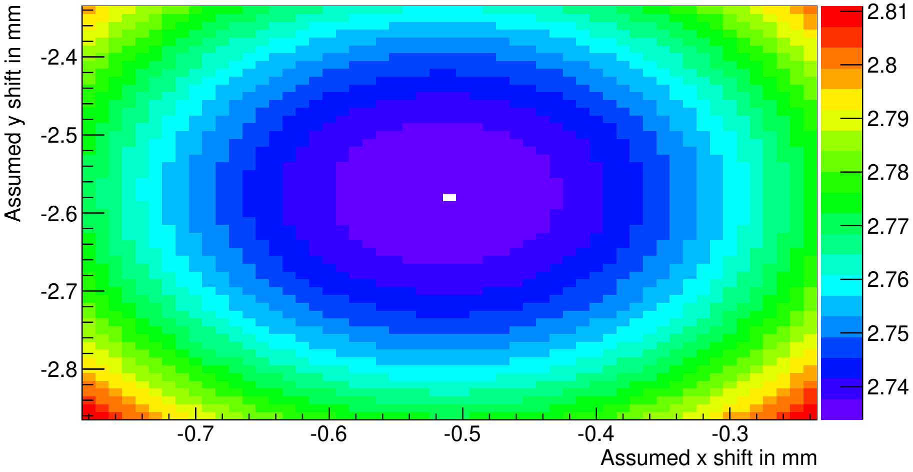

Figure 5.27.: Exemplary plotted figure of merit as function of supposed real beam position for one run.

The figure of merit (FOM) is then defined as

$$FOM = \Sigma d^2 \,. \tag{5.12}$$

Varying the assumed center and calculating the FOM for each case yields a clear minimum as is visible in Figure 5.27. This was done for each run separately so that the time-dependent shift could be determined [3]. Figure 5.28 shows the thus determined shifts including their 1 σ uncertainties. Using this argument, the entire experimental data set can be split into two, which are kinematically different, while within one set the kinematical differences can be considered negligible. The first set has its center at an offset of -0.6 mm in x and an offset of -2.6 mm in y. For the second set the offset is 0.3 mm and -0.8 mm, for the x and y direction, respectively.

This is the reason why the run-dependent correction of the energy effects of the DSSSDs is handled as described in Section 5.3.3.

Furthermore, the angles of the detected particles were corrected using these determined shifts for each run separately.

The clear change between the two sets happened due to an intervention of the ISOLDE team, during which they tried to improve beam current and alignment via changes of ISOLDE's post-accelerator.

---

[3] The advantage of this approach is the independence of the method from, e.g., MUX behavior and set thresholds. A method based on Rutherford cross section arguments has a stronger dependence on these.

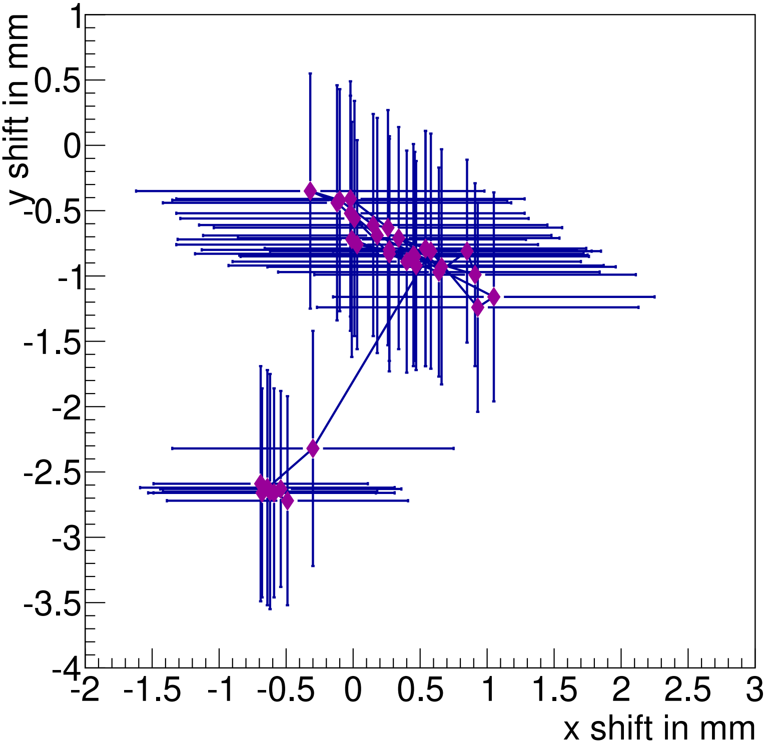

Figure 5.28.: Determined beam position for each run including their 1 σ uncertainties. The lines in between the points connect consecutive runs.

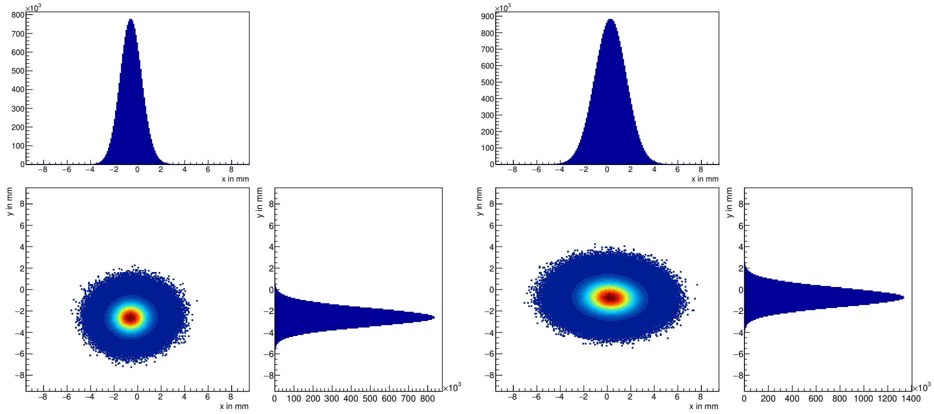

(a) First part of the campaign.

(b) Second part of the campaign.

Figure 5.29.: Beam position and accumulated intensity in a.u. during the campaign. In between the two sets changes to HIE-ISOLDE's post accelerator were performed by the ISOLDE operators. Note that the beam is not centered for the entire campaign.

Figure 5.29a shows the accumulated beam-spot intensity in the first part of the campaign. This was calculated assuming a Gaussian in x and y direction using the estimated $1\,\sigma$ uncertainties as shown in Figure 5.28. Figure 5.29b depicts the same for the second set.

5.10.3. Determination of position of MINIBALL crystals

The determination of the position the MINIBALL segments was done by considering the Doppler correction of each MINIBALL segment separately. This was possible as the $2_1^+ \to 0_{\text{g.s.}}^+$ transition has sufficient statistics for this approach. An additional assumption is that by determining the position that yields an optimal Doppler correction for this specific transition, γ rays with different energies are Doppler-corrected sufficiently as well.

When considering only spatial information the Doppler correction is only dependent on the relative angle between emitting particle and its γ ray. (See Section 5.6 and specifically Equation 5.5 for more information.) That means that if the particle detector is already fixed, the only spatial information needed from the γ-ray detector is the polar angle ϑ and the azimuthal angle φ.

In order to determine these, a Doppler correction created from all possible pairings of ϑ and φ is performed. The allowed values for φ are limited to integers, while ϑ is subdivided in 0.5 ° steps. For each of the (ϑ, φ) pairs a γ-ray energy-spectrum is created for each MINIBALL segment separately. For each of these spectra a fit to the $2_1^+ \to 0_{\text{g.s.}}^+$ transition is performed. The quality of the fit is then written into an array corresponding to the pairs of φ and ϑ. Using this array the optimal angles for each segment are determined. The crucial part is to define a measure of the quality of the fit. The figure of merit (FOM) used is introduced in the following section.

Further improvements are discussed in Section 5.10.3.

Figure of merit

Choosing a Gaussian

$$G(x) = \frac{1}{\sqrt{2\pi\sigma^2}} \cdot \exp\left\{\left(-\frac{(x-\mu)^2}{2\sigma^2}\right\}\right) \tag{5.13}$$

as fit function, two fit parameters play an important role in the decision whether a Doppler correction is performed well: The standard deviation σ and the center of the peak μ, or rather the distance of the center to the nominal value as given in literature [86]. The latter is more important for this case as the spectra of all crystals need to be added up eventually. So if each of these peaks lies at a slightly different position the standard deviation of the summed peak will be significantly increased. Therefore a weighting factor of 10 is chosen to increase the impact of the mean value on the figure of merit FOM. The FOM is defined as

$$FOM = \sqrt{\sigma^2 + 10 \cdot |287.2\,\mathrm{keV} - \mu|^2}\ , \tag{5.14}$$

where $287.2\,\mathrm{keV}$ is the γ-ray energy stemming from the aforementioned $2_1^+ \to 0_{\text{g.s.}}^+$ transition.

Figure 5.30 shows a plot of the FOM for one MINIBALL segment. The optimal angle combination of this segment is easily determined.

Consideration of higher-lying transitions

Another property of the nucleus is relevant for the determination of the MINIBALL angles using Coulomb excitation data: The lifetime of the initial state of the transition. An excited nucleus first moves a certain lifetime-dependent distance before decaying into the final state. This means that higher-lying states must have decayed before then. Furthermore, the velocity vector of the nucleus has a slightly different angle relative to the MINIBALL segment.

The lifetime of the first 2^+ state is 249 ps [87]. This corresponds to a distance of roughly 4 mm, after which half of the states are depopulated assuming a mean β of 0.08 c, see Figure 5.23. Hence, on average, all transitions other than the $2_1^+ \to 0_{\text{g.s.}}^+$ transition happen 4 mm before the one used as measure to determine the position of the MINIBALL segments.

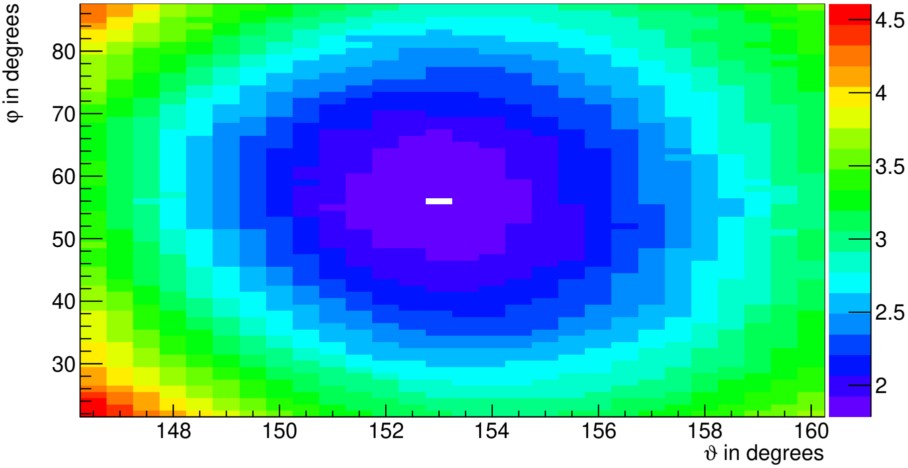

Figure 5.30.: Part of the plot of the FOM as defined in Equation 5.14 dependent on ϑ and φ of an exemplary MINIBALL segment. Centered on the optimal MINIBALL angles.

This is clearly not the optimal case. Considering instead the second strongest transition, i.e., the transition $4_1^+ \rightarrow 2_1^+$ at 404 keV, which has a lifetime corresponding to a travel distance below 1 mm, may have its merits. This transition takes place at roughly the same point as the other higher-lying transitions. Unfortunately, the statistics for this transition is a lot lower, especially on segment level. This results in a flatter minimum for the angle set, and increasing uncertainties for the respective angles.

Nevertheless, the optimal angles were fitted in the same manner as described for the $2_1^+ \rightarrow 0_{\mathrm{g.s.}}^+$ transition. The ϑ positions of the MINIBALL segments are systematically lower than the ones obtained from the analysis of the ground-state transition. There is no systematic change in φ. Both these observations make sense: ϑ must be lower when the emission of the γ ray takes place closer to the target. Simultaneously, φ will not show such a regular change as the particle detector is almost symmetric with respect to the beam direction. (Deviations from that symmetry are caused by malfunctioning strips on the detector, and are rather minor.) Consider for the last part a MINIBALL crystal located upstream, and on the top-right side of the DSSSD. On the one hand, a particle can be detected on the left part of the DSSSD, in which case the φ emission angle is smaller for 404 keV γ rays than for 287 keV γ rays. On the other hand, a particle can hit the right side of the DSSSD, generating a bigger φ emission angle for 404 keV γ rays than for 287 keV

γ rays. This is to say that deviations $\Delta\varphi$ are averaged out as for each hit on the particle detector a “mirror”-partner hit can be found as the setup is symmetric.

Due to the lower statistics, the average deviation $\Delta\vartheta = -1.5\,^\circ$ is used to correct all MINIBALL angles, while φ remains untouched.

For a cross check of the plausibility of this value also the distances d between the respective MINIBALL crystals and target given in reference [77] can be used: Consider a triangle formed by the side d (the aforementioned distance d), the adjacent angle $\Delta\vartheta = 1.5\,^\circ$ and the opposite angle $\beta = 180\,^\circ - \vartheta$. The short side s of this triangle can then be calculated using $s = \frac{\sin{(\Delta\vartheta)}}{\sin\beta} \cdot d$, yielding 5 (2) mm. This is consistent with the 4 mm determined by considering the lifetime of the first 2^+ state.

Furthermore, the γ-ray interaction depth in a germanium crystal depends on the γ-ray energy. As a result, the interaction point of an 287 keV γ ray and an 404 keV γ ray already differs by several millimeters, and increases further when considering higher-lying transitions. This is calculated employing the idea of an equivalent point-like detector according to [88]. This energy dependence adds to the uncertainty when comparing the values given in [77] to the determined $\Delta\vartheta = -1.5\,^\circ$ offset.

The final validity check, if the assumption of subtracting 1.5 ° from all ϑ is correct, is given by the Doppler-corrected γ-ray spectra. There is a systematic improvement of the resolution of the visible peaks, but they lie within the uncertainties. The literature peak positions are better met for all known transitions, except for the $2_1^+ \rightarrow 0_{\text{g.s.}}^+$ transition, which shows a shift by 0.5 keV towards lower energies. This is neither surprising, nor an issue for the further analysis. The accuracy of the energies of the new transitions is more important as they are determined for the first time.

6. Spectroscopy

Before this experimental campaign only the main band along with some higher-lying states were known.

Most data stems from fission experiments, e.g., neutron-induced prompt fission of ^{235}U and ^{241}Pu [87], and spontaneous fission of ^{252}Cf [89] and ^{248}Cm [90, 9]. A feature of spectroscopy of fission fragments is the population of high-energy high-spin levels, which subsequently deexcite and decay via lower-lying levels towards the ground state of the nucleus. The method gives access to high-lying non-yrast band members, at least if a band is populated at all, but not the low-lying non-yrast states, as the γ-ray decay predominantly happens via the main band. The latter is due to the fact that E1 transitions are possible from the side bands with negative-parity states to the yrast band with positive-parity states. E1 transitions have a higher transition probability than E2 transitions within the same band.

An earlier Coulomb excitation campaign at ISOLDE confirmed the location of the first 2^+ and first 4^+ state in ^{142}Xe [10]. The advantage of Coulex experiments is the population from the ground state up the level scheme, as the intensity of the measured γ-rays provides definite knowledge on the order of the states, at least for the main band.

Furthermore, a report on a β-decay study of ^{142}I populating ^{142}Xe is available [91], though it does not comprise a level scheme, which is under construction [92]. From systematics, the authors assume the odd-odd parent ^{142}I to have a ground state of $I^\pi = 2^-$, indicating that only the low-spin states, i.e., states for which $1 \leq I \leq 3$ applies, in the daughter ^{142}Xe can be populated [92].

So, in principle, the complementary nature of these experimental methods yields complete access to the states of a nucleus, such that a consistent picture of the level scheme forms. Unfortunately, for ^{142}Xe the level scheme is far from complete.

Figure 6.1 shows the low-energy level scheme published in literature. Note that for the octupole band, the spin and parity assignment for the two lowest-lying states is missing. These could be the 3^- and 5^- states, which were put at their respective energies based on coincidence and systematics arguments by Urban et al. [9]. Furthermore, the 1^- state is missing altogether and no other low-lying states and transitions have been published so far.

In Figure 6.2 several γ-ray energy-spectra, which are Doppler corrected with respect to ^{142}Xe, are shown. While the main band is well visible up to the 8_1^+ state, discussed in detail in Section 6.2, additional new features are visible. The spectra already show all the assignments discussed within the scope of this chapter. Note that Figure 6.2a shows events

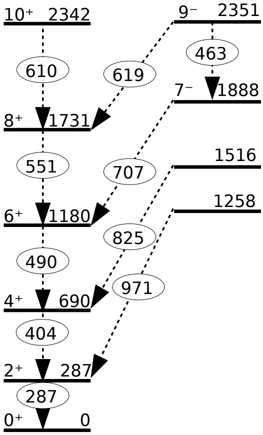

Figure 6.1.: Partial level scheme of ^{142}Xe as found in [9]. For higher-lying states see also [90].

for which the full kinematic information is available, i.e., one xenon nucleus and one lead nucleus with matching kinematics were identified. This yields the cleanest spectra.

The two other spectra show events for which the scattered beam nucleus is detected in extreme backwards angles, once for xenon hits on the barrel in Figure 6.2b, and for xenon hits on the BCD in Figure 6.2c. This highlights the enhancement of multiple Coulomb excitation with increasing scattering angle, e.g., note the development of the ratio $\frac{\mathrm{Y}(8_1^+\rightarrow 6_1^+)}{\mathrm{Y}(2_1^+\rightarrow 0_{\mathrm{g.s.}}^+)}$, especially as the first two spectra are shown on a semi-logarithmic scale, while the last one is linear for both axes.

Besides the clearly visible main band up to the 8_1^+ state, there are hints of the 3^- state at the energy proposed in [9], see Section 6.4.

Additionally, comparatively strong transitions are visible that are interpreted as stemming from a γ band. These transitions have not been reported previously. Their spectra are examined in Section 6.3, including the influence of the smeared target transition on the determinability of the counts in the new transitions.

At the low energy side, the X rays stemming from the lead target are visible at the expected energies at 73 keV, 75 keV and 85 keV [93]. They appear broader as one combined peak as the spectra are Doppler corrected assuming all γ rays stem from the deexcitation of ^{142}Xe. The X rays originate from events where an electron is removed from the atomic K shell. This vacancy is subsequently filled by an electron from the L shell under emission of electromagnetic, so-called K_α radiation, or the M shell emitting K_β radiation. The thus

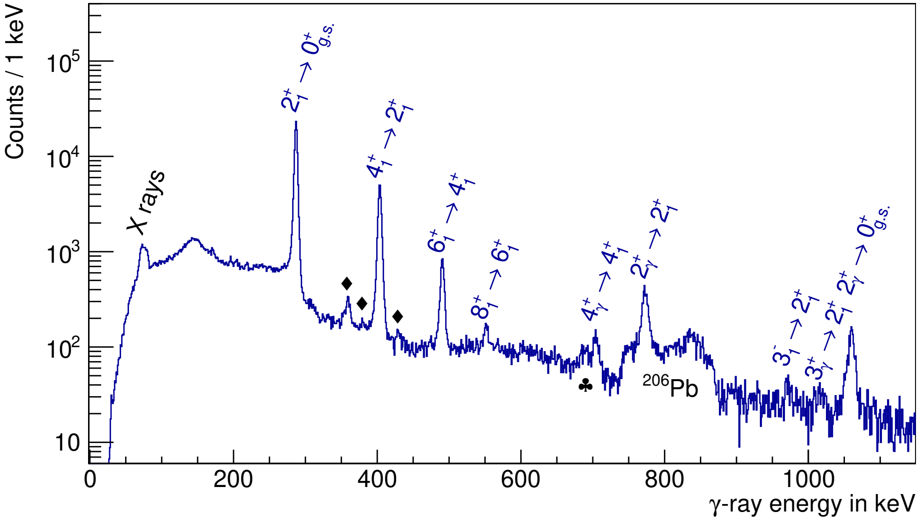

(a) Doppler-corrected γ-ray spectrum for full kinematics (pp) events.

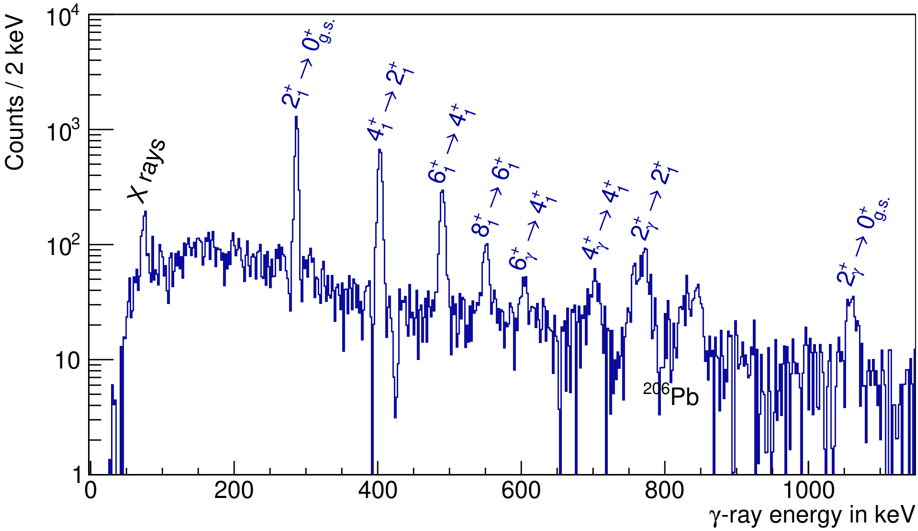

(b) Doppler-corrected γ-ray spectrum for detected ^{142}Xe on barrel.

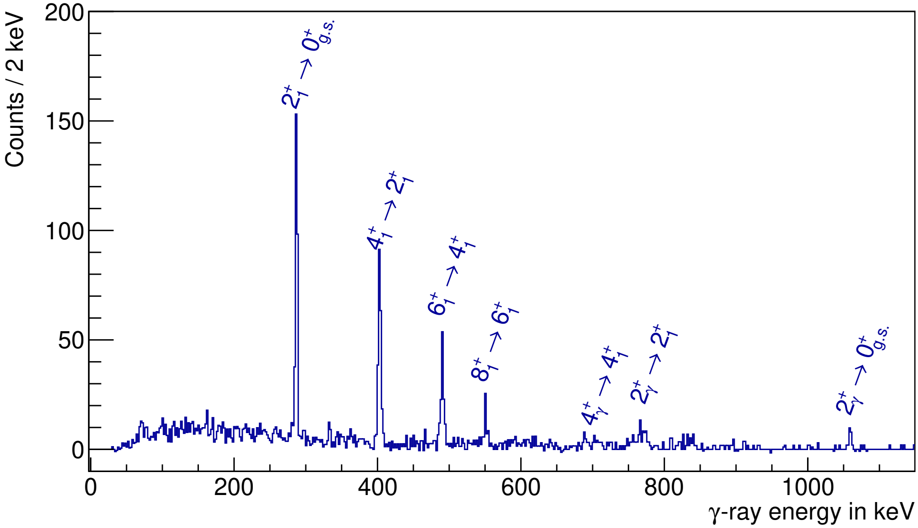

(c) Doppler-corrected γ-ray spectrum for detected ^{142}Xe on BCD.

Figure 6.2.: Doppler-corrected γ-ray energy-spectra. Doppler corrected with respect to xenon. Efficiency calibrated and background subtracted. ^{142}Xe transitions are denoted including the corresponding states. Dominant daughter transitions are labeled with a diamond, while the pile-up transition at 691 keV is marked with a club. The target transition is smeared due to being wrongly corrected. For more information see text.

created radiation is referred to as characteristic X rays.

The $2_1^+ \rightarrow 0_{\mathrm{g.s.}}^+$ transition of the ^{206}Pb target is visible at 803 keV. It appears broad in this spectrum for the same reason as the X rays.

Furthermore, signs of the excitation of the daughter nuclei ^{142}Cs and ^{142}Ba show up at the expected energies and are discussed in Section 6.1. They are marked with a diamond.

In order to work out the nature of the visible transitions, several pieces of information were utilized: Their detected γ-ray energy can be used to determine consistent energy loops such that two deexcitation paths match the same original level (Ritz combination principle). Particle-γ-γ coincidences play an important role in putting states at their correct places as well. Lastly, the angular dependence of the relative population of all states yields valuable information. This is due to the fact that excitation probabilities of these states are dependent on the scattering parameters. The latter is discussed in-depth in Chapter 7, which deals with the GOSIA analysis. The current chapter provides details on the energies of all visible transitions, their coincidences with other transitions, and a rough idea of their kinematics-dependent behavior.

6.1. Beam purity

The Cold Plasma Ion Source is used at ISOLDE's primary target, as mentioned in Section 4.1.1. Utilizing this particular ion source xenon is easily extracted as anything that is less volatile than a noble gas will stick to the transfer line. The beam leaving the source can therefore be considered clean and all possible contaminants are suppressed before entering ISOLDE's post accelerator.

At the start of the post accelerator the nuclei are bunched and charge bred in REXTRAP and REXEBIS, respectively. The charge breeding process takes 192 ms. While the transport from the primary target to the post accelerator and the acceleration after leaving the electron-beam ion-source and delivery towards the MINIBALL experimental-site takes negligible time, and decays in REXTRAP are lost and not transported further, this is not true for the time spent in the REXEBIS: ^{142}Xe has a half-life of 1.23 s [86]. Its daughter is ^{142}Cs, an odd-odd nucleus, with a half-life of 1.68 s [86]. In turn, the daughter of ^{142}Cs is ^{142}Ba. The half-life of this nucleus is 10.6 min [86].

Using the Bateman equations [94] with the lifetime information of all three nuclei along with the breeding time of the REXEBIS yields a beam composed of 89.8 % xenon, 9.8 % cesium and 0.4 % barium. This is, of course, the value calculated for the target location at the MINIBALL experimental site.

Utilizing this, the expected number of counts in the first 2^+ to ground-state transition in ^{142}Ba can be determined. Here, the obtained yield is normalized to the overall counts in the transition $2_1^+ \rightarrow 0_{\mathrm{g.s.}}^+$ in ^{142}Xe. The estimate amounts to 1300 counts, which reproduces the measured 360 keV peak, shown in Figure 6.3, nicely. Furthermore, hints of the $4_1^+ \rightarrow 2_1^+$ transition at 475 keV of ^{142}Ba are visible. This energy lies close to the 490 keV transition of ^{142}Xe. The intensity of the 475 keV transition of ^{142}Ba is roughly 4 % of the 490 keV transition of ^{142}Xe. The statistical uncertainty of the transition of xenon for all angular subsets is at least 6 % (see Table C.2). This means that even if these two transitions were indistinguishable, the uncertainty of the number of counts would not increase by much. In fact, the resolution is sufficient to distinguish the two close-lying peaks in all spectra.

For the odd-odd daughter ^{142}Cs, the excitation probability is spread over multiple low-lying transitions, rather than being concentrated in the lowest main-band transition as is the case for the even-even barium. Traces of several of the lowest-lying transitions are visible in the spectrum. These ^{142}Cs transitions are given in Table 6.1 with their respective intensities relative to the $2_1^+ \rightarrow 0_{\text{g.s.}}^+$ transition in ^{142}Xe.

Table 6.1.: Visible transitions of ^{142}Cs in the Doppler-corrected γ-ray energy-spectra. The given efficiency-calibrated intensities are relative to the observed $2_1^+ \rightarrow 0_{\text{g.s.}}^+$ transition in ^{142}Xe. Initial and final level energy are noted as far as they are available in literature [95].

Measured γ-ray energy	Relative intensity	Literature γ-ray energy	Inital level energy	Final level energy
171 keV	0.4 %	171 keV	210 keV	39 keV
197 keV	0.4 %	197 keV	210 keV	13 keV
204 keV	0.4 %	203 keV	203/343 keV	0/39 keV
219 keV	0.2 %	219 keV	304/.. keV	85/.. keV
243 keV	<0.5 %	243 keV	243 keV	0 keV
251 keV	<0.5 %	251 keV	251 keV	0 keV
380 keV	0.4 %	380 keV	419 keV	39 keV
429 keV	0.1 %	428 keV	733 keV	304 keV

The β-decay spectra, i.e., the not Doppler-corrected γ-ray MINIBALL energy-spectra created without requesting any particle coincidences, present an additional way of checking for contaminants in the beam. All the known transitions of the daughter nuclei of ^{142}Xe down to ^{142}Ce were compared with the β-decay spectra. Typical background in the ISOLDE hall was taken into consideration as well. No discrepancy was found within the spectra.

Hence, the beam is considered clean for the further analysis, except for the first daughter and granddaughter of ^{142}Xe.

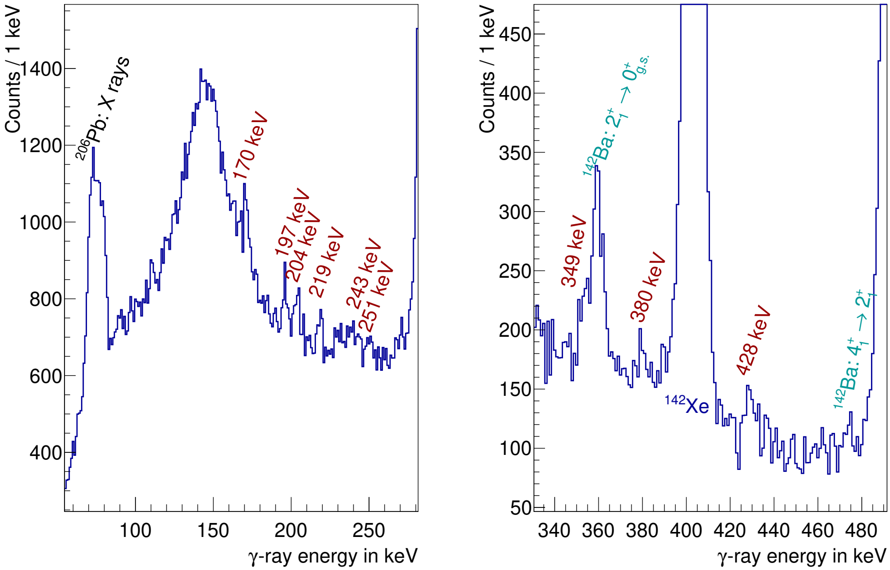

Figure 6.3.: Two partial Doppler-corrected γ-ray spectra showing signatures of the daughter and granddaughter of ^{142}Xe. The known transitions in the odd-odd nucleus ^{142}Cs are marked in red with their respective energies, while the two lowest-lying transitions of the yrast band of ^{142}Ba are shown in cyan. Doppler corrected with respect to beam particles, background subtracted, and efficiency calibrated.

6.2. The main band

In the Doppler-corrected γ-ray energy spectra in Figure 6.2 the yrast band up to the 8^+ state is visible. All main-band transitions are visible at the expected energies. Table 6.2 lists the transitions with their respective mean energies $\mathrm{E}_{\mathrm{mean}}$ and resolutions R. The resolution is defined as

$$R = \frac{\mathrm{FWHM}}{\mathrm{E}_{\mathrm{mean}}} \,. \tag{6.1}$$

Table 6.2.: Main-band transitions in ^{142}Xe including their mean energies and resolutions as defined in Equation 6.1. The given literature energies are taken from reference [96]. The values given in [90, 9] agree within the uncertainties.

Inital level Spin$^{\mathrm{Parity}}$	Final level Spin$^{\mathrm{Parity}}$	Literature γ-ray energy	Measured γ-ray energy	Resolution
2^+_1	$0^+_{\mathrm{g.s.}}$	287.2 (2) keV	286.8 keV	1.7 %
4^+_1	2^+_1	403.5 (2) keV	403.5 keV	1.4 %
6^+_1	4^+_1	490.4 (2) keV	490.5 keV	1.3 %
8^+_1	6^+_1	551.1 (2) keV	551.5 keV	1.2 %
10^+_1	8^+_1	610.4 (2) keV	- keV	- %
12^+_1	10^+_1	671.7 (5) keV	- keV	- %

The $10^+_1 \rightarrow 8^+_1$ transition, expected at 610 keV, is the lowest-lying transition of the main band that is not clearly visible. This is not to say that this transition would not be at that exact place, just that the excitation probability for a transition that far up in the band is not sufficient in this Coulex experiment. A transition at 610 keV is not visible in the spectrum in Figure 6.2c, which is obtained by taking into account only events for which the backwards facing DSSSD was hit. This is the kinematics range in which the highest-lying main-band transition is expected to be visible. Particle-γ-γ coincidences as shown in Figure 6.4 suggest that what is visible in the 610-612 keV range is an overlap of multiple transitions. Namely, the close-lying $6^+_\gamma \rightarrow 6^+_1$ transition at an energy of 603 keV, which is discussed in Section 6.3.4, and the $3^+_\gamma \rightarrow 4^+_1$ transition at 612 keV, see Section 6.3.2, rather than the depopulation of the 10^+ state as there are no visible coincidences with the $8^+_1 \rightarrow 6^+_1$ yrast-band transition.

The $12^+_1 \rightarrow 10^+_1$ transition at 672 keV is definitely not visible in this data set.

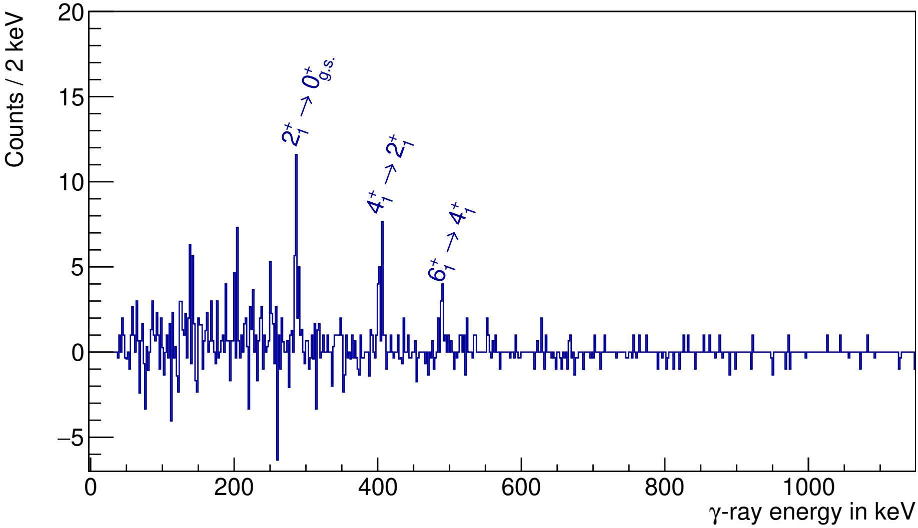

Figure 6.4.: Doppler-corrected particle-γ-γ coincidence γ-ray spectrum for the $10^+_1 \to 8^+_1$ transition at 610-612 keV. Background subtracted, raw counts. For more details see text.

6.3. The gamma band

The most prominent features of the Doppler-corrected γ-ray energy spectra besides the main band are the transitions at 703 keV, 773 keV and 1060 keV. Additional weaker transitions can be found investigating more extreme angles, such as the 1016 keV and the 603 keV transitions. All these transitions have in common that they have not been reported in any publication previously.

As Coulomb excitation experiments readily excite low-lying collective 2^+ states, it is intuitive to assume the head of a gamma band just like the one reported in the neighboring ^{140}Xe [97].

Table 6.3 shows the determined level energies of all assumed members of the band. This section is dedicated to the presentation of details on each of the levels and the evidence for their respective placement.

Table 6.3.: Gamma-band candidates in ^{142}Xe including their energies. Spin and parity assignments are based on coincidences and energies only.

Spin$^{\text{Parity}}$	Level energy
2^+_γ	1060 (1) keV
3^+_γ	1303 (1) keV
4^+_γ	1394 (1) keV
6^+_γ	1784 (1) keV

6.3.1. The 2^+_γ state

The energetic difference between the two γ-ray lines at 773 keV and 1060 keV matches exactly the energy of the $2^+_1 \rightarrow 0^+_{\text{g.s.}}$ transition. The intensity of the two transitions is of the same order of magnitude. In Figures 6.5 and 6.6 the projections of the particle-γ-γ matrix for each of the two transitions are shown. The 773 keV line is coincident with the $2^+_1 \rightarrow 0^+_{\text{g.s.}}$ transition, while the one at 1060 keV is not coincident with any other γ-ray energy. Consider here, that the number of raw counts in the coincidence spectrum would be comparable to the ones shown in Figure 6.5, as they possess a similar strength. Therefore, the transition with the energy of 1060 keV is parallel to the $2^+_1 \rightarrow 0^+_{\text{g.s.}}$ transition.

Based on the comparitively high intensity, it is unlikely that this decaying state is part of the negative parity band as 1^-_1 state. Furthermore, a 0^+ state would not decay to the $0^+_{\text{g.s.}}$. Together with the information on the existence of the gamma band in ^{140}Xe [97], this leads to the assumption of this state being a 2^+_γ state.

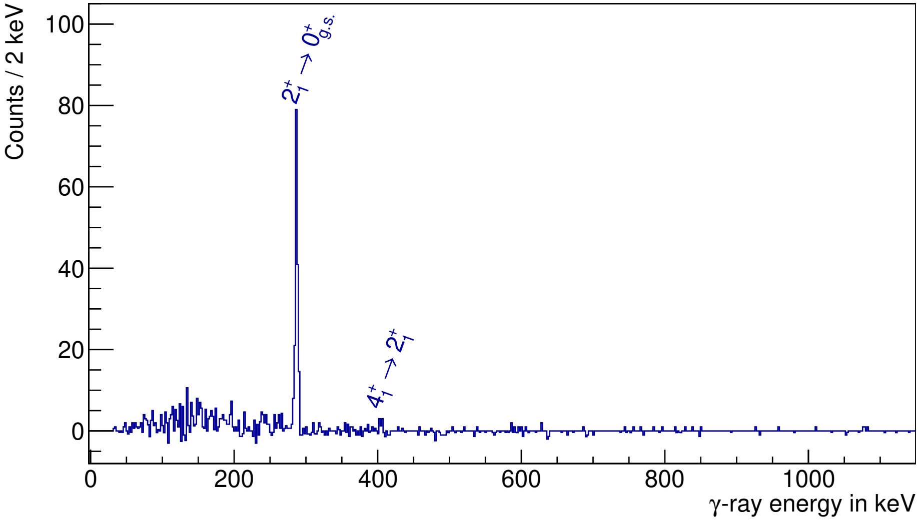

Figure 6.5.: Doppler-corrected particle-γ-γ coincidence γ-ray spectrum for the $2_\gamma^+ \rightarrow 2_1^+$ transition at 773 keV. Background subtracted, raw counts.

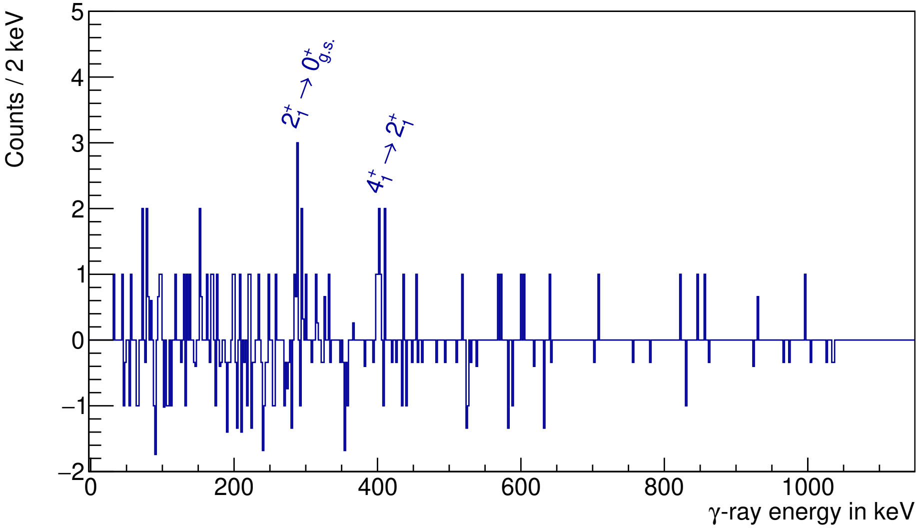

Figure 6.6.: Doppler-corrected particle-γ-γ coincidence γ-ray spectrum for the $2^+_\gamma \rightarrow 0^+_{\text{g.s.}}$ transition at 1060 keV. Background subtracted, raw counts.

In order to determine the branching ratio of this state, the intensities of both observed transitions are needed. The fact that one of the transitions sits on top of the smeared target region complicates the analysis. This occurs because, when creating this spectrum, the ^{206}Pb target transition with an energy of 803 keV is Doppler corrected assuming that the γ ray stems from ^{142}Xe, i.e., is emitted by the beam instead of the target, which in itself shows an impact-parameter dependence. This leads to a warped number of counts depending on what center-of-mass range is considered when determining the intensity of the 773 keV transition. The correction applied to account for this effect is discussed in detail in the next subsection.

The two transitions are also seen in unpublished beta-decay data [92], supporting the interpretation as a possible 2^+_γ state.

The relative branching of $\frac{\mathrm{Y}(2^+_\gamma \to 0^+_{\mathrm{g.s.}})}{\mathrm{Y}(2^+_\gamma \to 2^+_1)}$ is 57 (6) %, as determined using the results of the following subsection.

Target area correction

The solid blue line in Figure 6.7 shows the kinematics-dependent deviation of the counts in the 1060 keV peak C_{1060} over the counts in the 773 keV transition C_{773}, normalized to the mean ratio r_{mean} calculated from all data sets, i.e., $\frac{C_{i,1060}/C_{i,773} - r_{\mathrm{mean}}}{r_{\mathrm{mean}}}$. The ranges are the same as in the experiments defined in Section 7, i.e., the ratio with the lowest range number equates to the highest shown impact-parameter and vice versa. A clear angular dependence is visible at low impact parameters. This is interesting as this suggests that the 773 keV line stemming from the transition $2^+_\gamma \to 2^+_1$ comprises another higher-lying transition, a transition with a small enough count number such that it is not visible in the particle-γ-γ coincidence spectra.

Another possible explanation is the not exactly determinable impact of the smeared target background. In order to get an idea of the influence of the wrongly corrected target peak on the number of counts in the 773 keV transition it is instructive to first do a Doppler correction with respect to the ^{206}Pb target nuclei, determine all γ rays that have an energy that lies within the target peak and then look at the distribution of these counts after a Doppler correction with respect to ^{142}Xe. Figure 6.8 shows the latter with its angular dependence, i.e., the kinematics or impact-parameter dependence, of the distribution.

Though not an exact way of determining the real influence, it displays how such an impact can occur.

To investigate this further, the set of events is used for which the full kinematical information is available, i.e., events in which both target and projectile are detected. This eliminates effects which are introduced due to wrongly identified particles. For each angular range, a set of two histograms is created. The first one is the standard γ-ray energy-spectrum constructed with respect to ^{142}Xe and without any further alteration. The second is the

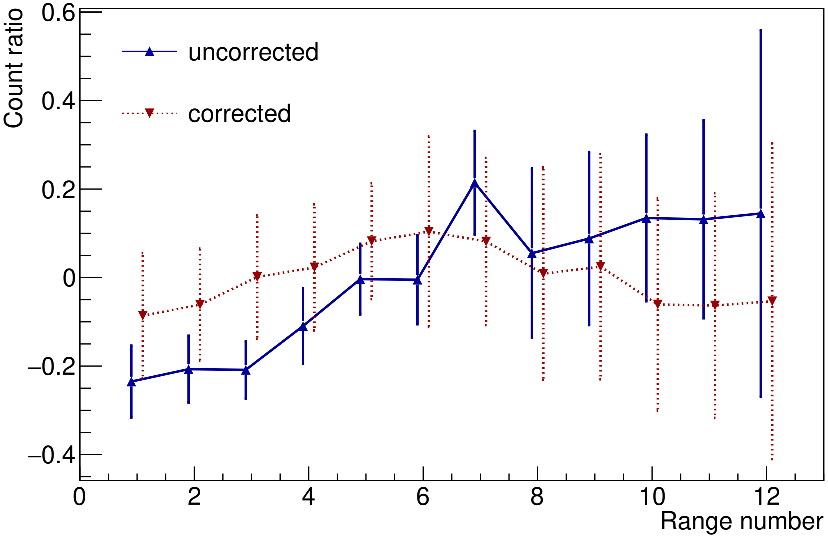

Figure 6.7.: Range-dependent count deviation of the $2^+_\gamma \rightarrow 0^+_{\text{g.s.}}$ transition to the $2^+_\gamma \rightarrow 2^+_1$ transition, normalized to the mean ratio calculated from all data sets. Solid line without correction for smeared target effects, dotted line includes the correction. Both data sets are normalized to their respective arithmetic mean.

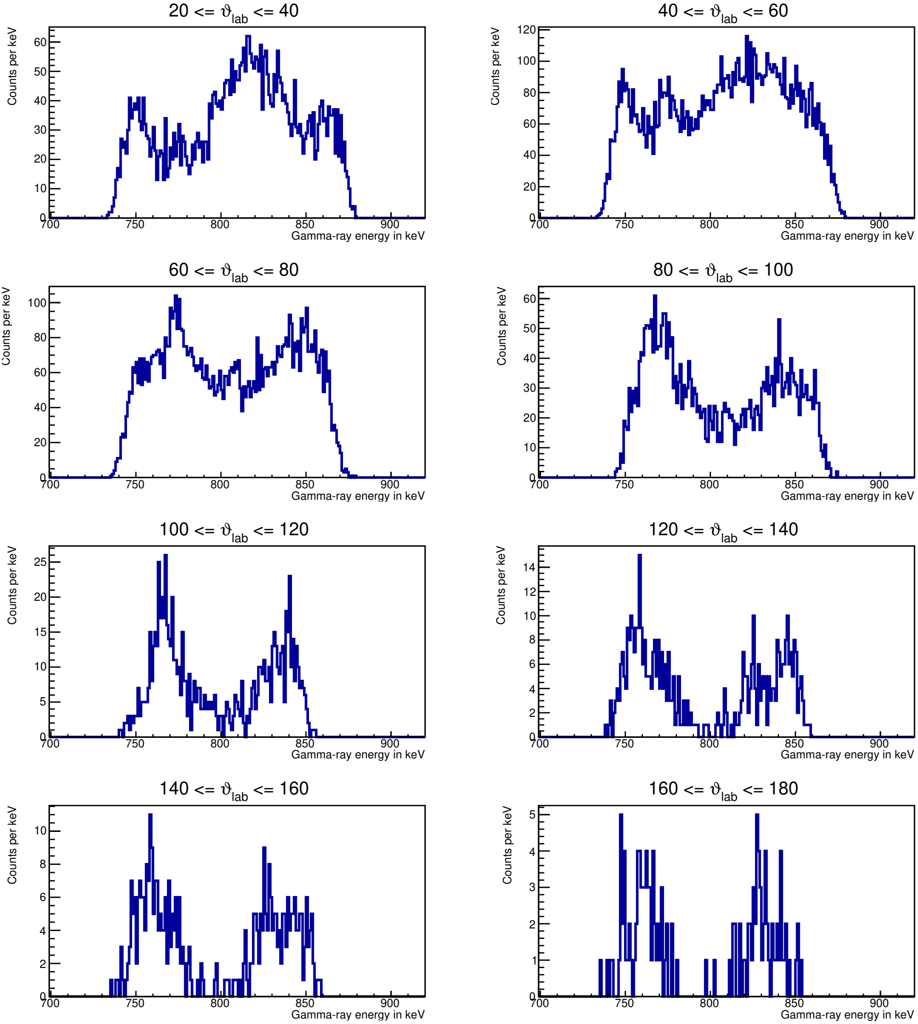

Figure 6.8.: Angular dependence of the smearing of the target transition in the γ-ray energy-spectra Doppler corrected with respect to beam particles. Only those counts are shown that lie within the target-peak area at 803 keV when Doppler correcting with respect to the target.

same except for being reduced by the counts which were identified to lie within the target peak range for the Doppler correction with respect to ^{206}Pb. The ratio of the counts as determined from these two spectra is then used to correct the overall counts in the 773 keV transition without restricting to full kinematic availability.

The validity of this approach is tested by looking again at the impact-parameter dependent deviation between the countrate of the two transitions. The dotted red line in Figure 6.7 shows the result. The angular dependence is essentially gone, which means that we are in fact looking at a peak originating from one transition, only. This matches the interpretation of the particle-γ-γ coincidence spectrum in Figure 6.6.

The disadvantage of this method is that it leads to an increased uncertainty of the counts in the 773 keV transition, an issue that cannot be circumvented without additional information from other data.

In conclusion, within the experimental errors the intensity ratio $\frac{\mathrm{Y}(2^+_\gamma \to 0^+_{\mathrm{g.s.}})}{\mathrm{Y}(2^+_\gamma \to 2^+_1)}$ remains constant as function of the scattering angle indicating that both transitions stem from the decay of the same state.

6.3.2. The 3^+_γ state

Initial evidence of the 1303 keV level is given by the measured γ-ray energy of 1016 keV, which is in coincidence with the $2^+_1 \to 0^+_{\mathrm{g.s.}}$ transition, only. The crucial hint for the nature of this state came from discussions with the group analyzing beta-decay data obtained at RIKEN [92]. For our Coulex-data case, the fact that 612 keV lies so closely to the first not clearly observed main-band transition, the $10^+_1 \to 8^+_1$ transition with an energy of 610 keV, and also next to a new transition with an energy of 603 keV, which is discussed in Section 6.3.4, leads to an ambiguity even when considering particle-γ-γ coincidences.

For the beta-decay spectra, the 612 keV transition is identified as feeding the 4^+_1 state. On the basis that the 10^+_1 state is not expected to be populated via beta decay at all, it can be said that the state decays via this transition. This is also confirmed by the absence of any signatures of the 6^+_1 state or other higher-lying yrast-band members in their beta-decay spectra [91].

Figure 6.9 shows the projection of the particle-γ-γ matrix for the 1016 keV transition. While this spectrum shows convincing coincidences with the $2^+_1 \to 0^+_{\mathrm{g.s.}}$ transition, the case of the 612 keV transition is more complicated. The spectrum already plotted in Figure 6.4 is interpreted as showing coincidences of two or three transitions, namely the $3^+_\gamma \to 4^+_1$ transition at 612 keV, the $10^+_1 \to 8^+_1$ transition with an energy of 610 keV, and the new higher-lying transition at the flank of this peak with an energy of 603 keV, which is discussed below in Section 6.3.4. Hence, coincidences with the lowest two main-band transitions are strongly visible as they are expected as coincidences for all these transitions. Additionally there are weaker coincidences with the $6^+_1 \to 4^+_1$ transition.

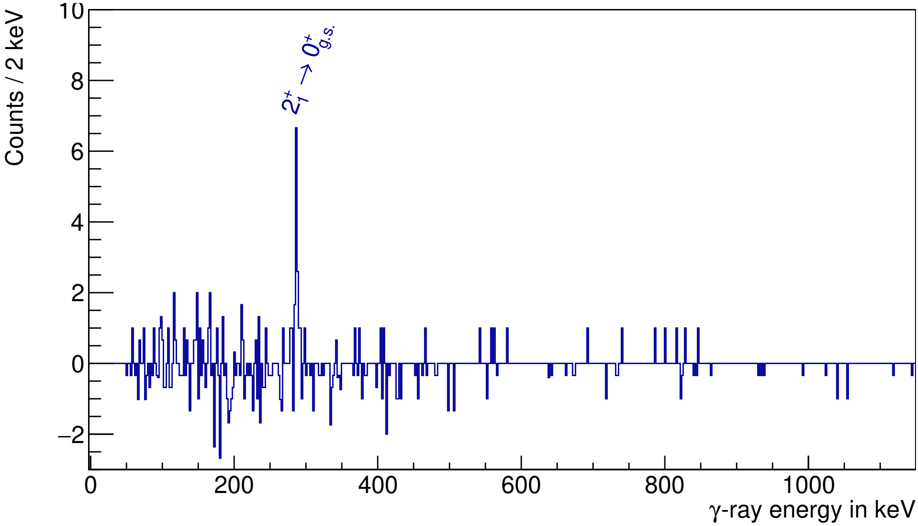

Figure 6.9.: Doppler-corrected particle-γ-γ coincidence γ-ray spectrum for the $3_\gamma^+ \to 2_1^+$ transition at 1016 keV. Background subtracted, raw counts.

For the GOSIA analysis the origin of the few visible counts is not too problematic, as the count rates in that area are well below the set upper limits for invisible transitions for each of the considered kinematical ranges.

Systematically, a 3^+_γ state fits at this position, and is also seen for the nearby nuclei ^{140}Xe [97], ^{142}Ba [98], and ^{144}Ba [99].

As for the branching ratios this case is very complicated. As described above it is not clear whether the visible counts stem from the depopulation of the 10^+_1 state, the 3^+_γ state, or both, and the nearby 603 keV transition impedes the analysis further. Using the upper limits method [100] and making the crude assumption that all Coulex counts stem from this particular transition, the branching ratio $\frac{Y(3^+_\gamma \rightarrow 4^+_1)}{Y(3^+_\gamma \rightarrow 2^+_1)}$ is at least below 66 % requesting a 1σ confidence level. Looking at the beta-decay spectra [91] suggests that the branching ratio is significantly lower than that.

A third possible decay path exists in the transition from the 3^+_γ state to the 2^+_γ state with a γ-ray energy of 243 keV. This is a region wherein multiple transitions of the odd-odd daughter-nucleus ^{142}Cs lie. Determining a sensible background proved impossible, therefore no reliable estimate could be made. For the GOSIA analysis it is assumed that the strength of this transition falls below the set upper limit for all angular ranges.

6.3.3. The 4^+_γ state

The only evidence for the state at 1394 keV is the $4^+_\gamma \rightarrow 4^+_1$ transition at 703 keV. This is also the transition for which using addback results in an actual disadvantage: The pile-up peak consisting of the sum of the $2^+_1 \rightarrow 0^+_{\mathrm{g.s.}}$ and the $4^+_1 \rightarrow 2^+_1$ at 691 keV lies right next to the aforementioned transition at 703 keV. Furthermore, the smeared target transition is located fairly close-by, a fact that complicates the background subtraction further.

The coincidence spectrum is shown in Figure 6.10. Clear coincidences with the two lowest main-band transitions are visible. The coincidences with the $6^+_1 \rightarrow 4^+_1$ transition are interpreted as originating from the nearby pile-up transition at 691 keV. If the 703 keV transition was feeding the 6^+_1 state, the coincident count rate is expected to be higher.

Again, from systematics, this is assumed to be the 4^+_γ state, supported by information from beta-decay spectroscopy [92], where also a transition with an energy of 703 keV, which feeds the 4^+_1 state, is visible.

Several transitions are allowed to depopulate a 4^+_γ state at this energy: Two transitions within the γ band, namely the $4^+_\gamma \rightarrow 3^+_\gamma$ transition with 91 keV and a $4^+_\gamma \rightarrow 2^+_\gamma$ transition with 334 keV, are possible. Likewise, transitions connecting to the energetically lower-lying main-band states, 2^+_1, 4^+_1 and 6^+_1, are allowed.

It is interesting to note, that the 1107 keV transition depopulating this state via the 2^+_1 state is invisible in the Coulex data as well as the beta-decay spectra [91]. Employing the same method [100] as for the other possible low-intensity transitions, the relative intensity

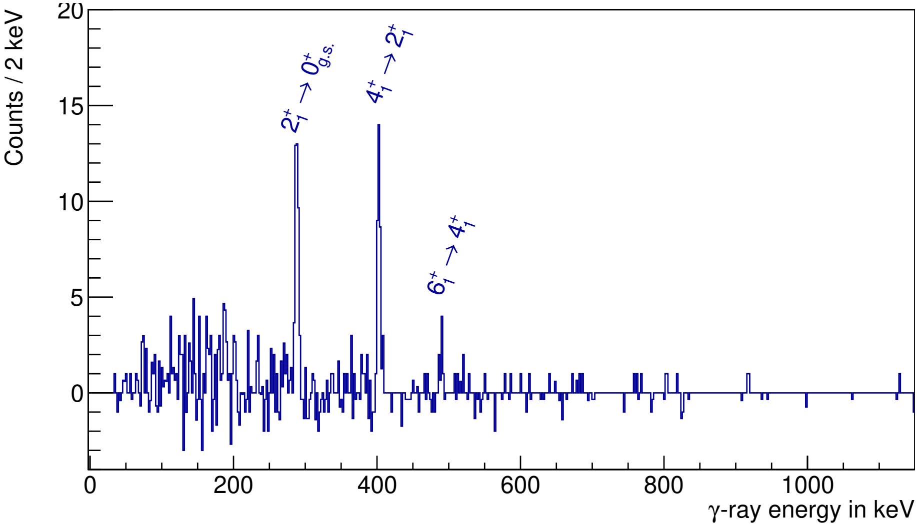

Figure 6.10.: Doppler-corrected particle-γ-γ coincidence γ-ray spectrum for the $4_\gamma^+ \rightarrow 4_1^+$ transition at 703 keV. Background subtracted with raw counts.

for the $4^+_\gamma \to 2^+_1$ transition compared to the $4^+_\gamma \to 4^+_1$ transition is determined to be below 8 % for a strict 2σ confidence level and below 6 % requesting only a 1σ confidence level. The branching ratio $\frac{\mathrm{Y}(4^+_\gamma \to 2^+_1)}{\mathrm{Y}(4^+_\gamma \to 4^+_1)}$ is estimated utilizing the same method to be 4 (2) %. This value is used as an additional constraint in the GOSIA analysis.

A possible $4^+_\gamma \to 6^+_1$ transition has an energy of 213 keV, thus lying in an area wherein multiple transitions of the odd-odd daughter-nucleus ^{142}Cs are visible in our data set. The strongest transitions of ^{142}Cs in that region are transitions with an energy of 196 keV, 204 keV, and 219 keV, respectively. Furthermore, this region is affected by the Compton-scattered events stemming from the 287 keV transition. Both these facts make a reliable background determination as is needed for the above employed method impossible. Therefore, this method can not be used and instead the crude assumption is made that the state does not decay via this path. For the GOSIA analysis as described in Section 7, the count rate is assumed to be below the respective upper limits for each of the defined angular ranges.

The determination of the intensity of the $4^+_\gamma \to 3^+_\gamma$ transition with an energy of 91 keV is affected by similar problems. The region is part of the Compton background of the same 287 keV transition and, on the low-energy side, the X rays stemming from the lead target are visible. This makes an exact determination of an upper limit impossible. What can be said, though, is that the detected γ rays depopulating the 3^+_γ state encompass at most a sixth of what is seen for the 4^+_γ state, and that an exclusive population of the 3^+_γ state from the above-lying 4^+_γ state is unphysical. Therefore, in the scope of the GOSIA analysis, the uncertainty stemming from the unknown branching ratio for this transition is covered by the set upper limits.

The last possible decay path of the 4^+_γ state is the transition via the 2^+_γ state with an energy of 334 keV. In the Coulex data a fairly strong peak can be identified using the upper limits method [100], which would amount to a relative intensity of 46 % with respect to the visible $4^+_\gamma \to 4^+_1$ transition for a set 2σ confidence level. However, a transition at that energy is not visible in the beta-decay spectra [91], nor do particle-γ-γ coincidences show anything but background. Consequently, this transition may belong to ^{142}Cs or consist of background, as the background determination for this case is also rather challenging. Therefore, it is assumed for this transition as well that the set upper limits are sufficient for the GOSIA analysis.

6.3.4. The 6^+_γ state candidate

A weak transition at 603 keV is visible at high center-of-mass angles, see Figure 6.2b. This indicates that this transition belongs to a state somewhere further up in the level scheme. It is instructive to compare this to the Doppler-corrected spectrum plotted in Figure 6.2c, which is obtained by looking at events from the back CD only. If the transition at 603 keV was part of the main band, it would be visible in that spectrum, too. The 603 keV transition also

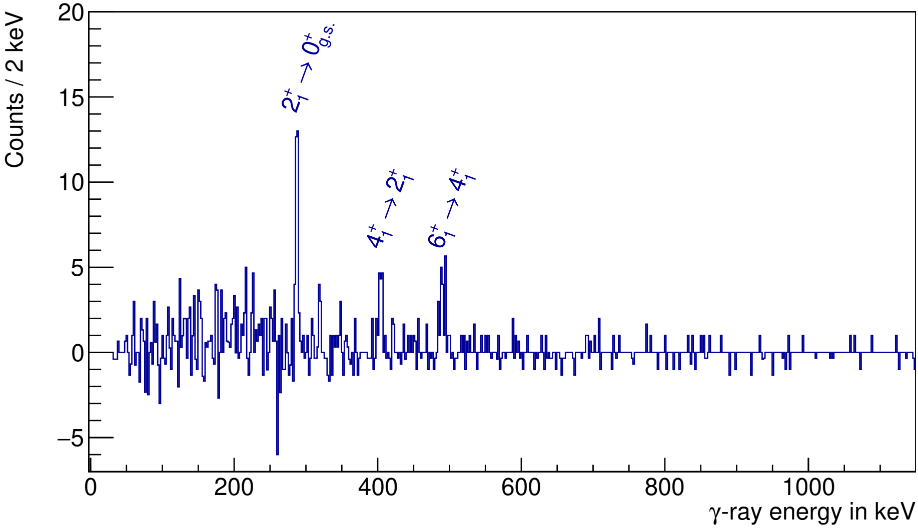

Figure 6.11.: Doppler-corrected particle-γ-γ coincidence γ-ray spectrum for the $6_\gamma^+ \to 6_1^+$ candidate at 603 keV. Background subtracted, raw counts.

lies close to the $3_\gamma^+ \to 4_1^+$ transition with an energy of 612 keV and the $10_1^+ \to 8_1^+$ transition with an energy of 610 keV, which complicates the analysis.

Though when looking at the coincidence spectrum in Figure 6.11 the coincidences with the $2_1^+ \to 0_{\text{g.s.}}^+$ transition, $4_1^+ \to 2_1^+$ transition, and the $6_1^+ \to 4_1^+$ transition look fairly convincing.

Besides a decay from a 6_γ^+ state, a transition from the 5_γ^+ state is possible according to the selection rules. As the 3_γ^+ state is fairly weakly populated in our Coulex data, and the $5_\gamma^+ \to 4_1^+$ transition is by far the strongest decay path for the 5_γ^+ state in the neighboring ^{140}Xe [97], this suggests a 6_γ^+ state, though the decay from a 5_γ^+ state can not be ruled out.

Therefore, this is put as a $6_\gamma^+ \to 6_1^+$ transition candidate.

The corresponding $6_\gamma^+ \to 4_1^+$ transition is calculated to have an energy of 1093 keV. Using the upper limits method [100] for both transitions, the count ratio of the $6_\gamma^+ \to 4_1^+$ transition to the $6_\gamma^+ \to 6_1^+$ transition is below 0.5.

A transition to the 4_γ^+ state is calculated to have an energy of 481 keV, which is too close to the high-statistics $6_1^+ \to 4_1^+$ transition at 490 keV and the $4_1^+ \to 2_1^+$ transition at 475 keV of the ^{142}Ba daughter nucleus, so that no reliable estimate can be calculated. Again, from systematics, the transition is assumed to be below all limits in the scope of the GOSIA

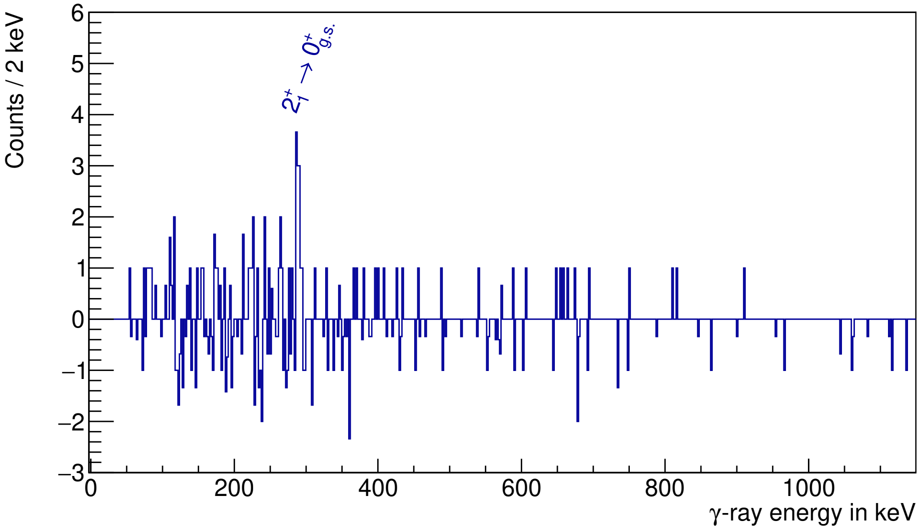

Figure 6.12.: Doppler-corrected particle-γ-γ coincidence γ-ray spectrum for the $3^-_1 \rightarrow 2^+_1$ transition at 971 keV. Background subtracted with raw counts.

analysis.

6.4. Negative-parity candidates

6.4.1. The 3^-_1 state

The 3^- state at 1258 keV was proposed as part of the octupole band [9]. The predominant decay path is expected to be the $3^- \rightarrow 2^+_1$ transition with an energy of 971 keV. Figure 6.12 shows the particle-γ-γ coincidence γ-ray spectrum for the $3^- \rightarrow 2^+_1$ transition. This finding supports the claim of [9].

The $3^- \rightarrow 4^+_1$ transition is also expected to be a possibility, even though it is weaker. In our Coulex data, there may be a weak signature of this line at the expected energy of 567 keV.

Utilizing the upper limits method [100] and requesting a significance level of 50 % the branching ratio $\frac{\mathrm{Y}(3^- \rightarrow 4^+_1)}{\mathrm{Y}(3^- \rightarrow 2^+_1)}$ is determined as 22 (15) %, including the statistical uncertainties for the $3^- \rightarrow 2^+_1$ and a 1σ uncertainty as defined in [100]. A more reliable branching ratio is unavailable in literature at the moment. The branching ratio for the same states in the nearby ^{142}Ba is, with 20 (8) %, comparable [101].

A branching ratio to the 1^-_1 state is not needed as this state probably lies above the 3^-_1 state as discussed in the next subsection.

6.4.2. The 1^-_1 state candidate

Before the Coulex experiment the location of the 1^-_1 state was unknown. Discussions with the group analyzing beta-decay data from RIKEN [92] suggest that the 1^-_1 state is located slightly above the 3^-_1 state. The same is true for the nearby nucleus ^{142}Ba [101, 95], wherein too the 3^-_1 state is found below the 1^-_1 state.

In our Coulex data both possible transitions are invisible, though using the upper limits method [100] the $1^-_1 \rightarrow 0^+_{\mathrm{g.s}}$ transition candidate and the $1^-_1 \rightarrow 2^+_1$ transition candidate are estimated to have count ratios below 42 % and 38 %, respectively, relative to the $3^-_1 \rightarrow 2^+_1$ transition, when requesting a 1σ confidence level. Note that the method employed is not capable of predicting that a peak does not exist.

6.4.3. The 5^-_1 state candidate

The 5^-_1 state was proposed at an energy of 1516 keV as part of the octupole band [9]. Only the $5^- \rightarrow 4^+_1$ transition at 826 keV was observed and therefore, based on systematics arguments, the state was put at its energy.

In the Coulex data, this energy is located where the smeared target transition is visible. No signatures of the state are seen. Based on this fact, together with the weak $3^-_1 \rightarrow 2^+_1$ transition count rate, the assumption is made that the state is not populated.

For the GOSIA analysis the 5^-_1 state is set as a buffer state connecting to the 3^-_1 state only.

7. GOSIA analysis and results

The analysis was performed using the literature lifetime $\tau(2_1^+)$ [87] as normalization. Such a normalization is mandatory to convert the measured γ-ray intensities to absolute excitation cross sections as beam intensity, efficiency and angular acceptance of the particle detector, and efficiency and dead time of the γ-ray detector are typically not known to sufficient precision.

The advantage of this approach as opposed to normalizing towards the target is that absolute efficiencies and acceptances of both the MINIBALL array and C-REX are averaged out.

For the further analysis of the data and the extraction of the relevant matrix elements GOSIA [43] is used. A detailed overview on the required input for GOSIA is available in the GOSIA manual [41] and is shortly discussed in Section 7.1. After that, the data extracted from spectra is presented in Section 7.2, which is also meant to be an overview on the input that is given to GOSIA. Subsequently, the fitting scheme and restrictions on matrix elements are discussed in Section 7.3.

Lastly, in Section 7.4, results are presented and sources of uncertainties are discussed, with a focus on systematic uncertainties.

7.1. Required input

In order to have the GOSIA code determine the best matrix elements, it needs several input files. Without going too much into detail about how the information is split over those files and distinct jobs, in this section the required input information is discussed.

Generally, data sets that are defined in GOSIA are referred to as experiments. Such an experiment is characterized by a certain beam and target nucleus, the beam energy, and the corresponding angular information of the detectors.

The latter is split in the two typical detector systems: The γ-ray detector, here the high-purity germanium array MINIBALL, needs to be put in with its full positional information relative to the target, including its physical dimensions, i.e., the crystal size. This enables GOSIA to take angular correlations of the γ rays into account. As MINIBALL is used frequently for this type of experiment, the measures are already available. Concerning the efficiency treatment, the user is left to either define the efficiency at the dedicated point and supply GOSIA with uncorrected γ-ray yields for each experiment. Or, as was done here, to set the efficiency to one and write the efficiency-corrected yields into the file.

The second detector system is the particle detector. GOSIA allows to include various detector shapes. Splitting information obtained by a silicon detector up into several distinct ranges is common practice as this allows a more selective determination of the impact-parameter dependent cross-sections. Therefore, an experiment may be defined only as part of the particle detector, if the corresponding γ-ray yields are given. The input of the exact angular information of the particle detector can be a delicate procedure, which is described in a bit more detail in Section 7.1.1.

The aforementioned γ-ray intensities, or so-called yields, need to be given for each experiment along with their respective uncertainties and corresponding transition.

Nuclear structure information, such as spin, parity and excitation information of each of the participating levels, need to be provided. It is necessary to include higher-lying energy levels than the highest ones observed, as GOSIA will overestimate the transition amplitude of the final level of a band.

In order to then provide a set of matrix elements, which GOSIA expects in a specifically sorted order, another small code, MEGEN, can be used. The user has to decide which multipolarities need to be considered. For this work E1, E2, E3, and E4 transitions were allowed.

Furthermore, electron-conversion coefficients for all transitions and multipolarities need to be provided. These were determined using BrIcc [102]. Also, the stopping powers as calculated with SRIM [85] are needed. GOSIA integrates over a given beam-energy range, i.e., incident and exit beam energy in the target, effectively calculating the target thickness.

As additional input, spectroscopic data such as lifetimes, branching ratios, and matrix elements can be included.

Lastly, several control flags can be set, which can speed up or slow down the analysis considerably. Examples for such are controls specifying output, the method used to perform the minimization, or which matrix elements and angular ranges should be excluded from the analysis. For details see the GOSIA manual [41].

7.1.1. Detector shape and normalization constants

As discussed before, the beam was not only not centered during the entire campaign, but there are also two distinct sets, that were treated separately. Though the effects were corrected as described in Section 5.10.2, this has implications for the analysis using GOSIA.

The angular coverage, as was seen by the particles dependent on their corresponding beam shift, is different for each and every single run that shows a unique beam shift. Figure 7.1 shows the angular coverage of the DSSSD mounted in forward direction, requesting only the area that was covered for all runs.

It is intuitive that only the overlap region can be used for the analysis. GOSIA does not

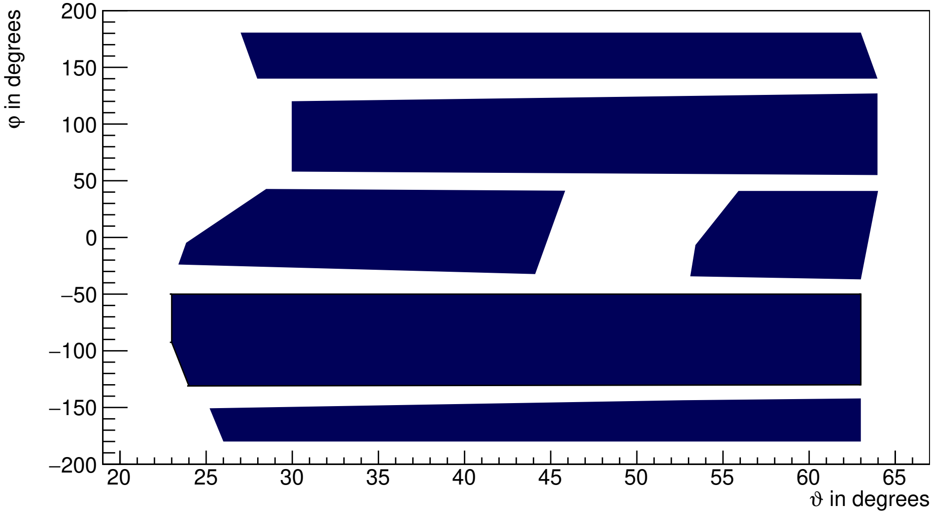

Figure 7.1.: The angular coverage of the DSSSD mounted in forward direction in the laboratory system for the complete campaign is shown. The asymmetric shape stems from the fact that the beam was off-center, and the two defined sets show a distinct beam shift. Only angular areas are marked that are covered for both sets.

know about beam-shift related problems and will always assume that every given range was covered during the entire campaign. That leads to problems especially when extreme ϑ ranges are not reflected in the data set. Take as an example the innermost range. The cross sections are different there and the contribution of that area to the totally expected γ-ray yield will be overestimated when not explicitly removing it.

GOSIA asks for the specific φ ranges per ϑ meshpoint as defined in [41]. This means the user has to take special care when providing these numbers, specifically at endpoints of the detector. A good way to cross check the result as GOSIA understands the shape is to take a look at the determined normalization constants for the single experiments that GOSIA calculates. It is also possible to calculate those via several approaches as given in [44]. This way problems could be identified and the detector shape defined such that GOSIA has the expected understanding of the shape.

7.2. Segmentation of data into angular bins and γ yields

The forward facing DSSSD was segmented into 12 angular ranges, which were chosen such, that the peak with the lowest statistics of the main-band transitions and the visible transitions deexciting the 2^+_γ and the 4^+_γ state exhibit no more than 50 % statistical uncertainty including the respective efficiency-related uncertainties.

In order to get an estimate of the population of both the 3^-_1 and the 3^+_γ state, the FCD was also once only split in two ranges, which were used to determine the E3 matrix element describing the $0^+_{\text{g.s.}} \rightarrow 3^-_1$ transition.

Further to this, the barrel part is given as one range and the BCD is given as another. Making it 16 experimental ranges overall.

Table 7.1 lists the chosen angular ranges. Note, that the barrel detector overlaps some of the BCD, this area is excluded in the GOSIA analysis, similarly as done for the uncovered FCD ranges.

In Appendix C the efficiency-corrected yields for each of the transitions including their uncertainties are shown in the Tables C.2, C.3, C.4, C.5, and C.6.

7.3. Fitting scheme

GOSIA fits electromagnetic matrix elements to Coulex data by considering both the excitation and the subsequent deexcitation process. The matrix elements serve as parameters and are varied.

The measure of the best solution is whether the least-squares static S as defined in Equation 3.45 is smallest. To ensure that the search converges a sufficient number of γ-ray yields and other experimental data as compared to the number of free matrix elements has to be provided.

The challenge with this particular data set was a rich number of observed transitions together with little information available in literature. This section aims to give an overview on how the fit of the matrix elements using GOSIA was performed.

As starting point an exclusive description using E2 matrix elements was chosen. In this first step, only the main band and the strongest transitions connecting to the gamma band, i.e., the transitions $4^+_\gamma \rightarrow 4^+_1$, $2^+_\gamma \rightarrow 2^+_1$, and $2^+_\gamma \rightarrow 0^+_{\mathrm{g.s.}}$, including the buffer states and in-band connections were allowed. So-called buffer states are needed in GOSIA as unobserved transitions exceeding 1 % can have measurable effects and the truncation of coupled equations results in errors for the calculated corresponding cross sections, granting no physical meaning to the calculated matrix elements connecting to these states [41].

Subsequently, the other possible E2 matrix elements were introduced, or rather released so they could be fit as well. Furthermore, was the influence of possible E4 transitions within the yrast band, and also to the 4^+_γ state, investigated. This is discussed in detail in

Table 7.1.: Angular segmentation of data. The respective γ-ray yields are given in Table C.2, C.3, C.4, C.5, and C.6. All these ranges are understood as laboratory angles under which a ^{142}Xe nucleus was detected.

Range number	Angular range (lab)	Detector type
1	59 - 64 °	Forward DSSSD
2	56 - 59 °	Forward DSSSD
3	53 - 56 °	Forward DSSSD
4	49 - 53 °	Forward DSSSD
5	44 - 49 °	Forward DSSSD
6	40 - 44 °	Forward DSSSD
7	38 - 40 °	Forward DSSSD
8	36 - 38 °	Forward DSSSD
9	34 - 36 °	Forward DSSSD
10	31 - 34 °	Forward DSSSD
11	28 - 31 °	Forward DSSSD
12	23 - 28 °	Forward DSSSD
13	31 - 43 °	Forward DSSSD
14	44 - 62 °	Forward DSSSD
15	110 - 153 °	Barrel
16	153 - 172 °	Backward DSSSD

Section 7.3.2.

As very last part the E1 and E3 matrix elements connecting to the octupole band and mainly the 3_1^- state were investigated.

A determination of the strength of the deexcitation via M1 radiation was not possible, as the information on the participating states of the γ band is not sufficient, see Section 7.3.2.

7.3.1. Minimization procedure

During the minimization phase, several flags controlling the way GOSIA minimizes the least-squares static S can be set. Far away from the minimum a fast approximation as opposed to the full Coulex formalism can be used, which speeds up the minimization process by an order of magnitude. Though, when getting closer to the minimum, especially in this case of many matrix elements, the full Coulex formalism is needed.

Also, a simple steepest descent minimization or a gradient and gradient derivative method are available, as described in detail in [41]. The latter option locates the direction of search better, especially in the frequent case of sharp valleys in the multi-parameter surface.

For this analysis, mostly the full Coulex formalism along with the gradient plus gradient derivative method was used.

Additionally, 2-d scans of sets of two matrix elements were performed, i.e., matrix elements that are expected to have a strong influence on each other were varied. The other matrix elements were then minimized by GOSIA, while leaving the two matrix elements fixed, such that the 1σ contour, indicating the uncertainty for the matrix elements for this set, could be determined.

7.3.2. Matrix elements

The main band of ^{142}Xe consists exclusively of positive parity states with the known sequence $0^+_{\text{g.s.}}$, 2_1^+, 4_1^+, 6_1^+, .. , 16_1^+ [90, 9, 89]. As discussed in Chapter 6.2, transitions stemming from the states up to the 8_1^+ state are visible, with possible hints of the $10_1^+ \rightarrow 8_1^+$ transition. Therefore the states up to the 12_1^+ state are included in the GOSIA analysis. Here, the 12_1^+ state serves as a further buffer state, as is needed for GOSIA.

The transitions within this band are governed by E2 matrix elements, though E4 transitions can, generally speaking, also play a role.

In literature two relevant lifetimes can be found, namely the lifetime of the first 2^+ state being 249(23) ps and the lifetime of the first 4^+ state 54(10) ps [87].

While the lifetime $\tau(2_1^+)$ was used as normalization, it was found that the lifetime of the 4_1^+ state could not be reproduced. This is discussed in the section below.

As discussed in the previous section as starting point an exclusive description allowing E2 excitations was chosen. The influence of E4 contributions was investigated afterwards.

The lifetime of the 4_1^+ state and E4 matrix elements

The original idea was to use both the known ^{142}Xe lifetimes [87] as constraint for the analysis. Though pretty quickly it became apparent that the two lifetimes are inconsistent with the Coulex data[1]. Starting with E2 transitions only, the determined values for the matrix elements connecting the first 2^+ state to the first 4^+ state disagree even within the relatively big uncertainties.

Trying to match the longer lifetime using E4, i.e., only putting the literature value in together with the possibility of an E4 transition, requires a $B(E4;\ 4_1^+ \rightarrow 0_{\mathrm{g.s.}}^+)$ value of above 3500 W.u., which is unphysical considering the following. An older paper suggests an upper limit of 30 W.u. for B(E4,↓) values for the A = 91-150 mass region [40]. Today new literature is available for a few additional nuclei which lie closer to ^{142}Xe, though no nuclei in the immediate proximity.

For the neodymium isotopic chain most information is accessible of all the neighboring nuclei: ^{142}Nd exhibits a B(E4,↓) value range of 0.2 W.u. to 15 W.u. [103], for ^{146}Nd the B(E4,↓) values vary within 0.9 W.u. to 11 W.u. for several transitions [104], ^{148}Nd displays a B(E4,↓) value of 46(14) W.u. [105], and for ^{150}Nd the value 61(33) W.u. was reported [105].

The B(E4,↓) value in ^{140}Ce is 11(1) W.u. [106], and the one for ^{134}Ba is reported as 16 W.u. [107].

So even though the 30 W.u. limit that was suggested in 1981 [40] may have never been quite accurate, a value that is by a factor hundred higher than anything seen in other nuclei, is interpreted as not possible. Therefore, the lifetime of the 4_1^+ state is not used as means to determine the B(E4) values.

An earlier investigation of ^{142}Xe data recorded at REX-ISOLDE did show the same effect, the literature lifetime was too long and could not be matched[2]. The advantage of the REX-ISOLDE data set for this particular state and the determination of its lifetime is the low beam energy. As no high-lying states could be populated at that energy, only a very low-lying state would have lead to problems in the determinability of the reduced transition strength of the $2_1^+ \rightarrow 4_1^+$ transition. Nevertheless, there is no evidence for such a transition in literature, nor do particle-γ-γ coincidences in this work suggest such a state.

Thus, the interpretation is that the shorter lifetime as obtained from the $B(E2;\ 4_1^+ \rightarrow 2_1^+)$ value in the Coulex analysis is correct, while the lifetime given in [87] is not used as additional normalization.

In order to estimate the influence of possible E4 transitions on the other matrix elements, the E4 matrix elements of the main band, namely the matrix elements of the transitions

---

[1] The lifetime $\tau(4_1^+)$ as determined from the B(E2) value in this work is 30 % lower than the lifetime given in [87]. See Section 7.4 for the results.

[2] The author of this work analyzed the REX data in the scope of her Master thesis [108] and afterwards as the final value from the lifetime measurement was available. Trying to employ $\tau(4_1^+)$ by [87], the procedure utilizing the computer program CLX/DCY [59] did not converge.

$0^+_{\mathrm{g.s.}} \rightarrow 4^+_1$, $2^+_1 \rightarrow 6^+_1$, $4^+_1 \rightarrow 8^+_1$, and $0^+_{\mathrm{g.s.}} \rightarrow 4^+_\gamma$ were varied, allowing a reduced transition strength of 30 W.u. for each of the transitions. The changes to the other matrix elements are below 2 %, and are incorporated in the overall systematic uncertainty.

Gamma-band matrix elements and M1 transitions

The relevant states that are interpreted as part of the gamma band, see Section 6.3, are the states 2^+_γ, 3^+_γ, 4^+_γ, and 6^+_γ. As buffer states 7^+_γ and 8^+_γ were set at the energies 2542 keV and 2872 keV, respectively, following [109]. The energetic location of the 5^+_γ state is unknown, and therefore assumed to be at 1622 keV, which is energetically in between the energy of the 4^+_γ state and the 6^+_γ state candidate. The assignment of the 6^+_γ state itself is ambiguous, and just put at its respective energy based on systematics arguments. The influence of the exact energies of these levels on the determined matrix elements is negligible.

It is notable, that deexcitation of the γ-band members happens predominantely via decay to same spin members of the main band. In fact, some of the states are only seen due to the deexcitation via this path.

While the excitation is expected to be governed by E2 transitions, for the deexcitation also M1 transitions and even E0 transitions can play a role. In order to determine the impact of M1 transitions, M1/E2 mixing ratios can be utilized.

For the determination of these mixing ratios angular correlations are used. Unfortunately, for the Coulex data the low number of coincident γ rays along with the fact that the $2^+_\gamma \rightarrow 2^+_1$ transition is located on top of the smeared target structure, makes the determination of this ratio impossible.

Therefore, the M1 matrix elements are set to zero for the analysis.

Matrix elements of negative-parity candidates

Due to the low statistics, the extraction of a B(E3) value relies on several assumptions.

Firstly, it is assumed that the set upper limits on the γ yields for the 5^-_1 state are sufficient, i.e., the seen decay energy of 826 keV [9] belongs to the $5^-_1 \rightarrow 4^+_1$ transition.

Secondly, the assumption is made that the 1^-_1 state is not populated as β-decay data [92] suggests that this state lies above the 3^-_1 state and both the possible decay paths, i.e., the $1^-_1 \rightarrow 2^+_1$ transition and the $1^-_1 \rightarrow 0^+_{\mathrm{g.s.}}$ transition, are not visible in the Coulex data. Therefore, the matrix elements connecting to the 1^-_1 state are completely switched off.

Thirdly, the branching ratio $\frac{\mathrm{Y}(3^- \rightarrow 4^+_1)}{\mathrm{Y}(3^- \rightarrow 2^+_1)}$ of 22 (15) % as determined in this work is used as additional data point.

The relative phase of E1 and E3 transitions is fixed to be positive, though a negative phase produces a comparable minimum and can not be ruled out. The sensitivity of Coulex as a method to this phase is lost due to the low statistics and scarce information on the transitions in question.

With these constraints the E3 matrix element describing the $3_1^- \rightarrow 2_1^+$ transition was determined.

7.4. Results and uncertainty discussion

The extracted reduced matrix elements are given in Table 7.2. For the other matrix elements, especially the matrix elements belonging to the γ band, the uncertainty was too high. Their best values are given in Table C.1. The high uncertainty stems from the fact, that only one transition for each of these cases is seen, with no signs of inband transitions. Furthermore, the transition energies in the band are such that they lie in ranges in the γ-ray spectrum that make a reliable background determination impossible.

The statistical uncertainty stems from the number of counts in the peaks per defined angular range. This uncertainty is governed by the background uncertainty for low-statistics transitions, while for high-statistics peaks, the with the efficiency calibration associated uncertainty of the order of 5-6 % has the biggest impact.

Besides the statistical uncertainties there are several sources of systematic uncertainties.

Some of these factors can be taken into account by explicitly varying them within their respective uncertainties. Others stem from the used approximations in the GOSIA code and need to be estimated as well.

The target thickness of 4 $\frac{\mathrm{mg}}{\mathrm{cm}^2}$ was varied by 5 %. This uncertainty is supposed to account for non-uniformities in the target thickness and density, which may also result from beam damage. Further to this, the determinability of energy loss of heavy ions in the target needs to be reflected. Between different codes that are usable to determine the stopping powers exist considerable discrepancies in the output. Some offsets are as high as 10 % of the respective calculated stopping power.

The beam energy was not explicitly measured for our experiment as the production target died too early. For other comparable campaigns at HIE-ISOLDE in 2016 a beam-energy measurement was done. In these a maximum deviation of 1 % from the requested beam energy was found with uncertainties in the measurement smaller than 0.5 % [58]. Thus, during the GOSIA investigation the beam energy was varied by 1 %.

The distance between target and forward detector was also varied by 5 %, even though the method used in Section 5.10.1 seems to be more sensitive than that. The cause for the bigger variation in GOSIA is the uncertainty of the beam energy, which is also incorporated here. Varying the distance affects the given ϑ ranges, which define the particle detector and the respective so-called experiments in the GOSIA input. These have a huge impact on the determined cross sections and therefore on the extracted matrix elements.

For the Doppler correction on the other hand, it is mandatory that the resolution of the peaks is improved as far as possible. This is done by extracting the angles of the MINIBALL array after setting the distance between FCD and target. Therefore, the Doppler correction of the γ-ray energies is less sensitive to the beam energy. The resulting changes of the MINIBALL angles have no measurable effect on the extracted matrix elements.

Table 7.2.: Extracted matrix elements in this work. Note, that the $2_1^+ \rightarrow 0_{\text{g.s.}}^+$ transition was used as normalization following [87]. The uncertainty given for this value is the full uncertainty. For more information see text.

Matrix element	Matrix element	Statistical uncertainty	Systematic uncertainty
M02	0.896 eb	*	0.042 eb
M24	1.35 eb	0.06 eb	0.10 eb
M46	1.84 eb	0.08 eb	0.13 eb
M68	2.2 eb	0.2 eb	0.2 eb
M22	-0.65 eb	0.60 eb	0.46 eb
M44	-2.1 eb	1.0 eb	0.9 eb
M66	-3.7 eb	1.2 eb	1.5 eb
M02g	0.18 eb	0.04 eb	0.01 eb
M22g	0.52 eb	0.10 eb	0.06 eb
M03	0.20 $\mathrm{eb}^{3/2}$	$^{0.14}_{0.10}\,\mathrm{eb}^{3/2}$	0.03 $\mathrm{eb}^{3/2}$

8. Discussion

The new partial low-energy low-spin level scheme for ^{142}Xe is shown in Figure 8.1. It shows the levels that were placed in the scope of this work, using information from both the Coulex data set and β-decay spectroscopy information [92]. The respective energies of the levels are indicated along with all observed transitions in the Coulex data. The γ-ray transitions only seen in β-decay spectroscopy are not shown. Also, the energy of the 1_1^- state candidate is not given, as it is not seen in the Coulex data. All new states are indicated in red. The assigned spins are based on systematic arguments.

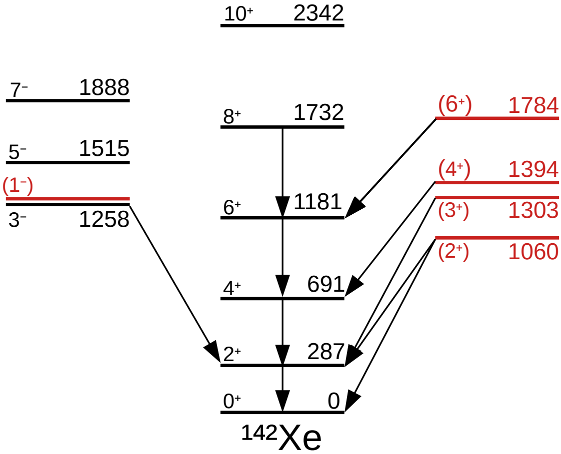

Figure 8.1.: Partial low-spin low-energy level scheme of ^{142}Xe. The level energies are given in keV. New states are indicated in red. The visible γ-ray transitions in the Coulex data are marked. For more details see text.

In Figure 8.2, the experimental level energies of the main band and the γ band are compared to Symmetry-Conserving Configuration-Mixing (SCCM) and Large Scale Shell Model (LSSM) calculations, performed by T. R. Rodríguez [109] and H. Naïdja [110], respectively. Before the comparison of experimental data and calculations, both approaches are outlined in the following.

For the LSSM calculations, the orbitals $1f_{7/2}$, $0h_{9/2}$, $1f_{5/2}$, $2p_{3/2}$, $2p_{3/2}$, $2p_{1/2}$, $0i_{13/2}$ and $0g_{7/2}$, $1d_{5/2}$, $1d_{3/2}$, $2s_{1/2}$, $0h_{11/2}$ for neutron and protons, respectively, span the model space above a closed ^{132}Sn core [111, 112]. The single-particle energies are fixed for both neutrons and protons using ^{133}Sn and ^{133}Sb experimental data [110].

For the diagonalization of the valence space, the shell-model codes ANTOINE and NATHAN [113, 114] were employed.

The effective interaction was based on the Chiral-effective field-theory potential N3LO [115]. The low-momentum potential V_{low-K} [116], accounting for the repulsive short-range core, was built from a smooth low-momentum potential, obtained via the integration of the nucleon-nucleon potential V_{NN} up to the cutoff momentum $\Lambda = 2.2\,\mathrm{fm}^{-1}$. The adaptation to the used model space is performed by many-body perturbation-theory techniques. See [111, 112] for further details.

Within the calculations, the E2 matrix elements were obtained utilizing the effective charges 0.6 e and 1.6 e for neutrons and protons, respectively, [110].

The SCCM method is a self-consistent beyond-mean-field approach. The calculations are performed using the finite-range Gogny-interaction in 1DS parameterization [117], which is based on the global properties of nuclear matter and can therefore be applied to nuclei on the entire nuclear chart.

In this method, final nuclear states are built as linear combinations from a mix of many-body states that possess distinct intrinsic parameters, e.g., deformation parameters. The required linear coefficients are calculated utilizing the generator coordinate method. With this method, intrinsic many-body states, i.e., generalized Slater determinants, are projected onto good quantum numbers to mix many-body states. The intrinsic many-body states are allowed to be both axially-symmetric and triaxial [118, 109].

In order to learn about the deformation of the states in a nucleus within this framework, the first step in the SCCM method is the evaluation of the mean-field energy as a function of the deformation (β, γ). In the present case, the particle-number projected energy is computed instead of the pure mean-field energy [109].

Similarly to the experimental results, the SCCM calculations show a rotational yrast band and a first excited γ band, although the spectrum is stretched with respect to the experimental data. This is a well-known effect in the present implementation of the SCCM method, where only static quadrupole (axial and triaxial) shapes have been considered to build the final nuclear states. Therefore, the ground state is variationally better explored than the excited states causing a larger energy gain for such a state. Including intrinsically rotating (cranking) configurations would help to deal with ground and excited-state energies on an almost equal footing from the variational point of view. This improvement of the SCCM method would produce a compression of the original theoretical spectrum and a better agreement with the experimental results. However, SCCM calculations with cranking are computationally expensive. In cases where the ground-state band has a rotational character, this compression can be mimicked by a constant factor because this compression can be interpreted by a modification of the moment of inertia of the deformed nucleus. If the main-band energies are multiplied by a factor 0.7, the agreement with the experimental data is much better [109].

The LSSM calculations [110] reproduce the experimental energies of the lowest-lying states for both the yrast and the γ band well.

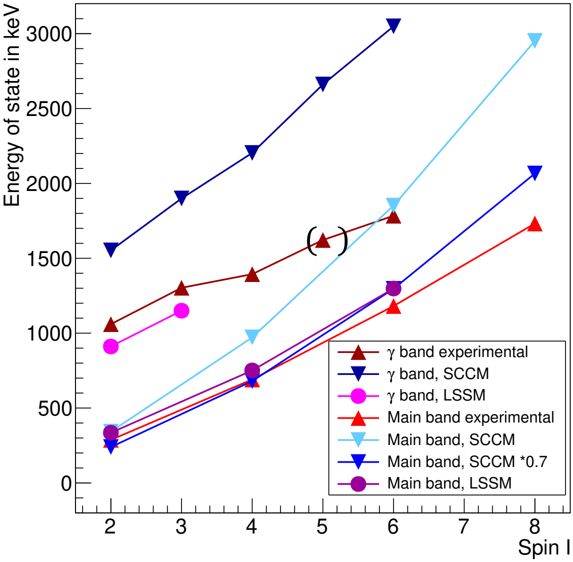

Figure 8.2.: Comparison of SCCM calculations [109], LSSM calculations [110], and experimental level energies for the main and the γ band in ^{142}Xe. The experimental values for the γ band were determined based on the data analyzed in the scope of this work and discussions with [92] analyzing β-decay data. A state at the energy of the 5^+_γ state is seen in fission data [89, 90], and is only placed based on systematics arguments in this work. For more details see text.

8.1. Collectivity and deformation in ^{142}Xe

In Table 8.1, the obtained B(Eσ;↓) values are given in single-particle units. The systematical uncertainties incorporate uncertainties that stem from approximations in GOSIA [41] and the ones discussed in the previous section. The statistical uncertainties describe uncertainties related to the number of counts and the background subtraction of the γ-ray spectra.

All reduced transition strengths of the main band are in the order of tens of W.u., indicating collective states. For the γ band, only the B(E2) values connecting to the head of the γ band, the first 2^+_γ state, are determined. This was done within the assumption of E2 transitions only. The collectivity of this state is lower than the one for the main band. The same is true for the 3^-_1 state, the determined uncertainty is dominated by the low statistics of the observed transition and lack of knowledge on the negative-parity band generally.

Table 8.1.: Reduced transition strengths B(Eσ;↓) in W.u. and spectroscopic quadrupole moments eQ$_s$ as obtained in this work. The B(E2) value for the $2^+_1 \rightarrow 0^+_{\text{g.s.}}$ transition was used as normalization and is taken from [87]. Uncertainties are denoted with statistical and systematical uncertainties.

I^π_i	I^π_f	$E_{\text{Level},i}$	E_γ	B(Eσ;↓) in W.u.	eQ$_s$(I^π_i) in eb
2^+_1	$0^+_{\text{g.s.}}$	287 keV	287 keV	36 (3)	-0.49 (45)$_{\text{stat.}}$ (35)$_{\text{sys.}}$
4^+_1	2^+_1	691 keV	404 keV	46 (4)$_{\text{stat.}}$ (7)$_{\text{sys.}}$	-0.71 (34)$_{\text{stat.}}$ (31)$_{\text{sys.}}$
6^+_1	4^+_1	1181 keV	490 keV	59 (5)$_{\text{stat.}}$ (9)$_{\text{sys.}}$	-1.02 (33)$_{\text{stat.}}$ (41)$_{\text{sys.}}$
8^+_1	6^+_1	1732 keV	551 keV	65 (12)$_{\text{stat.}}$ (12)$_{\text{sys.}}$	
2^+_γ	$0^+_{\text{g.s.}}$	1060 keV	1060 keV	1.5 (7)$_{\text{stat.}}$ (2)$_{\text{sys.}}$	
2^+_γ	2^+_1	1060 keV	773 keV	12 (5)$_{\text{stat.}}$ (3)$_{\text{sys.}}$	
3^-_1	$0^+_{\text{g.s.}}$	1259 keV	971 keV	5 (7)$_{\text{stat.}}$ (1)$_{\text{sys.}}$	

In Figure 8.3, the B(E2) values obtained in this work are shown in comparison to SCCM calculations [109], LSSM [110] calculations, and experimental lifetime measurement data [87]. The B(E2) value of the 2^+_1 state, calculated from this data [87], served as normalization for this work. The lifetime of the 4^+_1 state of the same campaign [87] is inconsistent with the Coulex data within the uncertainties. This inconsistency was also seen when analyzing REX-ISOLDE data, where both the 2^+_1 and the 4^+_1 state were populated [108].

The SCCM calculations [109] overestimate the B(E2) value for the same transition by 28 (20) %, while the LSSM calculations [110] reproduce the experimental value of this work. The other determined B(E2) values belonging to the other main-band transitions are in agreement with both SCCM and LSSM calculation.

For the 2^+_γ state, which is the lowest-lying member of the γ band, the experimental reduced transition strengths were extracted under the assumption that these transitions are governed by E2 transitions only. For the LSSM and SCCM calculations, only the B(E2) part is shown in this plot. The B(E2; $0^+_{\text{g.s.}} \rightarrow 2^+_\gamma$) value is shown on the left and the B(E2; $2^+_1 \rightarrow 2^+_\gamma$) value is shown on the right. The LSSM calculations agree with the experimental data, but the SCCM calculations overestimate the B(E2; $0^+_{\text{g.s.}} \rightarrow 2^+_\gamma$) value, while the B(E2; $2^+_1 \rightarrow 2^+_\gamma$) value is in agreement with the experimental Coulex data.

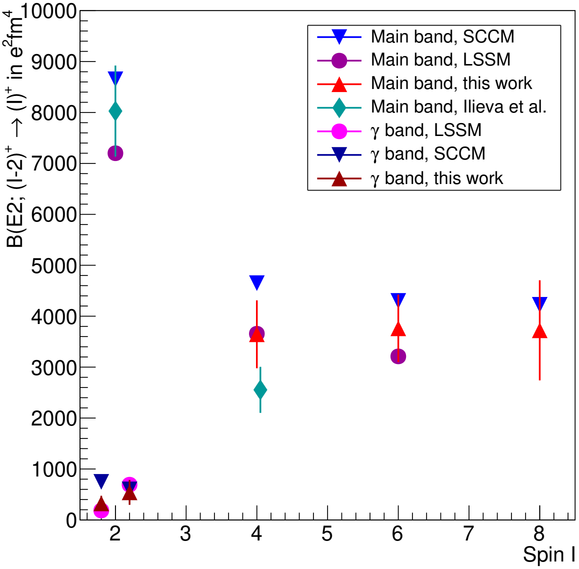

Figure 8.3.: Comparison of SCCM calculations [109], LSSM calculations [110], and experimental B(E2↑) values for the main band and the transitions to the 2^+_γ state. The lifetime of the 2^+_1 state given in the work by S. Ilieva et al. [87] is used as normalization in this work. The reduced transition strengths connecting to the 2^+_γ state are understood as showing the value for the $0^+_{\text{g.s.}} \rightarrow 2^+_\gamma$ transition on the left and the $2^+_1 \rightarrow 2^+_\gamma$ transition on the right, considering E2 transitions, only. For more details see text.

In Figure 8.4, the spectroscopic quadrupole moments as determined in this work are shown together with a comparison to SCCM [109] and LSSM [110] calculations. The theoretical and experimental values agree within their uncertainties. The fact that the spectroscopic quadrupole moments are negative indicates that the yrast-band states are prolate.

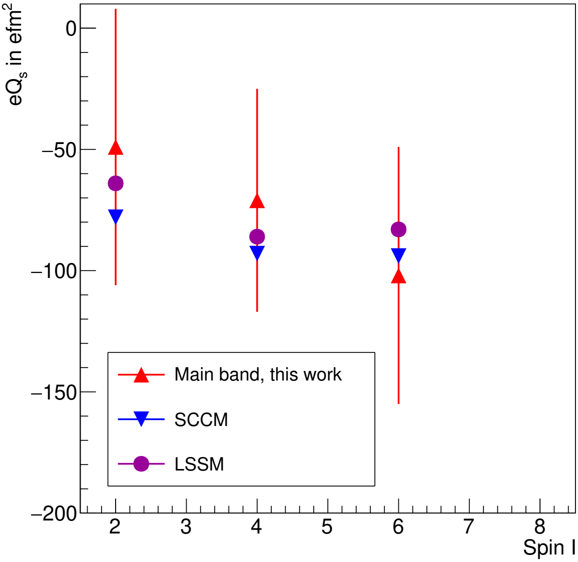

Figure 8.4.: Comparison of SCCM calculations [109], LSSM calculations [110], and experimental spectroscopic-quadrupole moments for the main band. The experimental values are obtained in this work. For more details see text.

Figure 8.5 shows the collective wave functions for the yrast band and the γ band of ^{142}Xe calculated via SCCM by [109]. These collective wave functions represent the weights of the various intrinsic deformations in each individual nuclear state. The yrast-band states exhibit an axial prolate shape. The shape of the γ-band states is a triaxial ellipsoid.

The collective wave functions were calculated for the isotopes ^{138}Xe and ^{140}Xe as well, showing a maximum close to the axial prolate state. The trend is that ^{138}Xe is almost spherical, and ^{142}Xe being the most deformed in β, while ^{140}Xe lies in between the two. Consistently, the reduced transition strengths and spectroscopic quadrupole moments increase from the less deformed ^{138}Xe to the more deformed ^{142}Xe [109].

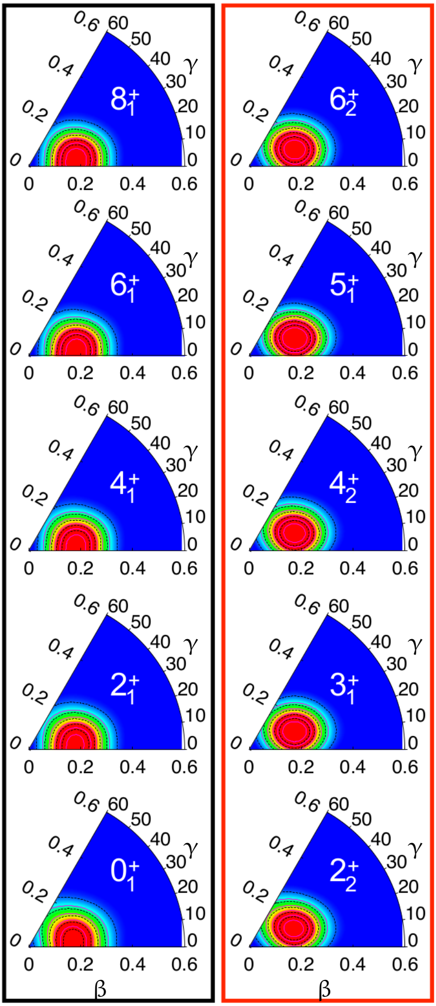

Figure 8.5.: Collective wave functions of the yrast band and the γ band in ^{142}Xe [109]. The yrast band is marked in black on the left, and the γ band is marked in red on the right. Note that the yrast-band states exhibit an axial prolate shape, while the γ-band states form a triaxial ellipsoid.

8.2. Octupole collectivity in ^{142}Xe

One main motivation for the investigation of this nucleus at the given energy was to determine whether the enhancement of octupole collectivity at N = 88 goes as far down as xenon.

Generally, octupole correlations depend on the spacing in between single-particle states with $\Delta j = \Delta l = 3$, and on the matrix elements of the related spherical harmonics. For the proton and neutron numbers $\approx$ 34, 56, 88, and 134, the spacing is small, and the states approach the Fermi surface [8].

^{142}Xe lies just below the proton number 56, where a coupling of the $h_{11/2}$ shell with the $d_{5/2}$ shell is expected to enhance octupole collectivity. Furthermore, ^{142}Xe has 88 neutrons, where the same is true for the $i_{13/2}$ shell and the $f_{7/2}$ shell [7].

Comparing the in this work obtained $B(E3;\, 3^-_1 \rightarrow 0^+_{\mathrm{g.s.}})$ value of ^{142}Xe, 5 (7) W.u., to the $48\,^{+25}_{-34}$ W.u. for ^{144}Ba [6], indicates that the two values are consistent, especially considering the large uncertainties.

The B(E3;↓) value calculated following the systematics as given in [119] is with 2.7 (8) W.u. comparable to the one determined from the Coulex data in this work. Due to the large uncertainties of the obtained B(E3) value, the question of whether ^{142}Xe shows enhanced octupole collectivity cannot be decided conclusively. Nevertheless, a value as large as the one reported for ^{144}Ba [6] can be excluded.

When thinking about octupole collectivity it is also instructive to consider the location of the first 1^-_1 state.

In spherical, vibrator-like even-even nuclei, the lowest excitations are mostly quadrupole and octupole vibrations. In such nuclei, harmonic coupling of quadrupole-octupole phonons leads to a multiplet consisting of five states that is expected at the energy $E(2^+_1) + E(3^-_1)$ [120].

With the onset of quadrupole-octupole deformation, the energy of the 1^- state starts being lower. A static quadrupole deformation together with the octupole phonon allows to create four bands with K = 0, 1, 2, 3, thus allowing two 1^- states. These states can possess a dynamic dipole moment, which is equal to a separation of center of charge and center of mass, and decay via E1 transitions.

In ^{142}Xe, the 1^- state candidate lies slightly above the 3^- state, just like in ^{142}Ba and unlike in ^{144}Ba.

8.3. Branching ratios for γ bands in ^{140}Xe and ^{142}Xe

In Table 8.2, the γ-ray energies and branching ratios of the transitions depopulating the known states in the γ band of ^{140}Xe [97] are compared to their respective counterparts in ^{142}Xe as obtained from this work. Additionally, the expected branchings for ^{142}Xe according to the Alaga rule [121], and the ones calculated from SCCM [109], are presented.

Table 8.2.: Comparison of relative intensities $I_{rel.}$ of transitions depopulating γ-band states in ^{142}Xe as obtained in this work and in the neighboring ^{140}Xe as given in [97]. Intensities are denoted relative to the strongest decay path. Comparison to relative intensities following the Alaga rules [121] and SCCM calculations including M1 transitions [109] are given for ^{142}Xe.

		^{140}Xe		^{142}Xe	This work	SCCM	Alaga
J_i^π	J_f^π	E_γ	$I_{rel.}$	E_γ	$I_{rel.}$	$I_{rel.}$	$I_{rel.}$
6_γ^+	6_1^+	309 keV	1.0	603 keV	1.0	1.0	0.2
	4_1^+	891 keV	0.8	1093 keV	< 0.5	0.26	1.0
5_γ^+	6_1^+	156 keV	0.03				
	3_γ^+	269 keV	0.08				
	4_1^+	739 keV	1.0				
4_γ^+	4_1^+			703 keV	1.0	1.0	0.3
	2_1^+			1107 keV	0.04 (2)	0.41	1.0
3_γ^+	4_1^+	470 keV	0.3	612 keV	< 0.7	0.11	0.03
	2_1^+	928 keV	1.0	1016 keV	1.0	1.0	1.0
2_γ^+	2_1^+			773 keV	1.0	1.0	0.3
	$0_{\text{g.s.}}^+$			1060 keV	0.57 (6)	0.86	1.0

While the 2_γ^+ and 4_γ^+ states of ^{140}Xe are not sufficiently populated in the spontaneous fission of ^{248}Cm [97], for Coulomb excitation at a beam energy of 4.5 MeV/u, the 5_γ^+ state was not seen and anything beyond the 6_γ^+ state candidate not populated.

In both nuclei, the dominant decay path for the 6_γ^+ state is the $6_\gamma^+ \rightarrow 6_1^+$ transition, with the $6_\gamma^+ \rightarrow 4_1^+$ transition being weaker. This finding is the main argument for the assignment of spin 6 as opposed to 5 to the found 6_γ^+ state candidate. Considering the decay paths in ^{140}Xe, the predominant transition depopulating the 5_γ^+ state is the transition to the first 4^+ state of the main band, by a significant margin. Such a transition is not visible in ^{142}Xe with the particle-$\gamma\gamma$ coincidences suggesting a transition to the 6_1^+ state.

Further to this, the ratio $\frac{Y(5_\gamma^+ \rightarrow 4_1^+)}{Y(2_1^+ \rightarrow 0_{\text{g.s.}}^+)}$, at 11 %, is fairly high in ^{140}Xe, while none of the other γ-band transitions exhibit a similiar strength [97]. For both the spontaneous fission of ^{252}Cf [89] and ^{248}Cm [90], a γ-ray transition with an energy of 931 keV feeding the 4_1^+ state of ^{142}Xe is observed. The corresponding state energy, at 1622 keV, lies in between the energies of the 4_γ^+ state and 6_γ^+ state, which reside at 1394 keV and 1784 keV, respectively. Considering the strength of the $5_\gamma^+ \rightarrow 4_1^+$ transition measured in the neighboring ^{140}Xe employing the same method, this level is a candidate for the 5^+_γ state in ^{142}Xe.

The other directly comparable state, as seen for both ^{140}Xe and ^{142}Xe, is the 3^+_γ state. Here, the dominant decay path for both nuclei is the $3^+_\gamma \rightarrow 2^+_1$ transition, while the corresponding $3^+_\gamma \rightarrow 4^+_1$ transition is weaker. Note that the actual intensity is quite likely lower than the given upper limit for the $3^+_\gamma \rightarrow 4^+_1$ transition, as the $10^+_1 \rightarrow 8^+_1$ main-band transition at 610 keV may enhance the determined limit. A more exact value can be expected from β-decay spectroscopy, where the population of the 10^+_1 state is impossible [92].

Regarding the γ-ray transitions depopulating the 2^+_γ and 4^+_γ states in ^{142}Xe, no comparison to the transitions in ^{140}Xe is possible, as these states are not reported for this nucleus. Nevertheless, the trend of a predominant decay via same-spin γ-ray transitions continues for these states.

A comparison of the experimental branching ratios in ^{142}Xe as obtained in this work to SCCM calculations [109], which also incorporate M1 transitions, shows a reproduction of the same trend. Same-spin transitions predominate.

On the other hand, comparing the branching ratios in ^{142}Xe to the Alaga intensity rules for transitions to rotational states in strongly-deformed nuclei [121], even though not fully applicable to this case, reveals that for pure E2 transitions, the stretched E2 transitions $(I)^+_\gamma \rightarrow (I-2)^+_1$ should dominate over the same spin transitions from the γ band to the main band. The Alaga rules employ angular momentum considerations only, which, while clearly an insufficient approach for the present nucleus, show a discrepancy between prediction and experimental evidence suggesting a mixing between yrast and γ band. This also allows M1 transitions, which would be forbidden if K was a good quantum number.

This is reflected in the results of the SCCM and LSSM calculations predicting non-zero M1 transition strengths for the higher-lying members of the γ band.

Coming back to the experimental findings, the branching ratios of the two neighboring nuclei ^{140}Xe and ^{142}Xe are consistent, suggesting structural similiarities between the two isotopes.

This interpretation is not supported when considering the information gained in β-decay measurements for ^{140}Xe [122] compared to β-decay measurements for ^{142}Xe [92]. The ground state of the mother nucleus ^{140}I is determined to be a 4^- state [122] unlike the 2^- state in ^{142}I [92]. Consistently, the low-lying members of the γ band were not populated in the decay of ^{140}I contrary to the decay of ^{142}I. This fact was crucial for the identification of the 3^+_γ state in ^{142}Xe.

Additionally, fission experiments highlight the differences between the two nuclei. In ^{140}Xe, the γ band is populated, and even the 3^+_γ state is reported [97]. In ^{142}Xe, on the other hand, no hints of the low-lying states of the γ band are seen in neutron-induced prompt fission of ^{235}U and ^{241}Pu [87], neither in neutron-induced fission of ^{238}U using νball [123], nor spontaneous fission of ^{252}Cf [89] and ^{248}Cm [90, 9].

Further to this, the collective wave functions, calculated by means of SCCM [109], suggest that the ground-state band of the nucleus ^{140}Xe is different to that in ^{142}Xe. The maximum of the collective wave function for ^{140}Xe lies at a γ of about 10$\,^\circ$, while this value is equal to zero for ^{142}Xe, as it is for ^{138}Xe [109].

In summary, the two nuclei ^{140}Xe and ^{142}Xe exhibit some properties that are similar, following a smooth trend from ^{138}Xe to ^{142}Xe, while other characteristics are quite distinct.

9. Summary and outlook

The main motivation and challenge of the data analysis in this work was a rich number of observed transitions combined with little information available in literature. Along with the low statistics of the transitions in question, some quantities could not be determined, while a consistent level scheme was created.

The determined reduced transition strengths for the main band up to the 8_1^+ state are in the order of several tens of W.u., indicating collective states. According to the analysis in the present work, the same states possess negative spectroscopic quadrupole moments illustrating a prolate shape. The novel observation of the γ band is a further clarification of the low-lying structure of this nucleus.

All these findings are consistent with SCCM [109] and LSSM [110] calculations.

A property that has not been but can be evaluated from this data set, is the g-factor of the first 2^+ state. Discussions with experts of the method have shown that the statistics in the $2_1^+ \rightarrow 0_{\text{g.s.}}^+$ transition should be sufficient.

As the lifetime of the first 2^+ state combined with the lifetime of the first 4^+ state [87] is inconsistent with the Coulex data, it would be instructive to determine the lifetimes from other data. Especially the B(E2; $4_1^+ \rightarrow 2_1^+$) value remains an interesting candidate for further investigation. Not only do the two experimental values disagree, but the calculated SCCM value also shows a deviation which does not appear for the other transitions.

Furthermore, observations from this work have already lead to fruitful discussions with the group analyzing β-decay spectroscopy data of ^{142}I [92]. Their final results will shed additional light on the decay branches of both the low-lying states in the γ band and the negative-parity band. This may allow for better determination of reduced transition strengths and possibly spectroscopic quadrupole moments of the participating states utilizing this Coulex data set.

These quantities are crucial in gaining a better understanding of the shape and collectivity of the nucleus. Both SCCM and LSSM calculations predict a positive spectroscopic quadrupole moment for the head of the γ band, suggesting an oblate shape for the 2_γ^+ state. The 3_γ^+ state is calculated to be almost spherical [109, 110], while the 4_γ^+ state and those beyond are expected to be prolate like the main-band states [109]. Therefore, robust branching ratios for the relevant transitions are essential to verify these predictions and hereby the applied theoretical approaches.

Moreover, SCCM calculations suggest a considerable influence of M1 transitions in the deexcitation of the higher-lying γ-band members, though this influence vanishes for the

$2^+_\gamma \rightarrow 2^+_1$ transition [109].

Unfortunately, the determination of M1/E2 mixing ratios in the decay of the γ band was not possible utilizing the present data due to the low statistics of the transitions in question. In addition, the $2^+_\gamma \rightarrow 2^+_1$ transition, having the highest intensity of the transitions depopulating the γ band, lies on top of the smeared ^{206}Pb target transition further complicating the analysis.

In order to determine these properties, higher statistics would be necessary, mandating either a longer experimental campaign or a higher beam intensity. An increase of the beam energy alone would not help due to the limitations of "safe" Coulex. Coulomb excitation cross sections are maximized when approaching the maximum "safe" bombarding energy, beyond which Coulomb-nuclear interferences are destructive.

A measurement using a ^{208}Pb target could circumvent the difficulties arising from the smeared target structure in the vicinity of some of the newly observed transitions, as no γ-ray transitions are expected from this nucleus within this energy range. Additionally, a thinner target could increase the resolution of the peaks, improving clarity for the weaker transitions, but requiring a higher-intensity beam. Generally, performing the experiment with a second target is always desirable, as a distinct reaction partner provides valuable information for the GOSIA analysis.

The low-lying structure of the nuclei with two additional protons, ^{142}Ba and ^{144}Ba, has also been investigated in a Coulomb excitation campaign at HIE-ISOLDE. There appear to be considerable differences between the structure of ^{142}Xe and ^{144}Ba, especially in terms of octupole collectivity. ^{142}Ba, on the other hand, shows a more similar behavior as for this nucleus the 1^- state seems to lie slightly above the 3^- state as well. Once the data is published, a comparison of these barium nuclei with ^{142}Xe will be informative.

It is instructive to consider which information on the neutron-rich xenon isotopes could be obtained from what kind of experiment. The lowest-lying structure is, unsurprisingly, best investigated using Coulex, while the high-lying states are accessible using fission spectroscopy [89, 9]. β-decay spectroscopy seems to be a crucial tool in bringing both these data sets together. This is especially true as the low-lying part of the octupole band is insufficiently populated in fission experiments, and the γ band has not been seen for ^{142}Xe in fission data so far.

For the even-even neighbor ^{140}Xe, the lowest-lying states of the γ band are unknown, while the higher-lying states have already been seen in fission data [97]. Beta-decay measurements [122] have not succeeded in populating the low-lying states either, so, for the investigation of this nucleus, Coulomb excitation would be as perfect a tool as for ^{142}Xe. The clarification of the low-lying structure would help to expand the knowledge of both quadrupole and octupole collectivity in the region.

The same is true for the even-even isotope ^{144}Xe, though at present no facility is available that can provide this rare isotope as a beam with sufficient intensity to determine the properties of any possible side band. At ISOLDE, for example, the yield of this isotope is ten to thirty times lower than for ^{142}Xe. Information on this nucleus is generally very scarce, making it an interesting nucleus to investigate.

A. Coulex kinematics

This chapter provides various equations that were used during the analysis to reconstruct angles and energies based on given information from the detected particles. Note that all considerations here are true when considering the laboratory frame and not the center of mass frame.

The first set allows for the determination of the energy of a detected particle with mass number A by taking its θ angle into consideration. The energy of the projectile E_p is then

$$\begin{aligned} E_p = a_1 \left(\frac{A_t}{A_p + A_t} \right)^2 \Bigg[1 + a_2 \left(\frac{A_p}{A_t} \right)^2 \\ + 2\sqrt{a_2} \cdot \frac{A_p}{A_t} \cdot \cos\left(\theta_p + \arcsin\left(\sqrt{a_2} \cdot \frac{A_p}{A_t} \cdot \sin(\theta_p) \right) \right) \Bigg] \; . \end{aligned} \tag{A.1}$$

The energy of the target E_t is computable using

$$\begin{aligned} E_t = a_1 \frac{A_p A_t}{(A_p + A_t)^2} \Bigg[1 + a_2 + 2\sqrt{a_2} \\ \cdot \cos\left(\theta_t + \sin\left(\sqrt{\frac{A_p A_t E_{\text{beam}}}{A_p A_t E_{\text{beam}} - \Delta E (A_p + A_t)}} \cdot \sin(\theta_t) \right) \right) \Bigg] \; . \end{aligned} \tag{A.2}$$

The functions a_1 and a_2 are defined in the following.

$$\begin{aligned} a_1 &= A_p E_{\text{beam}} - \Delta E \left(1 + \frac{A_p}{A_t} \right) \; , \\ a_2 &= \frac{A_p E_{\text{beam}}}{a_1} \; . \end{aligned} \tag{A.3}$$

If the other reaction partner was not detected, its angle needs to be reconstructed using the spatial information of the detected particle.

$$\theta_t = \arccos\left(\frac{p_0^2 + p_p - 2A_p^2 E_{\text{beam}} - A_p^2 E_{\text{beam}}^2 + 2A_p E_{\text{rec}} + 2E_{\text{beam}} A_p E_{\text{rec}} - E_{\text{rec}}^2}{2p_0 p_p} \right) \; . \tag{A.4}$$

$$\theta_p = \arccos\left(\frac{p_0^2 - p_t^2 + p_p^2}{2p_0 p_p} \right) \tag{A.5}$$

The following definitions are used:

$$\begin{aligned}
p_0 &= \sqrt{E_{\text{beam}}^2 A_p^2 + 2E_{\text{beam}} A_p^2} \\
p_t &= \sqrt{(E_{\text{beam}} A_p - E_{\text{part}} - \Delta E)^2 + 2A_p (E_{\text{beam}} A_p - E_{\text{part}} - \Delta E)} \\
p_p &= \sqrt{E_{\text{rec}}^2 + 2A_t E_{\text{rec}}} \\
E_{\text{rec}} &= E_{\text{beam}} A_p - E_{\text{part}} - \Delta E \ .
\end{aligned} \tag{A.6}$$

B. Doppler correction of ^{196}Pt target spectrum

In the very beginning of the actual data collection the 1.4 $\frac{\mathrm{mg}}{\mathrm{cm}^2}$ thick platinum target was used.

The statistics obtained with this target are shown in Figure B.1. Note, that this is a near-online γ-ray energy-spectrum Doppler corrected with respect to the target. Thus, the transitions originating from the excitation of the ^{142}Xe beam appear as smeared structures in the spectrum. On the low-energy side the Kα and Kβ X-rays of platinum are visible at their expected energies. The most prominent transitions stem from the two even-even isotopes ^{194}Pt and ^{196}Pt. Both energetically lowest lying transitions, i.e., the $2_1^+ \rightarrow 0_{\mathrm{g.s.}}^+$ and $4_1^+ \rightarrow 2_1^+$ transitions, of these nuclei are clearly visible. For the case of ^{195}Pt, a nucleus with an odd number of neutrons, the excitation probability is spread over multiple transitions, of which only the strongest ones are marked here.

Considering the strength of each of the transitions, the interpretation is that this target was in fact closer to natural platinum as opposed to the assumed pure ^{196}Pt target[1].

---

[1] The most abundant isotopes in natural platinum are: ^{194}Pt with 33 %, ^{195}Pt with 34 %, ^{196}Pt with 25 % and ^{198}Pt with 7 % [124].

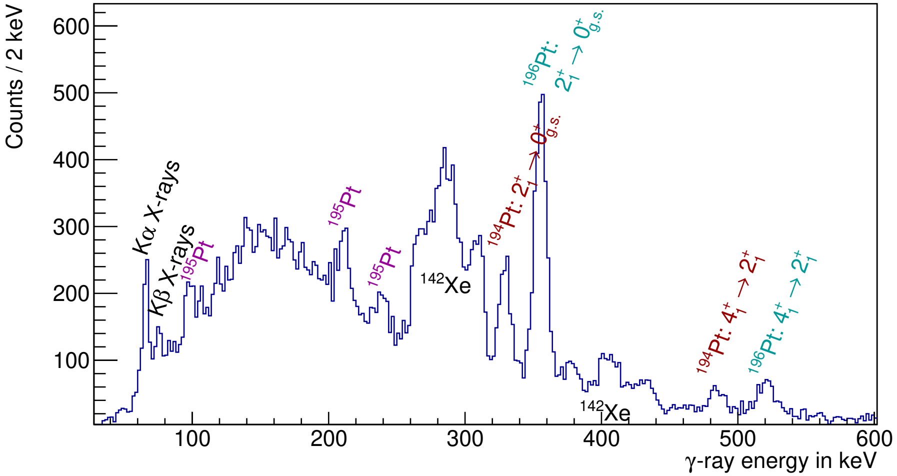

Figure B.1.: Online γ-ray energy-spectrum obtained with the platinum target. Doppler-corrected with respect to the target. Note, that all of the most abundant isotopes of natural platinum are visible. The xenon peaks appear smeared as they are wrongly corrected.

C. Gosia input

Table C.1 shows the best values of matrix elements, for which the uncertainty as determined in the GOSIA analysis is too high to give reliable error bars. Tables C.2, C.3, C.4, C.5, and C.6 show the efficiency-corrected yields for each of the transitions including their uncertainties. They were used as input for the GOSIA calculations.

Table C.1.: Best values for matrix elements with more than 100 % uncertainty as determined in the GOSIA analysis. Note that the given precision is arbitrary.

Matrix element	Transition	Best value
M_{23g}	$2_1^+ \rightarrow 3_\gamma^+$	-0.53 eb
M_{24g}	$2_1^+ \rightarrow 4_\gamma^+$	-0.07 eb
M_{42g}	$4_1^+ \rightarrow 2_\gamma^+$	-0.44 eb
M_{43g}	$4_1^+ \rightarrow 3_\gamma^+$	-0.04 eb
M_{44g}	$4_1^+ \rightarrow 4_\gamma^+$	1.17 eb
M_{64g}	$6_1^+ \rightarrow 4_\gamma^+$	-0.02 eb
M_{88}	$8_1^+ \rightarrow 8_1^+$	-5.44 eb
M_{2g2g}	$2_\gamma^+ \rightarrow 2_\gamma^+$	-0.64 eb
M_{2g3g}	$2_\gamma^+ \rightarrow 3_\gamma^+$	0.98 eb
M_{2g4g}	$2_\gamma^+ \rightarrow 4_\gamma^+$	1.14 eb
M_{3g3g}	$3_\gamma^+ \rightarrow 3_\gamma^+$	1.63 eb
M_{3g4g}	$3_\gamma^+ \rightarrow 4_\gamma^+$	-2.02 eb
M_{4g4g}	$4_\gamma^+ \rightarrow 4_\gamma^+$	-4.74 eb
M_{3-3-}	$3^- \rightarrow 3^-$	0.50 eb

Table C.2.: γ-ray yields for the different angular experiments defined in Table 7.1. Background subtracted and efficiency corrected. Part 1.

Range number	Transition	γ-ray energy	Counts
1	$4^+_\gamma \rightarrow 4^+_1$	703 keV	165 (51)
	$2^+_\gamma \rightarrow 2^+_1$	773 keV	340 (63)
	$2^+_\gamma \rightarrow 0^+_{\mathrm{g.s.}}$	1060 keV	172 (33)
	$8^+_1 \rightarrow 6^+_1$	551 keV	138 (35)
	$6^+_1 \rightarrow 4^+_1$	490 keV	1005 (74)
	$4^+_1 \rightarrow 2^+_1$	404 keV	4063 (239)
	$2^+_1 \rightarrow 0^+_{\mathrm{g.s.}}$	287 keV	9055 (476)
2	$4^+_\gamma \rightarrow 4^+_1$	703 keV	111 (50)
	$2^+_\gamma \rightarrow 2^+_1$	773 keV	281 (59)
	$2^+_\gamma \rightarrow 0^+_{\mathrm{g.s.}}$	1060 keV	135 (30)
	$8^+_1 \rightarrow 6^+_1$	551 keV	126 (28)
	$6^+_1 \rightarrow 4^+_1$	490 keV	736 (66)
	$4^+_1 \rightarrow 2^+_1$	404 keV	3364 (200)
	$2^+_1 \rightarrow 0^+_{\mathrm{g.s.}}$	287 keV	8230 (436)

Table C.3.: γ-ray yields for the different angular experiments defined in Table 7.1. Background subtracted and efficiency corrected. Part 2.

Range number	Transition	γ-ray energy	Counts
3	$4_\gamma^+ \rightarrow 4_1^+$	703 keV	111 (50)
	$2_\gamma^+ \rightarrow 2_1^+$	773 keV	273 (56)
	$2_\gamma^+ \rightarrow 0_{\text{g.s.}}^+$	1060 keV	155 (25)
	$8_1^+ \rightarrow 6_1^+$	551 keV	99 (27)
	$6_1^+ \rightarrow 4_1^+$	490 keV	740 (67)
	$4_1^+ \rightarrow 2_1^+$	404 keV	3507 (208)
	$2_1^+ \rightarrow 0_{\text{g.s.}}^+$	287 keV	9224 (485)
4	$4_\gamma^+ \rightarrow 4_1^+$	703 keV	133 (51)
	$2_\gamma^+ \rightarrow 2_1^+$	773 keV	325 (68)
	$2_\gamma^+ \rightarrow 0_{\text{g.s.}}^+$	1060 keV	192 (29)
	$8_1^+ \rightarrow 6_1^+$	551 keV	74 (28)
	$6_1^+ \rightarrow 4_1^+$	490 keV	808 (72)
	$4_1^+ \rightarrow 2_1^+$	404 keV	4243 (249)
	$2_1^+ \rightarrow 0_{\text{g.s.}}^+$	287 keV	12777 (666)
5	$4_\gamma^+ \rightarrow 4_1^+$	703 keV	182 (61)
	$2_\gamma^+ \rightarrow 2_1^+$	773 keV	502 (92)
	$2_\gamma^+ \rightarrow 0_{\text{g.s.}}^+$	1060 keV	326 (40)
	$8_1^+ \rightarrow 6_1^+$	551 keV	89 (34)
	$6_1^+ \rightarrow 4_1^+$	490 keV	862 (81)
	$4_1^+ \rightarrow 2_1^+$	404 keV	5853 (338)
	$2_1^+ \rightarrow 0_{\text{g.s.}}^+$	287 keV	21521 (1113)

Table C.4.: γ-ray yields for the different angular experiments defined in Table 7.1. Background subtracted and efficiency corrected. Part 3.

Range number	Transition	γ-ray energy	Counts
6	$4_\gamma^+ \to 4_1^+$	703 keV	113 (51)
	$2_\gamma^+ \to 2_1^+$	773 keV	499 (146)
	$2_\gamma^+ \to 0_{\text{g.s.}}^+$	1060 keV	335 (55)
	$8_1^+ \to 6_1^+$	551 keV	62 (36)
	$6_1^+ \to 4_1^+$	490 keV	716 (77)
	$4_1^+ \to 2_1^+$	404 keV	5510 (320)
	$2_1^+ \to 0_{\text{g.s.}}^+$	287 keV	25904 (1337)
7	$2_\gamma^+ \to 2_1^+$	773 keV	271 (70)
	$2_\gamma^+ \to 0_{\text{g.s.}}^+$	1060 keV	176 (29)
	$6_1^+ \to 4_1^+$	490 keV	256 (35)
	$4_1^+ \to 2_1^+$	404 keV	2525 (154)
	$2_1^+ \to 0_{\text{g.s.}}^+$	287 keV	14558 (758)
8	$2_\gamma^+ \to 2_1^+$	773 keV	210 (75)
	$2_\gamma^+ \to 0_{\text{g.s.}}^+$	1060 keV	121 (28)
	$6_1^+ \to 4_1^+$	490 keV	261 (36)
	$4_1^+ \to 2_1^+$	404 keV	2437 (150)
	$2_1^+ \to 0_{\text{g.s.}}^+$	287 keV	14859 (773)
9	$2_\gamma^+ \to 2_1^+$	773 keV	243 (96)
	$2_\gamma^+ \to 0_{\text{g.s.}}^+$	1060 keV	144 (28)
	$6_1^+ \to 4_1^+$	490 keV	165 (35)
	$4_1^+ \to 2_1^+$	404 keV	2135 (136)
	$2_1^+ \to 0_{\text{g.s.}}^+$	287 keV	15735 (818)

Table C.5.: γ-ray yields for the different angular experiments defined in Table 7.1. Background subtracted and efficiency corrected. Part 4.

Range number	Transition	γ-ray energy	Counts
10	$2^+_\gamma \rightarrow 2^+_1$	773 keV	363 (161)
	$2^+_\gamma \rightarrow 0^+_{\text{g.s.}}$	1060 keV	184 (35)
	$6^+_1 \rightarrow 4^+_1$	490 keV	205 (44)
	$4^+_1 \rightarrow 2^+_1$	404 keV	2706 (169)
	$2^+_1 \rightarrow 0^+_{\text{g.s.}}$	287 keV	23967 (1238)
11	$2^+_\gamma \rightarrow 2^+_1$	773 keV	282 (128)
	$2^+_\gamma \rightarrow 0^+_{\text{g.s.}}$	1060 keV	142 (33)
	$6^+_1 \rightarrow 4^+_1$	490 keV	75 (39)
	$4^+_1 \rightarrow 2^+_1$	404 keV	1843 (121)
	$2^+_1 \rightarrow 0^+_{\text{g.s.}}$	287 keV	20607 (1067)
12	$2^+_\gamma \rightarrow 2^+_1$	773 keV	100 (41)
	$2^+_\gamma \rightarrow 0^+_{\text{g.s.}}$	1060 keV	53 (25)
	$6^+_1 \rightarrow 4^+_1$	490 keV	48 (28)
	$4^+_1 \rightarrow 2^+_1$	404 keV	613 (54)
	$2^+_1 \rightarrow 0^+_{\text{g.s.}}$	287 keV	10094 (529)
13	$3^- \rightarrow 2^+_1$	971 keV	104 (80)
	$4^+_\gamma \rightarrow 4^+_1$	703 keV	91 (41)
	$3^+_\gamma \rightarrow 2^+_1$	1016 keV	113 (49)
	$2^+_\gamma \rightarrow 2^+_1$	773 keV	1526 (133)
	$2^+_\gamma \rightarrow 0^+_{\text{g.s.}}$	1060 keV	850 (89)
	$6^+_1 \rightarrow 4^+_1$	490 keV	1229 (106)
	$4^+_1 \rightarrow 2^+_1$	404 keV	13169 (744)
	$2^+_1 \rightarrow 0^+_{\text{g.s.}}$	287 keV	83664 (4348)

Table C.6.: γ-ray yields for the different angular experiments defined in Table 7.1. Background subtracted and efficiency corrected. Part 5.

Range number	Transition	γ-ray energy	Counts
14	$3^- \rightarrow 2_1^+$	971 keV	81 (50)
	$4_\gamma^+ \rightarrow 4_1^+$	703 keV	334 (45)
	$3_\gamma^+ \rightarrow 2_1^+$	1016 keV	39 (33)
	$2_\gamma^+ \rightarrow 2_1^+$	773 keV	1460 (130)
	$2_\gamma^+ \rightarrow 0_{\text{g.s.}}^+$	1060 keV	735 (74)
	$8_1^+ \rightarrow 6_1^+$	551 keV	410 (67)
	$6_1^+ \rightarrow 4_1^+$	490 keV	2873 (187)
	$4_1^+ \rightarrow 2_1^+$	404 keV	15550 (873)
	$2_1^+ \rightarrow 0_{\text{g.s.}}^+$	287 keV	47139 (2421)
15	$6_\gamma^+ \rightarrow 6_1^+$	603 keV	96 (50)
	$4_\gamma^+ \rightarrow 4_1^+$	703 keV	134 (50)
	$2_\gamma^+ \rightarrow 2_1^+$	773 keV	190 (100)
	$2_\gamma^+ \rightarrow 0_{\text{g.s.}}^+$	1060 keV	146 (30)
	$6_1^+ \rightarrow 4_1^+$	490 keV	1110 (84)
	$4_1^+ \rightarrow 2_1^+$	404 keV	2378 (156)
	$2_1^+ \rightarrow 0_{\text{g.s.}}^+$	287 keV	3434 (241)
16	$6_\gamma^+ \rightarrow 6_1^+$	603 keV	5 (5)
	$4_\gamma^+ \rightarrow 4_1^+$	703 keV	9 (9)
	$2_\gamma^+ \rightarrow 2_1^+$	773 keV	34 (20)
	$2_\gamma^+ \rightarrow 0_{\text{g.s.}}^+$	1060 keV	20 (7)
	$6_1^+ \rightarrow 4_1^+$	490 keV	109 (16)
	$4_1^+ \rightarrow 2_1^+$	404 keV	213 (22)
	$2_1^+ \rightarrow 0_{\text{g.s.}}^+$	287 keV	395 (27)

Acknowledgements

In the first place, I would like to thank my supervisor, Thorsten Kröll, for having given me the opportunity to work on my doctoral thesis in his group, for his advice, and support over the last years.

Also, I am grateful to the colleagues and students of the AG Kröll, former and present, who I have worked and spent time with. Special thanks go to Giovanna Umberti Caroli and Marco Brunken as well, who both helped to solve many organisatoric and other issues over the years.

During my stays at CERN and other facilities, a core group of people has been immensely helpful, be that for experimental setup or discussions on analysis and theory, including: Vinzenz Bildstein, Liam Paul Gaffney, Andres Illana Sison, Paweł Napiórkowski, Georgi Rainovski, Marcus Scheck, Nigel Warr, and Magda Zielińska.

For the experimental campaign of “my” xenon I must not forget to thank the IS548-MINIBALL collaboration and the ISOLDE team on-site for their great work and many hours spent to get the experiment going.

Quite important for this work were also fruitful email discussions with Atsuko Odahara on the experimental evidence stemming from β-decay spectroscopy compared to ours originating from Coulomb excitation of the same nucleus.

Additionally, I would like to express my gratitude to both Houda Naïdja and Tomás R. Rodríguez for performing the theoretical calculations, and especially answering my follow-up questions.

Last, but not least, I must thank my partner, close friends, and family, who have been there for me over the years and mainly the last months, and especially my parents who enabled me to study physics in the first place.

This work is supported by the German BMBF under contract 05P15RDCIA and 05P18RDCIA, has received funding from the European Union’s Horizon 2020 research and innovation programme under grant agreement no. 654002, and was supported by the ISOLDE Collaboration and technical teams, the MINIBALL Collaboration, and the IS548 Collaboration.

List of Figures

List of Tables

Bibliography

[1] M. Thoennessen. 2018 update of the discoveries of nuclides. *International Journal of Modern Physics E*, 28(01n02):1930002, 2019.

[2] J. Erler et al. The limits of the nuclear landscape. *Nature*, 486:509 – 512, 2012.

[3] C. Freiburghaus, S. Rosswog, and F.-K. Thielemann. r-process in neutron star mergers. *The Astrophysical Journal*, 525(2):L121–L124, nov 1999.

[4] E. Pian, P. D'Avanzo, S. Benetti, et al. Spectroscopic identification of r-process nucleosynthesis in a double neutron-star merger. *Nature*, 551:67–70, 2017.

[5] D. Rosiak et al. Enhanced Quadrupole and Octupole Strength in Doubly Magic $^{132}\mathrm{Sn}$. *Phys. Rev. Lett.*, 121:252501, Dec 2018.

[6] B. Bucher et al. Direct Evidence of Octupole Deformation in Neutron-Rich $^{144}\mathrm{Ba}$. *Phys. Rev. Lett.*, 116:112503, Mar 2016.

[7] P. A. Butler and W. Nazarewicz. Intrinsic reflection asymmetry in atomic nuclei. *Rev. Mod. Phys.*, 68:349–421, Apr 1996.

[8] P. A. Butler. Octupole collectivity in nuclei. *Journal of Physics G: Nuclear and Particle Physics*, 43(7):073002, jun 2016.

[9] W. Urban et al. The strength of octupole correlations in neutron-rich Xe isotopes. *The European Physical Journal A - Hadrons and Nuclei*, 16(3):303–307, Mar 2003.

[10] T. Behrens. *The Evolution of the B(E2) Values around the Doubly-Magic Nucleus ^{132}Sn*. PhD thesis, Technische Universität München, Lehrstuhl E12 für Experimentalphysik, 2009.

[11] M. J. G. Borge and Y. Kadi. ISOLDE at CERN. *Nuclear Physics News*, 26(4):6–13, 2016.

[12] E. Rutherford. *Phil. Mag.*, 21(669), 1911.

[13] J. Chadwick. Possible Existence of a Neutron. *Nature*, 129(312), 1932.

[14] D. Iwanenko. The Neutron Hypothesis. *Nature*, 129(798).

[15] W. Heisenberg. Über den Bau der Atomkerne. *Zeitschrift für Physik*, 77:1 – 11.

[16] M. Goeppert-Mayer. On Closed Shells in Nuclei. II. *Phys. Rev.*, 75:1969–1970, Jun 1949.

[17] O. Haxel, J. H. D. Jensen, and H. E. Suess. On the "Magic Numbers" in Nuclear Structure. *Phys. Rev.*, 75:1766–1766, Jun 1949.

[18] A. Bohr and B. R. Mottelson. Collective and individual-particle aspects of nuclear structure. *Mat. Phys. Medd. Dan. Vid. Selsk.*, 27(16), 1953. Edition 2 (1957).

[19] G. Audi, A. H. Wapstra, and C. Thibault. The Ame2003 atomic mass evaluation: (II). Tables, graphs and references. *Nuclear Physics A*, 729(1):337 – 676, 2003. The 2003 NUBASE and Atomic Mass Evaluations.

[20] D. J. Rowe and J. L. Wood. *Fundamentals of nuclear models, Foundational Models*. World Scientific Publishing Co. Pte. Ltd., 2010.

[21] N. Bohr. Neutron Capture and Nuclear Constitution. *Nature*, 137:344–348, 1936.

[22] N. Bohr and F. Kalckar. *Mat. Fys. Medd. Dan. Vid. Selsk.*, 14(10), 1937.

[23] Th. Mayer-Kuckuk. *Kernphysik, Eine Einführung*. B.G Teubner GmbH, Stuttgart / Leipzig / Wiesbaden, 2002.

[24] R. D. Woods and D. S. Saxon. Diffuse Surface Optical Model for Nucleon-Nuclei Scattering. *Phys. Rev.*, 95:577–578, Jul 1954.

[25] S. G. Nilsson. *Mat. Fys. Medd. Dan. Vid. Selsk.*, 29(16), 1955.

[26] K. Bethge, G. Walter, and B. Wiedemann. *Kernphysik*. Springer-Verlag Berlin Heidelberg, 2008.

[27] T. Glasmacher. Coulomb excitation at intermediate energies. *Annual Review of Nuclear and Particle Science*, 48(1):1–31, 1998.

[28] A. Winther and K. Alder. Relativistic coulomb excitation. *Nuclear Physics A*, 319(3):518 – 532, 1979.

[29] D. H. Rester, M. S. Moore, F. E. Durham, and C. M. Class. Internal conversion electrons from coulomb excitation of heavy elements. *Nuclear Physics*, 22(1):104 – 130, 1961.

[30] R. D. Sharp and W. W. Buechner. Coulomb excitation studies using inelastically scattered particles. *Phys. Rev.*, 109:1698–1703, Mar 1958.

[31] K. Alder, A. Bohr, T. Huus, B. Mottelson, and A. Winther. Study of nuclear structure by electromagnetic excitation with accelerated ions. *Rev. Mod. Phys.*, 28:432–542, Oct 1956.

[32] K. Alder, A. Bohr, T. Huus, B. Mottelson, and A. Winther. Errata: Study of nuclear structure by electromagnetic excitation with accelerated ions. *Rev. Mod. Phys.*, 30:353–353, Apr 1958.

[33] K. Alder. *Coulomb excitation: A collection of reprints*. Academic Publishing, New York, 1966.

[34] K. Alder and A. Winther. *Electromagnetic Excitation: Theory of Coulomb excitation with heavy ions*. North-Holland Publ., Amsterdam, 1975.

[35] J. de Boer and J. Eichler. *The Reorientation Effect*, pages 1–65. Springer US, Boston, MA, 1968.

[36] P. M. S. Lesser, D. Cline, P. Goode, and R. N. Horoshko. Static electric quadrupole moments of the first excited states of ^{56}Fe and the even titanium nuclei. *Nuclear Physics A*, 190(3):597 – 634, 1972.

[37] D. Cline. Nuclear Shapes Studied by Coulomb Excitation. *Annual Review of Nuclear and Particle Science*, 36(1):683–716, 1986.

[38] H. J. Wollersheim. *Kernstruktur schnell rotierender Atomkerne*. Habilitation treatise, Universität Frankfurt am Main, 1992.

[39] V. F. Weisskopf. Radiative Transition Probabilities in Nuclei. *Phys. Rev.*, 83:1073–1073, Sep 1951.

[40] P. M. Endt. Strengths of gamma-ray transitions in A = 91-150 nuclei. *Atomic Data and Nuclear Data Tables*, 26(1):47 – 91, 1981.

[41] D. Cline, T. Czosnyka, A. Hayes, P. Napiorkowski, N. Warr, and C. Wu. GOSIA user manual for simulation and analysis of Coulomb excitation experiments, 2012.

[42] C. A. Bertulani. *Nuclear Physics in a Nutshell*. Princeton University Press, New Jersey, 2007.

[43] T. Czosnyka, D. Cline and C. Y. Wu. *Bull. Am. Phys. Soc.*, 28, 735, 1983.

[44] M. Zielińska, L. P. Gaffney, K. Wrzosek-Lipska, et al. Analysis methods of safe Coulomb-excitation experiments with radioactive ion beams using the GOSIA code. *Eur. Phys. J. A*, 52, 2016.

[45] S. Sundell and H. Ravn. Ion source with combined cathode and transfer line heating. *Nuclear Instruments and Methods in Physics Research Section B: Beam Interactions with Materials and Atoms*, 70(1):160 – 164, 1992.

[46] U. C. Bergmann et al. Production yields of noble-gas isotopes from ISOLDE UCx/graphite targets. *Nuclear Instruments and Methods in Physics Research Section B: Beam Interactions with Materials and Atoms*, 204:220 – 224, 2003. 14th International Conference on Electromagnetic Isotope Separators and Techniques Related to their Applications.

[47] U. Köster V. Fedoseyev, G. Huber et al. The ISOLDE laser ion source for exotic nuclei. *Hyperfine Interactions*, 127:409–416, 2000.

[48] E. Kugler. The ISOLDE facility. *Hyperfine Interactions*, 129(1):23–42, Dec 2000.

[49] C. Geisse, H. Wollnik, B. Allardyce, E. Kugler, and K. Schloesser. The optics of ISOLDE 3 - The new on-line mass separator at CERN. *Nuclear Instruments and Methods in Physics Research Section B: Beam Interactions with Materials and Atoms*, 26(1):120 – 124, 1987.

[50] F. Ames et al. Cooling of radioactive ions with the Penning trap REXTRAP. *Nuclear Instruments and Methods in Physics Research Section A: Accelerators, Spectrometers, Detectors and Associated Equipment*, 538(1):17 – 32, 2005.

[51] F. Wenander. Charge breeding techniques. *Nuclear Physics A*, 746:40 – 46, 2004. Proceedings of the Sixth International Conference on Radioactive Nuclear Beams (RNB6).

[52] F. Wenander et al. The REX-ISOLDE charge breeder as an operational machine. *Review of Scientific Instruments*, 77(3):03B104, 2006.

[53] Y. Kadi et al. Post-accelerated beams at ISOLDE. *Journal of Physics G: Nuclear and Particle Physics*, 44(8):084003, 2017.

[54] R. Rao, O. Kester, T. Sieber, D. Habs, and K. Rudolph. Beam optics design of the REX-ISOLDE q/m-separator. *Nuclear Instruments and Methods in Physics Research Section A: Accelerators, Spectrometers, Detectors and Associated Equipment*, 427(1):170 – 176, 1999.

[55] M. J. G. Borge and K. Riisager. HIE-ISOLDE, the project and the physics opportunities. *The European Physical Journal A*, 52(11):334, Nov 2016.

[56] C. Benvenuti et al. Superconducting niobium sputter-coated copper cavity modules for the LEP energy upgrade. Technical report, 1991. Conf. Rec. 1991 IEEE Part. Accel. Conf. (San Francisco).

[57] V. Palmieri et al. New Results on Niobium sputtered Copper quarter wave resonators. In *Proc. of the Sixth Workshop on RF Superconductivity, Newport News, Virginia*, 1993.

[58] J. A. Rodriguez. Beam Commissioning and Operations of the REX/HIE-ISOLDE Post-accelerator. URL: `https://indico.cern.ch/event/561089/contributions/2359008/`, 2016.

[59] H. Ower et al. CLX/DCY. Computer program.

[60] J. Eberth et al. Miniball: A Gamma-Ray Spectrometer With Position-Sensitive Ge Detectors For Nuclear Structure Studies At REX-ISOLDE. *AIP Conference Proceedings*, 656(1):349–356, 2003.

[61] N. Warr et al. The Miniball spectrometer. *The European Physical Journal A*, 49(3), 2013.

[62] V. Bildstein et al. T-REX. *The European Physical Journal A*, 48(6):85, Jun 2012.

[63] S. Hellgartner. *Probing Nuclear Shell Structure beyond the N = 40 Subshell using Multiple Coulomb Excitation and Transfer Experiments*. PhD thesis, Technische Universität München, Germany, 2015.

[64] Mesytec. MPR-16 / LMPR-32 / MPR-64 Data Sheet V8.0 05. `https://www.mesytec.com/products/datasheets/MPR-16.pdf`. Accessed: 03.09.20.

[65] Mesytec. STM-16+ Data Sheet V2.4 02. `https://www.mesytec.com/products/datasheets/STM-16+.pdf`. Accessed: 03.09.20.

[66] Mesytec. MADC-32 Data Sheet V2.1 04. `https://www.mesytec.com/products/datasheets/MADC-32.pdf`. Accessed: 03.09.20.

[67] Mesytec. MSI-8 Data Sheet V2.0 02. `https://www.mesytec.com/products/datasheets/MSI-8.pdf`. Accessed: 03.09.20.

[68] Micron Semiconductor Ldt. QQQ2. `http://www.micronsemiconductor.co.uk/product/qqq2/`. Accessed: 27.06.20.

[69] Mesytec. MUX-16 /-32 /-64 Data Sheet V2.4 01. `https://www.mesytec.com/products/datasheets/MUX-16.pdf`. Accessed: 27.06.20.

[70] R. Lutter, O. Schaile, K. Schöffel, K. Steinberger, and C. Broude. Marabou, MBS And ROOT Based Online/Offline Utility. `https://www-old.mll-muenchen.de/marabou/htmldoc/`.

[71] H. G. Essel and N. Kurz. The general purpose data acquisition system MBS. *IEEE Transactions on Nuclear Science*, 47(2):337–339, April 2000.

[72] R. Brun and F. Rademakers. ROOT - An Object Oriented Data Analysis Framework. Proceedings AIHENP'96 Workshop, Lausanne, Sep. 1996, Nucl. Inst. & Meth. in Phys. Res. A 389 (1997) 81-86. See also `http://root.cern.ch/`.

[73] V. Bildstein. *Exploring the Island of Inversion with the d(^{30}Mg,p)^{31}Mg Reaction*. PhD thesis, Technische Universität München, Lehrstuhl E12 für Experimentalphysik, 2010.

[74] K. Wimmer. *Discovery of the shape coexisting 0^+ state in ^{32}Mg*. PhD thesis, Technische Universität München, Lehrstuhl E12 für Experimentalphysik, 2010.

[75] A. K. Nowak. *Untersuchungen zur Formkoexistenz durch die ^{44}Ar(t,p)^{46}Ar-Reaktion in inverser Kinematik*. PhD thesis, Technische Universität München, Lehrstuhl E12 für Experimentalphysik, 2015.

[76] M. J. Martin. Nuclear Data Sheets for A = 152. *Nuclear Data Sheets*, 114(11):1497 – 1847, 2013.

[77] D. Rosiak. *Coulomb excitation of doubly-magic ^{132}Sn at HIE-ISOLDE and development of escape-suppression shields for the MINIBALL spectrometer*. PhD thesis, Universität zu Köln, Germany, 2018.

[78] G. Pasquali et al. Pulse height defect of energetic heavy ions in ion-implanted Si detectors. *Nuclear Instruments and Methods in Physics Research Section A: Accelerators, Spectrometers, Detectors and Associated Equipment*, 405(1):39 – 44, 1998.

[79] J. Yorkston, A. C. Shotter, D. B. Syme, and G. Huxtable. Interstrip surface effects in oxide passivated ion-implanted silicon strip detectors. *Nuclear Instruments and Methods in Physics Research Section A: Accelerators, Spectrometers, Detectors and Associated Equipment*, 262(2):353 – 358, 1987.

[80] L. Grassi et al. Study of the inter-strip gap effects on the response of Double Sided Silicon Strip Detectors using proton micro-beams. *Nuclear Instruments and Methods in Physics Research Section A: Accelerators, Spectrometers, Detectors and Associated Equipment*, 767:99 – 111, 2014.

[81] D. Torresi et al. Influence of the interstrip gap on the response and the efficiency of Double Sided Silicon Strip Detectors. *Nuclear Instruments and Methods in Physics Research Section A: Accelerators, Spectrometers, Detectors and Associated Equipment*, 713:11 – 18, 2013.

[82] B. Bruyneel, P. Reiter, and G. Pascovici. Characterization of large volume HPGe detectors. Part II: Experimental results. *Nuclear Instruments and Methods in Physics Research Section A: Accelerators, Spectrometers, Detectors and Associated Equipment*, 569(3):774 – 789, 2006.

[83] Z. Sosin. Description of the plasma delay effect in silicon detectors. *Nuclear Instruments and Methods in Physics Research Section A: Accelerators, Spectrometers, Detectors and Associated Equipment*, 693:170 – 178, 2012.

[84] J. F. Ziegler. The electronic and nuclear stopping of energetic ions. *Applied Physics Letters*, 31(8):544–546, 1977.

[85] J. F. Ziegler, M. D. Ziegler, and J. P. Biersack. SRIM - the stopping and range of ions in matter (2010). *Nuclear Instruments and Methods in Physics Research Section B: Beam Interactions with Materials and Atoms*, 268(11):1818 – 1823, 2010. 19th International Conference on Ion Beam Analysis.

[86] T. D. Johnson, D. Symochko, M. Fadil, and J. K. Tuli. Nuclear Data Sheets for A = 142. *Nuclear Data Sheets*, 112(8):1949 – 2127, 2011.

[87] S. Ilieva et al. Measurement of picosecond lifetimes in neutron-rich Xe isotopes. *Phys. Rev. C*, 94:034302, Sep 2016.

[88] A. Notea. The Ge(Li) spectrometer as a point detector. *Nuclear Instruments and Methods*, 91(3):513 – 515, 1971.

[89] K. Kohn. *Gamma Ray Spectroscopy of Fission Fragments*. Bachelor thesis. Unpublished, TU Darmstadt, 2016.

[90] M. Bentaleb, N. Schulz, E. Lubkiewicz, et al. Search for octupole deformation in neutron-rich Xe isotopes. *Z. Phys. A - Hadrons and Nuclei*, 354:143–151, 1996.

[91] A. Yagi et al. Study of neutron-rich ^{142}Xe using β-decay spectroscopy, 2016. Accel. Prog. Rep. 49.

[92] A. Odahara. Private communication.

[93] F. G. Kondev. Nuclear Data Sheets for A = 206. *Nuclear Data Sheets*, 109(6):1527 – 1654, 2008.

[94] H. Bateman. Solution of a system of differential equations occurring in the theory of radioactive transformations. *Proc. Cambridge Phil. Soc.*, 15:423 – 427, 1910.

[95] J. F. Wright. *Five-Particle, Shell-Model Calculation Using a Spin Dependent Potential as Applied to ^{101}Tc and the Nuclear Decays of ^{101}Mo, ^{101}Tc, ^{142}Xe, and ^{142}Cs*. PhD thesis, Iowa State University, United States of America, 1974.

[96] A. S. Mowbray et al. New nucleus $^{142}\mathrm{Xe}$: Test of the $n_p n_n$ scheme. *Phys. Rev. C*, 42:1126–1129, Sep 1990.

[97] W. Urban et al. First evidence of γ collectivity close to the doubly magic core $^{132}\mathrm{Sn}$. *Phys. Rev. C*, 93:034326, Mar 2016.

[98] H. Naïdja et al. New excitations in $^{142}\mathrm{Ba}$ and $^{144}\mathrm{Ce}$: Evolution of γ bands in the $n = 86$ isotones. *Phys. Rev. C*, 95:064303, Jun 2017.

[99] NT Brewer et al. Octupole Deformation in 144Ba and 148Ce. In *Fission And Properties Of Neutron-rich Nuclei-Proceedings Of The Sixth International Conference On Icfn6*, page 197. World Scientific, 2017.

[100] O. Helene. Upper limit of peak area. *Nuclear Instruments and Methods in Physics Research*, 212(1):319 – 322, 1983.

[101] S. M. Scott et al. The neutron-rich barium isotopes. *Journal of Physics G: Nuclear Physics*, 6(10):1291–1317, oct 1980.

[102] T. Kibédi, T. W. Burrows, M. B. Trzhaskovskaya, P. M. Davidson, and C. W. Nestor. Evaluation of theoretical conversion coefficients using BrIcc. *Nuclear Instruments and Methods in Physics Research Section A: Accelerators, Spectrometers, Detectors and Associated Equipment*, 589(2):202 – 229, 2008.

[103] R. K. J. Sandor et al. Interplay between single-particle and collective degrees of freedom in the excitation of the low-lying states in ^{142}Nd. *Nuclear Physics A*, 535(3):669 – 700, 1991.

[104] R. K. J. Sandor et al. Shape transition of ^{146}Nd deduced from an inelastic electron-scattering experiment. *Nuclear Physics A*, 551(3):378 – 408, 1993.

[105] B. S. Nara Singh, V. Nanal, and R. G. Pillay. Hexadecapole deformation studies in ^{148,150}Nd. *PRAMANA - journal of physics*, 61(3):507–515, 2003.

[106] W. Kim et al. Interplay between single-particle and collective degrees of freedom in the excitation of the low-lying states in $^{140}\mathrm{Ce}$. *Phys. Rev. C*, 45:2290–2299, May 1992.

[107] S. M. Burnett, A. M. Baxter, S. Hinds, F. Pribac, R. H. Spear, and W. J. Vermeer. A measurement of B(E3;$0^+ \to 3_1^-$) and some E2 transition probabilities in $^{132,\,134,\,136,\,138}$Ba using Coulomb excitation. *Nuclear Physics A*, 432(2):514 – 524, 1985.

[108] C. Henrich. *Coulomb excitation of neutron-rich xenon isotopes*. Master thesis. Unpublished, TU Darmstadt, 2014.

[109] T. R. Rodríguez. Private communication.

[110] H. Naïdja. Private communication.

[111] H. Naïdja, F. Nowacki, and B. Bounthong. Shell-model investigation of spectroscopic properties and collectivity in the nuclei beyond $^{132}\mathbf{Sn}$. *Phys. Rev. C*, 96:034312, Sep 2017.

[112] H. Naïdja and F. Nowacki. Spectroscopic properties and collectivity beyond $^{\mathrm{Sn}}$. *Acta Physica Polonica B*, 48, 2017.

[113] E. Caurier and F. Nowacki. Present Status of Shell Model Techniques. *Acta Physica Polonica B*, 30, 1999.

[114] E. Caurier, G. Martínez-Pinedo, F. Nowacki, A. Poves, and A. P. Zuker. The shell model as a unified view of nuclear structure. *Rev. Mod. Phys.*, 77:427–488, Jun 2005.

[115] D. R. Entem and R. Machleidt. Accurate charge-dependent nucleon-nucleon potential at fourth order of chiral perturbation theory. *Phys. Rev. C*, 68:041001, Oct 2003.

[116] M. Hjorth-Jensen, T. T. S. Kuo, and E. Osnes. Realistic effective interactions for nuclear systems. *Physics Reports*, 261(3):125 – 270, 1995.

[117] J. F. Berger, M. Girod, and D. Gogny. Microscopic analysis of collective dynamics in low energy fission. *Nuclear Physics A*, 428:23 – 36, 1984.

[118] T. R. Rodríguez. Precise description of nuclear spectra with Gogny energy density functional methods. *The European Physical Journal A*, 52(190), 2016.

[119] S. Raman, C. W. Nestor, S. Kahane, and K. H. Bhatt. Low-lying collective quadrupole and octupole strengths in even-even nuclei. *Phys. Rev. C*, 43:556–581, Feb 1991.

[120] Ulrich Kneissl, Norbert Pietralla, and Andreas Zilges. Low-lying dipole modes in vibrational nuclei studied by photon scattering. *Journal of Physics G: Nuclear and Particle Physics*, 32(8):R217–R252, jun 2006.

[121] G. Alaga and K. Alder and A. Bohr and B. R. Mottelson. Intensity rules for beta and gamma transitions to nuclear rotational states. *Dan. Mat. Fys. Medd.*, 29(9), 1955.

[122] A. Lindroth, B. Fogelberg, H. Mach, M. Sanchez-Vega, and J. Bielčík. Octupole Vibration and Influence of Shell Effects on the $E1$ Transition Rates in $^{140}\mathrm{Xe}$. *Phys. Rev. Lett.*, 82:4783–4786, Jun 1999.

[123] M. von Tresckow and M. Rudigier. Private communication.

[124] F. A. White, T. L. Collins, and F. M. Rourke. Search for Possible Naturally Occurring Isotopes of Low Abundance. *Phys. Rev.*, 101:1786–1791, Mar 1956.